Clays and Clay Minerals, Vol. 62, No. 6, 447–469, 2014.

AN INTEGRATED METHODOLOGICAL APPROACH FOR SOURCE-CLAY DETERMINATION OF ANCIENT CERAMICS: THE CASE OF AEGINA ISLAND, GREECE

GEORGE E. CHRISTIDIS[1,*], CHRISTINE M. SHRINER[2], AND HAYDN H. MURRAY[2,†]

[1] Technical University of Crete, Department of Mineral Resources Engineering, 73100 Chania, Greece
[2] Department of Geological Sciences, Indiana University, Bloomington, IN 47405, USA

Abstract—A new model is proposed for analysis of the source clays used to create ceramics, based on geographic, petrographic, mineralogical, mineral-chemistry, and geochemical criteria. The development of this model became feasible after the discovery of a Pliocene volcanic clay horizon on NW Aegina Island, Greece. The volcanic clay contains smectite, mixed-layer chlorite-smectite, biotite, and palygorskite and has greater feldspar content than the underlying Pliocene marls, which contain R0 mixed-layer illite-smectite, mica, dolomite, serpentine, talc and gypsum, and, in some places, palygorskite. The two units have distinct geochemical characteristics. In general the Pliocene volcanic clay is richer in SiO_2, Al_2O_3, and Fe_2O_3 and poorer in Na_2O, MgO, and P_2O_5 than the Pliocene marls. The Nb, Zr, Hf, Th, and rare earth element (*REE*) contents are also significantly greater in the Pliocene volcanic clay and comparable to those of the dacitic rocks of the island, reflecting the volcanic origin of the clay.

The proposed model was used to identify the source-clay materials that were used for the production of ceramics on the island of Aegina (Aeginetan Ware). All five criteria should be considered in any provenance study. The use of individual criteria on their own can lead to ambiguous conclusions. In the present study the geochemical criterion was particularly helpful. It provided robust evidence for the nature of the source clay. The Pliocene volcanic clay horizon and the underlying Pliocene marls are the candidate raw materials for Aeginetan Ware. Although the Pliocene marls have been invoked as raw materials for Greek Bronze Age (~3000−1100 BC) Aeginetan ceramics and are used as raw materials by modern Aeginetan ceramists, the geochemical characteristics of a large set of Bronze Age Greek Aeginetan sherds with fine and coarse fabrics coincide with those of the Pliocene volcanic clay. This comparative and cumulative evidence suggests that the Pliocene volcanic clay was the main source clay for ancient Aeginetan ceramics, regardless of the fabric (coarse or fine) and that admixture of different sources might not be necessary for fine-grained ceramics.

Key Words—Aegina Island, Archaeological Ceramics, Clay-material Multi-criteria Approach, Geochemistry, Greece, Mineralogy, Pliocene Volcanic Clay, Provenance Studies.

INTRODUCTION: RESEARCH APPROACH

Clay-rich materials have been used since ancient times in the fabrication of various types of ceramic articles (*e.g.* Freestone and Gaimster, 1997; Velde and Druc, 1999). The oldest pottery articles dated so far (12−14 ka) have been found in Japan and belong to the Jomon period (Kaner, 2003). Recognition of the source clays used as raw materials in ceramics involves a complex array of provenance studies. Examination of potential source clays has been included in provenance research designs of various cross-disciplinary ceramic studies (Jones, 1986, 1993; Douglass and Schaller, 1993; Shriner, 1999; Shriner and Dorais, 1999; Day and Kiriatzi, 1999; Whitbread, 2001; Whitbread *et al.*, 2002; Dorais and Shriner, 2002a, 2002b; Dorais *et al.*, 2004; Rathossi *et al.*, 2004; Ruby and Shriner, 2005; Prudencio *et al.*, 2006; Dias and Prudencio, 2008; Marques *et al.*, 2010; Trindade *et al.*, 2010; Gauß and Kiriatzi, 2011; Braekmans *et al.*, 2011; Ma *et al.*, 2012). A major impediment to success in attempts to link specific ceramic samples with specific source clays has been the lack of an effective method of comparison and correlation between source-clay data and existing descriptions and characterizations of ceramic artifacts.

The recognition of clay horizons used for fabrication of clay ceramics in prehistoric and historic time periods can be paralleled with provenance studies of sedimentary rocks and industrial sedimentary clay deposits. Provenance studies that include mineralogical and/or geochemical fingerprinting are common in applied clay geology and sedimentary geology. These studies are useful in identifying the sources of constituent minerals, in understanding transport and deposition mechanisms, and in recognizing diagenetic or other alterations of argillaceous sediments (Cullers *et al.*, 1979; Wronkiewitz and Condie, 1990; Dombrowski, 1993; Slack and Stevens, 1994; Faupl *et al.*, 1998; Setti *et al.*, 2004; Gonzalez-Lopez *et al.*, 2005). The methods involved in provenance studies include analysis of textural features of characteristic minerals present in

* E-mail address of corresponding author:
christid@mred.tuc.gr
† Deceased
DOI: 10.1346/CCMN.2014.0620601

the rock (both clay minerals and heavy minerals), interpretation of the chemical trends in the sediments using trace elements, and radiometric dating (Marinoni *et al.*, 2008).

In the present contribution, an integrated approach for ceramic provenance analysis is proposed to identify clay-rich sediments used as raw materials for the fabrication of ceramics. The approach proposed is method-driven, relying on a set of verifications (Kingery, 1982). The weight-of-evidence approach recognizes that in attempting to identify the origin of source clays for ceramics there is generally no single fingerprint that is indisputable. Rather, the strength of the argument rests upon the successful combination of a variety of factors. Therefore, an attempt is made to introduce a set of geologic, mineralogical, and geochemical techniques as key tools for answering important questions. This approach, which combines field observations, petrographic analysis, mineralogy, mineral chemistry, and bulk-element analysis, focuses on the potential raw materials rather than the ceramic articles. The aim of this research is to show that the use of this interdisciplinary approach contributes to reliable ceramic source-clay provenance analysis and eventually, through experimental ceramic source-clay research, to a deeper understanding of ceramic technology changes.

As a reference study area, the island of Aegina, Greece was selected. Aegina was a major producer of ceramics for various purposes in Greece, from the Early Bronze Age (ca. 3000 to 2000 BC) through at least the Classical period, ca. 400 BC, (Gauß and Kiriatzi, 2011). Presumed Aeginetan ceramics of various ages have been found in many areas of the Aegean and the Greek mainland (*e.g.* Zerner, 1986, 1993; Nordquist, 1987; Rutter, 1989, 1990; Dietz, 1991; Forsén, 1996; Pullen, 2000, 2011; Lindblom, 2001; Rotroff, 2006). These ceramics suggest that exchange of ceramics between different locations was in progress from a very early time. Reliable provenancing of a source clay for ancient Aeginetan ceramics has been a specific problem. Two clay horizons on the island, the Pliocene volcanic clay unit and the underlying Pliocene marl, used by modern potters, are possible sources of the ceramics. A clayey horizon known as 'Plakakia clays' exposed along and near the NW coast of the island (Figure 1) was proposed by Hein *et* al. (2004) as a source of at least some Bronze Age Aeginetan ceramics. In their compilation, based on petrographic and chemical data, Gauß and Kiriatzi (2011) proposed that the two Aeginetan ceramic Fabric Groups (FG1 and FG2) had been produced from different sources: the coarser FG1 was derived from a volcanic sediment of Holocene age, whereas the finer FG2 was derived from a mixture of the Pliocene marls with material from a volcanic source, probably the same as that used for FG1, at a 80:20 ratio. Those authors considered the Plakakia clays to be Pliocene marls. No volcanic clayey horizon of substantial thickness which would sustain the production of Aeginetan ceramics for ~2000 years was reported by Gauß and Kiriatzi (2011) on the island. The present study aimed to show that a substantial volcanic clay horizon is indeed present on the island and that use of the integrated approach employed here contributes to reliable archeological provenance analysis, which may resolve issues of possible mixing of raw materials for production of ancient ceramics.

GEOLOGIC FRAMEWORK

The volcanic island of Aegina is situated in the northwestern part of the Southern Aegean Volcanic Arc (SAVA) (Figure 1a), activity of which began during the Pliocene (Figure 1b). The island is composed of three units: (1) Alpine sediments; (2) Neogene pre-volcanic sediments; and (3) volcanic sequences (Dietrich *et al.*, 1991). The Alpine rocks span from Permian to Maastrichtian and include limestones (partly recrystallized in some horizons), cherts, and flysch. The Neogene (lower Pliocene) pre-volcanic sediments (namely Pliocene marls) consist of transgressive conglomerates at their base, followed by shallow marine limestones and marls (which are dolomitized in places); lacustrine sands and silts; breccias; and silty clays with intercalations of diatomites and fluviolacustrine silts and sands (Benda *et al.*, 1979; Stamatakis and Magganas, 1989).

The volcanic sequence includes some of the oldest rocks of the SAVA (Pe-Piper *et al.*, 1983) and comprises rocks that erupted in two episodes (Dietrich *et al.*, 1988; 1991). The first episode (4.4−3 Ma), known as the dacitic phase, began during the Early Pliocene, producing rhyodacitic tuffs and pumice, followed by andesitic dacite flows and plugs (Figure 2). The episode terminated with the eruption of dacitic pyroclastic and volcaniclastic flows. The first tuff (4.4 ± 0.2 Ma according to Müller *et al.*, 1979), associated with the Skotini volcano eruption (Figure 2), and the subsequent volcaniclastic flows, form the volcanic base of Aegina Island and were exposed throughout the rest of the Pliocene (Dietrich *et al.*, 1991). The second episode, known as the andesitic phase, was initiated during the Late Pliocene after a long period of quiescence. These rocks were erupted from two volcanic centers and produced minor amounts of pyroclastics and lavas of basaltic andesite composition. The basaltic andesite at Oros was dated to the Late Pliocene (2.1 ± 0.1 Ma) and the rhyodacite at Kakoperato, to a slightly earlier Late Pliocene age (2.2−2.45 Ma) (Morris, 2000) (Figure 2). Dietrich *et al.* (1991) designated as Pleistocene both fluviolacustrine and limnic deposits of clay, silt, and sand, often with intercalations of volcaniclastic volcanic material, followed by coastal calcareous sandstones and marly limestones, known as Poros.

Between the Pliocene marls and the Poros marly limestone, there is a 0.4−4 m thick, laterally extensive reddish brown clay-rich horizon, which is exposed along

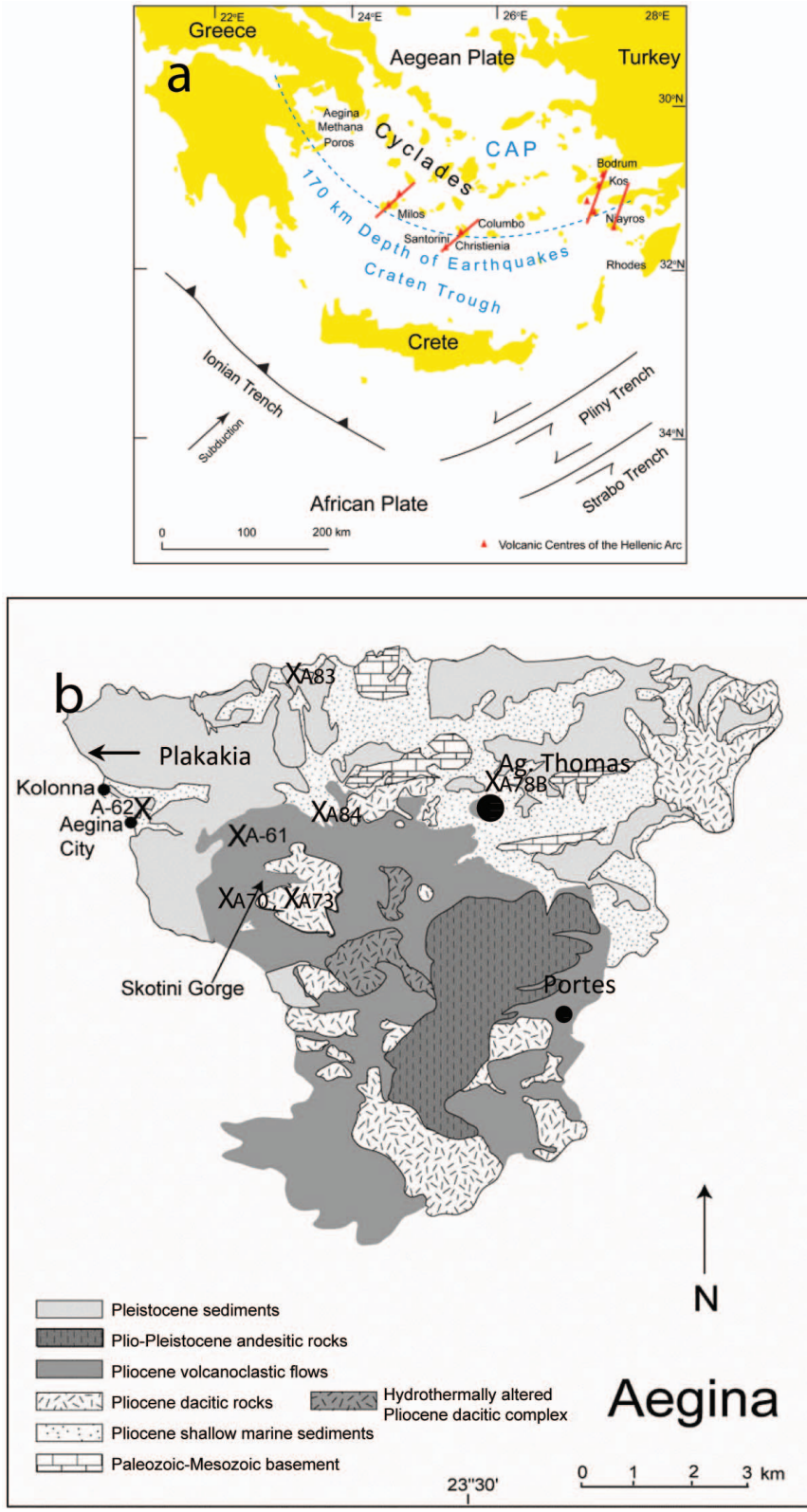

Figure 1. (a) The geographic location of the volcanic centers in the South Aegean Volcanic Arc (SAVA). (b) A simplified geologic map of Aegina Island. A61 and A62 are representative samples of the Aegina Pliocene volcanic clay. Samples A66, A58L and A58U were obtained 50 m upstream from A61.

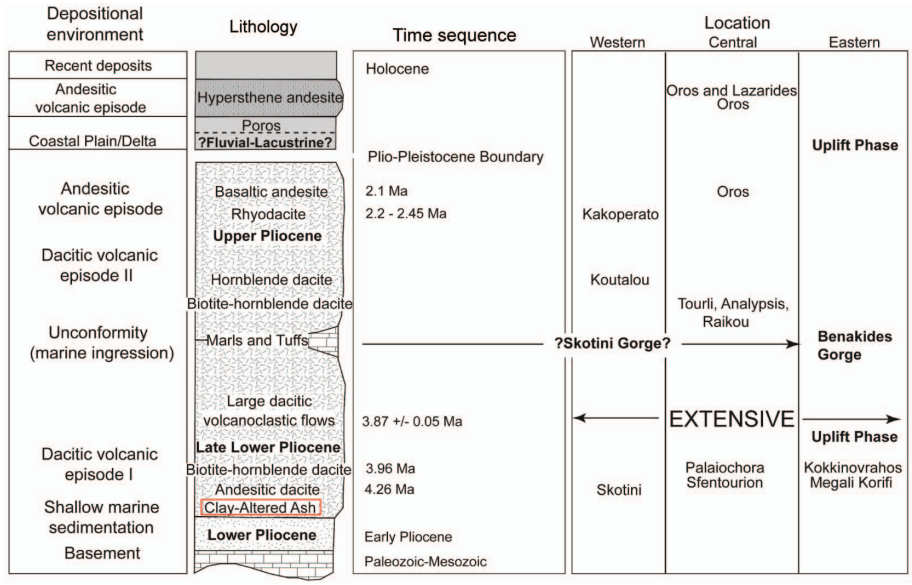

Figure 2. Composite framework visual for the time sequences of geologic activity on Aegina Island and the resultant depositional environment (modified after data from Dietrich *et al.*, 1991 and Morris, 2000). The time position of the clay-altered volcanic ash sediment is noted as Lower Pliocene.

nearly the entire northwestern coast of Aegina and along road cuts and ravine flanks, but does not crop out at the surface (Figure 3). The clay has not been recognized as a distinct unit in previous studies (*e.g.* Tsolis-Katagas, 1977; Dietrich *et al.*, 1991; Gauß and Kiriatzi, 2011) and was considered to be Pleistocene in age (Dietrich *et al.*, 1991). The clay-rich horizon consists of a fairly uniform mixture of clay and calcite nodules and contains abundant amphibole crystals embedded in the clay matrix. Internal stratification is largely absent, though some exposures display vertical changes in color. In many exposures, isolated pebbles or cobbles of older dacite are found suspended within the interior of the clay horizon. These characteristics clearly attest to an altered equivalent of a submarine airfall tuff deposit (Shriner *et al.*, 2007; Christidis *et al.*, in press). Shallow-marine microfossils are present. The microfossils present in the clay-altered ash unit suggest an Early Pliocene age for the original ash and suggest deposition on the adjacent submarine platform at depths ranging from shallow to deep (Figure 2). The depositional environment and the evolution of this bed will be the subject of future contribution to the literature.

MATERIALS AND METHODS

Samples were collected from the Pliocene volcanic clay underlying Poros calcareous sediments, from the Pliocene marls of the northwestern part of Aegina Island and the area of Agios Thomas, and from fresh outcrops of the dacitic volcaniclastic flows (Figure 1b). Sample N2 is a Pliocene marl from Ag. Thomas supplied by a local ceramist. Because the Pliocene volcanic clay was not exposed on the surface, samples were obtained from ravine flanks, road cuts, and coastal cliffs. All samples were collected at a depth of 10−15 cm from the outcrop surface to minimize the effects of weathering and contamination. The volcanic clay samples contained abundant calcite nodules larger than 2 mm and small dacitic pebbles ~10 mm in size. These nodules and pebbles were removed by sieving; the material passing through the 2 mm sieve was used for further examination. The Pliocene marls selected were free of calcite nodules. The bulk mineralogy of the Pliocene volcanic clay and marl samples was determined by X-ray diffraction (XRD) (Siemens D500, CuKα radiation, graphite monochromator, 35 kV and 35 mA, 0.02º step size, and counting time of 1 s/step) on randomly oriented samples, initially crushed with a fly press and subsequently ground with pestle and mortar. The clay mineralogy was determined in materials dispersed in distilled water using an ultrasonic probe (20 s). The <2 μm fractions were separated by settling, dried on glass slides at room temperature, and then solvated with ethylene-glycol (EG) vapor at 60ºC overnight to ensure maximum saturation. The XRD traces of the clay fractions were obtained using a 0.02º step size and a counting time of 4 s/step. Mineral abundances were calculated from XRD data using *Autoquan*© software, which uses Rietveld refinement.

Major-element analysis of representative samples of Pliocene volcanic clays, Pliocene marls, and dacitic volcaniclastic flows cropping out on the island, was carried out by inductively coupled plasma-optical emission spectrometry (ICP-OES). Trace-element analysis of these samples was performed by ICP-mass spectrometry (ICP-MS). Both analyses were conducted

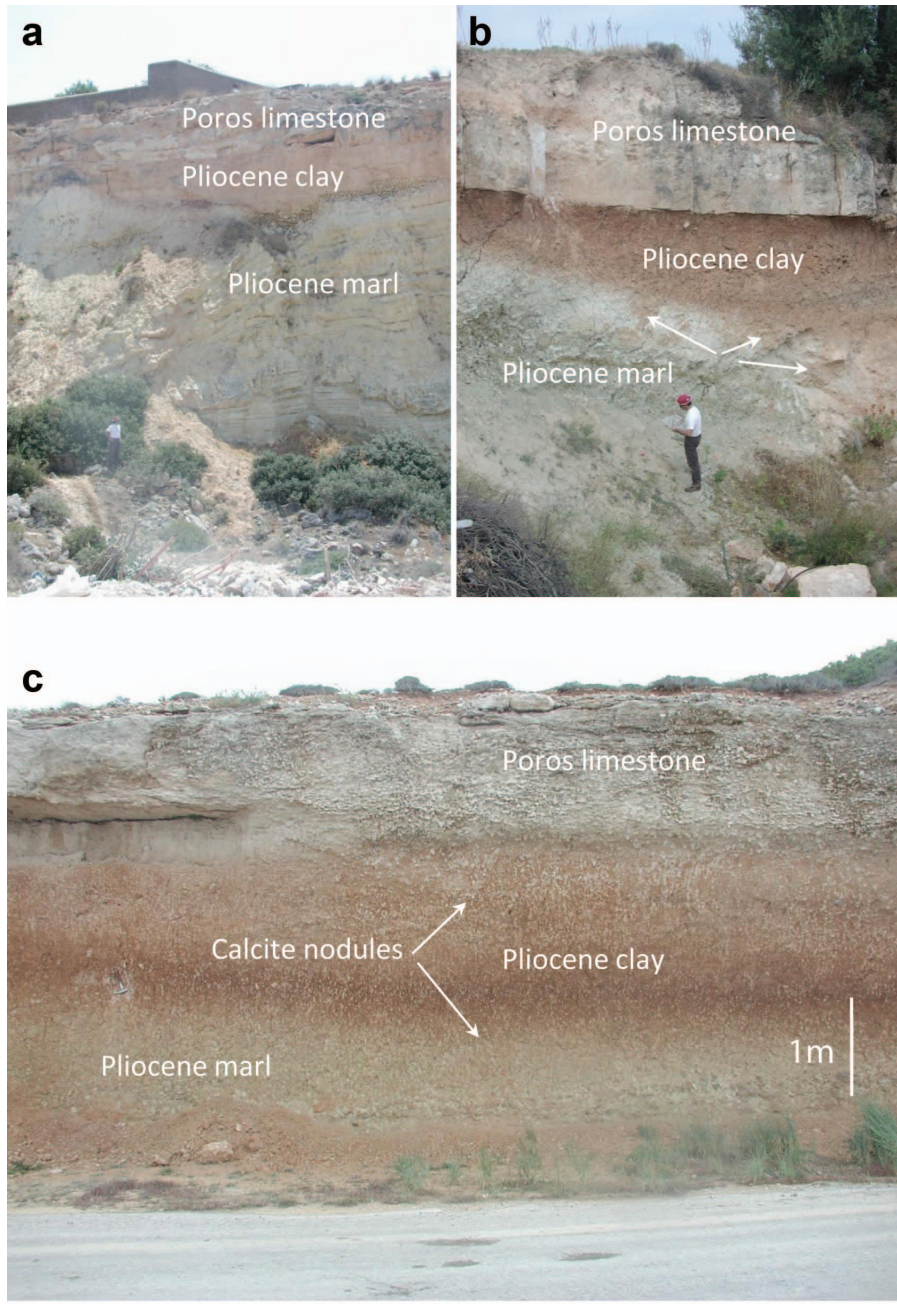

Figure 3. Typical exposures of the Pliocene volcanic clay between the Pliocene marl at the bottom and the Poros limestone. In outcrops free of debris from the overlying Pliocene clay, the boundary between the Pliocene volcanic clay and the Pliocene marl is sharp (3a). The arrows in 3b indicate debris from the overlying Pliocene volcanic clay. In 3c the boundary is obscured by the calcite nodules. See text for discussion.

at ACME Analytical Laboratories, Canada. Analysis involved fusion of 0.2 g samples with a lithium metaborate-lithium tetraborate mixture, followed by digestion in dilute nitric acid. Loss on ignition (LOI) was determined by mass difference after ignition at 1000ºC. Data for trace elements, including rare earth elements (*REE*), in a large set of different types of ceramics from the archeological site of Kolonna were obtained from Mommsen *et al.* (2001). The ceramics data used in the present study belong to the Mommsen *et al.* (2001) chemical groups A, E, F, and P, known to originate from Aegina. Furthermore, a sub-set of the Mommsen *et al.* (2001) original neutron activation analysis (NAA) sample set was supplied to the present authors by F. Felten, director of archeological excavations at Kolonna, University of Salzburg, Austria. This

sub-set was delivered as 83 highly polished thin sections. These thin sections were analyzed by electron microprobe analysis (EMPA). The ceramics data were compared with a databank of SAVA dacitic rock samples, including those from Aegina (Brophy *et al.*, in press; cf. http://www.indiana.edu/~sava/), in order to verify a local Aegina provenance for the chemical groups A, E, F, and P of Mommsen *et al.* (2001).

A second sample set of >80 sherds from Kolonna was supplied by Drs F. Felten and L. Berger (University of Salzburg, Austria) (see table under supplementary materials at the SAVA website, http://www.indiana.edu/~sava/), was assembled for further comparative study (Brophy *et al.*, in press; Christidis *et al.*, in press; Shriner *et al.*, in press), and was used in the present study for LOI determination. This second Kolonna sample set was comparable to the sub-set from Mommsen *et al.* (2001) in that the ceramics were predominantly of local provenance (L. Berger, pers. comm.). The sherds have been examined with optical microscopy, and analyzed by XRD and with comparative EMPA (Brophy *et al.*, in press). For 28 of the Aeginetan sherds, the LOI was determined by firing at 980ºC for 2 h and was found to vary between 2.95 and 17.89% (average 7.97%), and is due mainly to the presence of calcite. In the present study, the Mommsen *et al*. (2001) chemical NAA data have been adjusted for LOI in order to be comparable with the LOI-adjusted potential source (Pliocene volcanic clay and the Pliocene marl) data. The LOI correction for the sherds is 7.97%. Note that statistical analysis was carried out on the dataset of Mommsen *et al.* (2001) by Hein *et al*. (2004).

In order to reduce the dilution effect of calcite, which is abundant in both sediment types, the geochemical comparisons for both the major and the trace elements, including the *REE*, were carried out on a volatile-free basis. This was achieved by recalculation of the elemental concentrations on a LOI-free basis for each sample. In this manner the geochemical compositions of the sediments were directly comparable to those of the sherds, after LOI correction of the latter (see above). In geochemical plots involving elemental ratios, normalization by LOI was not necessary.

Gold-coated broken surfaces of representative Pliocene volcanic clay samples were examined using a JEOL JSM-5400 scanning electron microscope (SEM) equipped with an Oxford Link energy dispersive spectrometer (EDS) for qualitative analyses, in order to determine the textural relationships between the various mineral phases of the clays and marls. In selected samples the clay fraction was separated, spread on glass slides, coated with carbon and examined by SEM to detect the presence of palygorskite. Particle-size distribution of the sand and coarse silt fraction of the Pliocene volcanic clay and Pliocene marls was obtained by wet sieving after removal of calcite nodules by hand picking (Christidis *et al.*, in press).

RESULTS

Geologic characteristics of the Pliocene volcanic clay and the volcanic marls

The Pliocene volcanic clay horizon is a horizontal bed that underlies the Poros marly limestones (Figure 3a,b). Where it is exposed, its thickness varies from 40 cm to almost 4 m depending on the paleosurface of the underlying rocks, which consist of Pliocene marls (Figure 3). In general, the thickness and the D_{50} particle size obtained from the particle-size distribution curves (data not shown) increase towards the volcanic centre of Skotini, from which the original volcanic ash is considered to have been derived (Figure 1b). The contact with the underlying Pliocene marls is, in general, discordant and sharp without gradual transitions, reflecting the hiatus between the two horizons (Figure 3a). This suggests a depositional setting controlled by water depth, as is expected in coastal environments. In places, debris from the overlying Pliocene volcanic clay may make the contact between the two horizons obscure (Figure 3b). The contact with the overlying Poros marly limestones is also sharp (Figure 3).

The Pliocene volcanic clay bed is light red to brownish-red in color, becoming darker brown in places, and contains abundant calcite nodules, which are either scattered in the clay bed or are aligned vertically (Figure 3c). These nodules, which are more abundant in the Pliocene volcanic clay compared to the Pliocene marls, may also obscure the boundary between the two horizons. Such nodular textures are typical of calcretes; they are associated with downward movement of groundwater in arid environments (Collinson and Thompson, 1988) and indicate post-depositional soil-formation processes. Nodule formation is more intense away from the volcanic edifice of the island and is evident along the northern coastline. The amphiboles present in the clay bed are identical in composition to those present in the Aeginetan volcanic rocks thus reflecting the volcanic component of the clay horizon (Brophy *et al.*, in press; website, http://www.indiana.edu/~sava/). Gauß and Kiriatzi (2011) described a similar ~30 cm thick reddish clayey horizon close to the Portes area in the E-SE coast of Aegina, free of microfossils and pedogenic carbonate nodules (Figure 1), which those authors attributed to weathering of volcanic rocks and which was assumed to be Holocene in age.

The underlying Pliocene marls are pale green to off-white or brownish in color. In the northwestern part of the island they are exposed only in road cuts and ravine flanks, as is the overlying Pliocene volcanic clay. According to Benda *et al.* (1979), their maximum thickness reaches 70 m in the area of Ag. Thomas (Figure 1b). In this area the Pliocene volcanic clay is missing and the marls are overlain directly by unaltered

tuff and tuffite followed by andesitic breccias (Benda *et al.*, 1979; Stamatakis and Magganas, 1989).

Mineralogy and mineral textures

Representative photomicrographs of Aeginetan sherds with coarse and fine fabric are shown in Figure 4. More photomicrographs with coarse and fine fabric are shown under the 'Petrographic Database' on the SAVA website. The fine fabric (Figure 4a) is characterized by a texture in which larger crystals of hornblende, biotite, and feldspar are embedded within a finer matrix, consisting of quartz, feldspar, oxyhydroxides, calcite, and Ca-silicates (diopside and gehlenite), the latter formed during firing. The presence of diopside and gehlenite was verified by XRD in the second Kolonna sample set (data not shown). Small porphyritic dacite rock fragments are present (data not shown). The coarse fabric is characterized by the presence of rock fragments of porphyritic dacite and crystals of hornblende, biotite, and feldspar minerals (Figure 4b). The presence of calcite was verified by XRD. High-temperature Ca minerals have not been detected in the sherds with coarse fabric. The coarse fabric is considered to be equivalent to FG1 and the fine fabric is equivalent to FG2 of Gauß and Kiriatzi (2011).

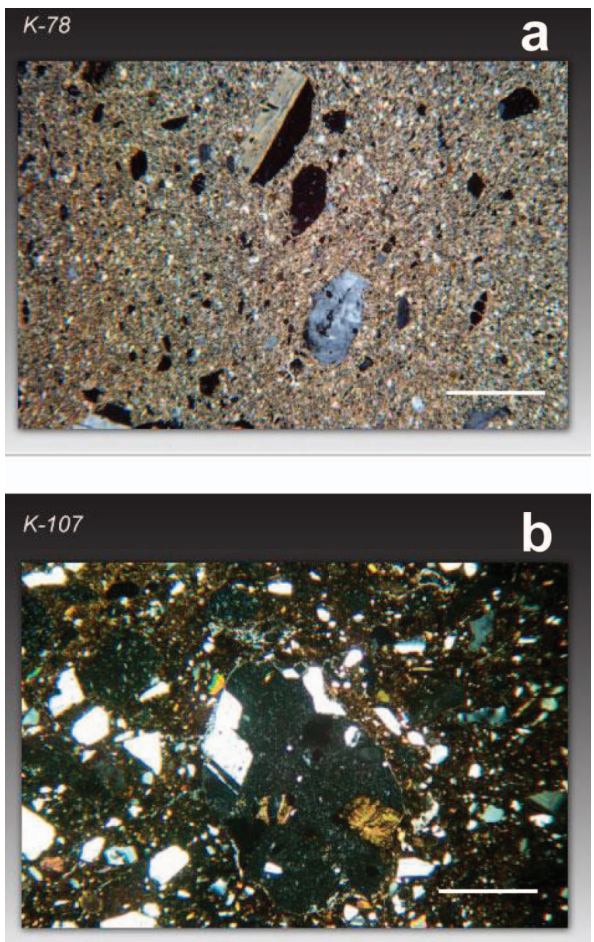

Figure 4. Representative photomicrographs of Aeginetan sherds with fine fabric (a) and coarse fabric (b). Crossed polars. Scale bars = 125 μm.

Typically, the Pliocene volcanic clay consists of quartz, igneous plagioclase (mainly andesine), clay minerals, hornblende, K-feldspar, biotite, calcite, and Fe-oxyhydroxides (Figure 5a). The clay mineral content is, on average, ~25% of the total clay. The composition of the hornblende is comparable to that of the hornblendes from the volcanic rocks of Aegina and of the hornblendes in the volcanic sherds of chemical groups A, E, F, and P of Mommsen (Brophy *et al.*, in press). The Aegina hornblendes have chemical fingerprints (Dietrich *et al*., 1988 and references therein) distinct from those of their counterparts in other volcanic centers of the SAVA, being richer in K_2O (Dorais *et al.*, 2004; Brophy *et al.*, in press; see Brophy's report on the SAVA website). The air-dried clay fraction consists of mica, chlorite, kaolinite, palygorskite, a phase with a diffraction maximum at 14–15 Å, quartz, calcite and feldspars. The 14–15 Å phase after EG solvation splits into two components, a smectitic one which swells to 17.5–17.8 Å and a second phase at 15 Å (Figure 5b). The presence of palygorskite was also suggested in the bulk samples (Figure 5a). The large *d* value of the swollen phase is attributed to the Lorenz polarization factor due to the small particle size of smectite. Smectite (confirmed by EDS analysis not shown) occurs in the form of wavy flakes (Figure 6a). Upon heating at 375ºC, the low-angle peaks collapse to a large one at 10 Å and a minor one at 13.7 Å. This suggests that the second swelling phase corresponds to chlorite-rich, R0 mixed-layer chlorite-smectite (C-S). Fine-grained chlorite and mixed-layer C-S flakes have replaced biotite (Figure 6b), as was suggested by EDS analysis.

Pliocene marl samples from the northwestern part of Aegina Island consist of quartz, calcite, dolomite, albite, gypsum, mica, chlorite, kaolinite, R0 mixed-layer illite-smectite and in places, traces of amphibole, serpentine, and talc (Figure 5a,b). Minor palygorskite is also present in places (Figure 5b). The presence of serpentine and talc suggests that the source material was different from that of the Pliocene volcanic clay and included an ultrabasic component, possibly derived from ophiolite rocks. Ophiolite rocks are common components of the Sub-Pelagonian Unit to which most of the Aeginetan Alpine rocks belong (Dietrich *et al.*, 1991). The Pliocene marl samples differ in many ways, in terms of bulk mineralogy, from the overlying Pliocene volcanic clay: (1) they contain dolomite, serpentine, talc, and gypsum; palygorskite is scarce and they lack mixed-layer C-S and K-feldspar; (2) they contain only trace amphibole (the Pliocene volcanic clay is considerably richer in amphibole) and albite rather than andesine; and (3) feldspars are considerably less abundant than in the Pliocene

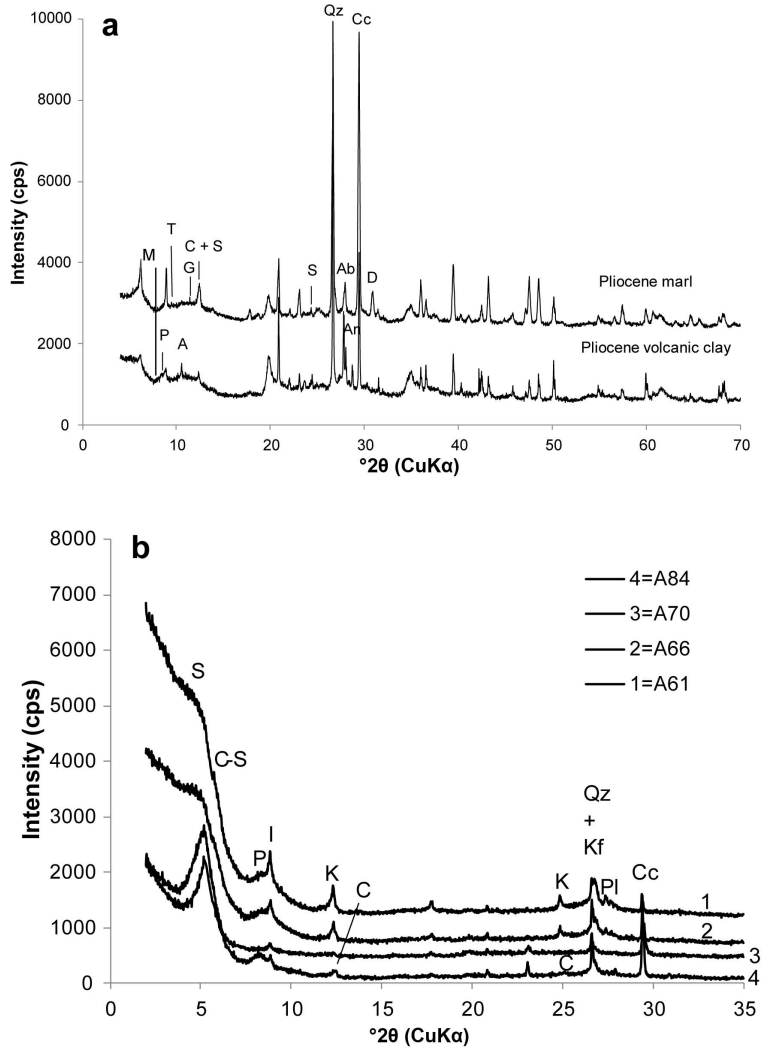

Figure 5. XRD traces of: (a) randomly oriented powdered samples. Symbols: A = amphibole, P = palygorskite, G = gypsum, C = chlorite, S = serpentine, D = dolomite, Ab = albite, An = anorthite, and; (b) of oriented clay fractions after EG solvation of the Pliocene volcanic clays (A61 and A66) and the Pliocene marls (A70, A84). The differences in mineralogy are indicated by symbols. S = smectite, I = illite, P = palygorskite, K = kaolinite, C = chlorite, C-S = mixed-layer chlorite-smectite, Qz = quartz, Kf = K-feldspar, Pl = plagioclase, Cc = calcite.

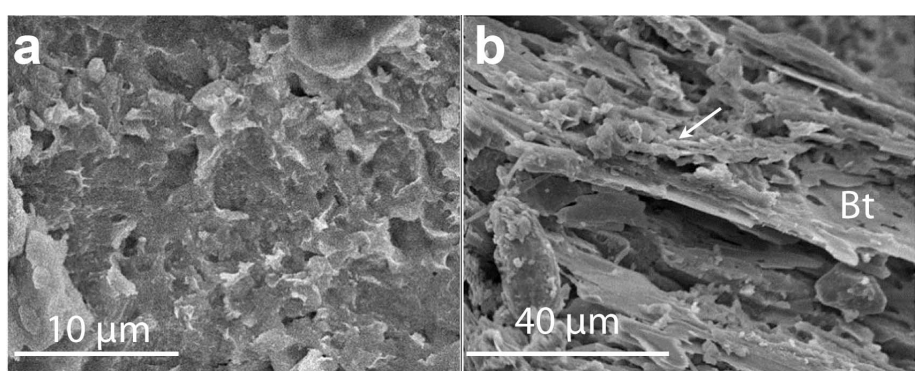

Figure 6. SEM images of the Pliocene volcanic clay: (a) smectite flakes with subhedral morphology; (b) mixed-layer chlorite-smectite and chlorite (shown by arrows), replacing biotite (Bt).

volcanic clay. The absence of opal-A and/or opal-CT suggests that the marl may correspond to the lower zone of the Ag. Thomas section, which is also free of opal-A and/or opal-CT (Stamatakis and Magganas, 1989). The presence of gypsum and dolomite suggests deposition in a shallow-marine depositional environment characterized by intense evaporation in an arid climate. The clay mineralogy of the marl samples is also different from that of the Pliocene volcanic clay: the clay fraction of the Pliocene marl is dominated by R0 mixed-layer illite-smectite with subordinate mica and chlorite and contains abundant calcite, and palygorskite is present in places (Figure 5b). In general the Pliocene marls are richer in clay minerals than the Pliocene volcanic clay. The different mineralogy suggests different sources for the two sediments.

Geochemistry

Mass fractions of major-element oxides, trace elements, and *REE* determined by chemical analysis of the Pliocene volcanic clay and the Pliocene marls are listed in Table 1. The chemical composition of the Plakakia samples used by Hein *et al.* (2004) and the A, E, F, and P groups of Mommsen *et al.* (2001) are listed in Table 2. The two sediment types have distinct chemical compositions, which reflect sediment supply from different sources. In general, the Pliocene volcanic clay has larger SiO_2, Al_2O_3, Fe_2O_3, and TiO_2 contents and smaller MgO, Na_2O, and P_2O_5 contents than the marls (Table 1). The two types also have comparable concentrations of K_2O (Table 1). The large MgO content in the Pliocene marl samples reflects the contribution of dolomite and the ultrabasic component represented by serpentine and talc. The CaO content of the two materials mainly reflects the presence of carbonates and to a lesser degree of plagioclase feldspar in the Pliocene volcanic clay. In general, the Pliocene marl samples are richer in CaO than the Pliocene volcanic clay. However, samples from the Pliocene volcanic clay with abundant calcite nodules which are <2 mm are also rich in CaO. In addition, the two sediment types display significant differences in trace-element chemistry. In general, the Pliocene marls are richer in Ni and Cr than the Pliocene volcanic clay in accordance with the presence of serpentine and talc, due to the ultrabasic input. The Pliocene volcanic clay is richer in high field strength elements (Zr, Nb, Y, Th, and Hf) and poorer in U than the Pliocene marls (Table 1). Moreover, the volcanic clays display heterogeneity which is not explained by calcite dilution; sample A83, which was collected from the north coast of the island, away from the Skotini volcanic center (Figure 1), has a fine grain size and is geochemically different from the remaining volcanic clay samples, being poorer in Ba, Th, Sr, the light *REE* (*LREE*), and Y, but not in the heavy *REE* (*HREE*) and Sc, and richer in Ni and Co.

The differences in geochemical composition were used to separate the two sediment types with geochemical plots. In the present study the concentration ratios were used instead of elemental concentrations to avoid possible problems with concentration dilution by calcite. Based on the geochemical data, MgO and P_2O_5 are important discriminating elements, which separate the two sediment types according to their chemical composition. The different geochemical signatures of the two sediment types are evident from geochemical plots of the Al_2O_3/MgO *vs*. SiO_2/MgO (Figure 7a) and Al_2O_3/P_2O_5 *vs*. SiO_2/P_2O_5 elemental ratios (Figure 7b).

Concentration ratios of certain trace elements are also useful for separation of the two sediment types (Figure 8). These diagrams also include the Plakakia clays (Hein *et al.*, 2004) and the sherd groups A, E, F, and P of Mommsen *et al.* (2001). The average compositions of the different horizons were also plotted. Note that Gauß and Kiriatzi (2011) considered the Plakakia clays to be Pliocene marls. The concentration ratios of trace elements have often been used in diagrams for analysis of sedimentary processes and provenance analysis of sedimentary rock units at a large scale (*e.g.* McLennan and Taylor, 1991; McLennan *et al.*, 1993). The Th/Sc and Th/Co ratios are indicative of differences

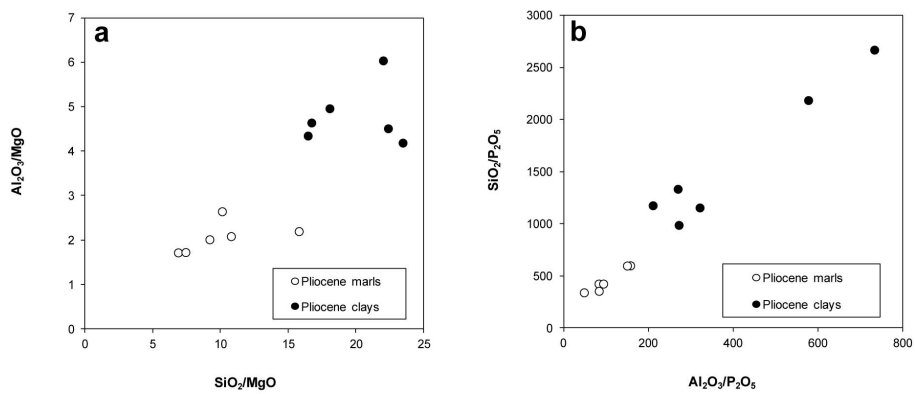

Figure 7. Geochemical plots for discrimination of the Pliocene marl and Pliocene volcanic clay: (a) SiO_2/MgO *vs*. Al_2O_3/MgO; (b) Al_2O_3/P_2O_5 *vs*. SiO_2/P_2O_5.

Table 1. Chemical composition (wt.%) of the Pliocene volcanic clay and the Pliocene marl samples from Aegina Island.

	Pliocene clays						Pliocene marls					
	A61	A62	A66	A58L	A58U	A83	A70	A73	A78B	A84	C8	N2
SiO_2	46.31	47.15	43.77	53.45	29.71	53.48	34.18	36.13	38.45	37.74	36.03	39.35
TiO_2	0.64	0.5	0.6	0.73	0.39	0.65	0.39	0.38	0.49	0.33	0.52	0.52
Al_2O_3	12.83	8.4	11.54	14.66	8.14	10.76	6.58	9.41	8.38	5.23	8.96	9.1
Fe_2O_3	5.64	4.28	5.33	6.51	3.23	5.89	3.63	4.28	5.11	3.27	4.46	4.88
MnO	0.08	0.07	0.07	0.09	0.05	0.08	0.03	0.05	0.07	0.02	0.05	0.06
MgO	2.77	2.01	2.66	2.96	1.35	2.39	3.17	3.57	4.18	2.39	5.24	5.3
CaO	11.26	16.59	12.42	4.54	27.95	7.63	21.94	18.82	18.67	24.35	18.13	16.11
Na_2O	0.58	0.5	0.62	0.67	0.46	0.54	0.7	1.04	0.8	0.56	0.83	0.77
K2O	1.82	1.41	1.7	2.19	1.21	1.63	0.91	0.55	1.64	0.84	1.65	2
P_2O_5	0.04	0.04	0.02	0.02	0.03	0.04	0.08	0.06	0.09	0.11	0.06	0.11
Cr_2O_3	0.033	0.107	0.041	0.041	0.023	0.08	0.039	0.019	0.052	0.042	0.048	0.05
LOI	17.7	18.8	21	13.9	27.3	16.7	28.2	25.4	21.9	24.9	23.7	21.6
Total	99.7	99.86	99.77	99.76	99.84	99.87	99.85	99.71	99.83	99.78	99.68	99.85
Concentrations (ppm)												
Ba	283	154	241	327.3	187.2	184	162	288	154	211	193	167
Ni	135	181	148	175	81	253	165	80	325	172	228	249
Sc	14	10	13	17	8	15	9	11	13	9	13	14
Mo	0.9	0.5	0.7	0.8	0.5	0.6	0.1	0.2	1.5	4.1	29.5	3
Cu	21.7	16.5	21.6	29.1	20.9	26.2	17	15.8	28.4	25	26.4	30.8
Pb	14.4	9.8	12.3	16.7	8.8	9.3	6.2	7.2	10.7	4.7	14.5	15.4
Zn	52	33	52	70	30	47	30	22	61	33	73	70
As	6.2	16.5	6.5	7.7	13.1	13.8	2.1	2.4	7.2	8.3	5.1	5.7
Cd	0.2	0.2	0.2	0.1	0.1	0.1	0.1	0.1	0.1	0.6	0.1	0.2
Sb	0.2	0.1	0.2	0.2	0.2	0.1	0.1	0.1	0.3	0.1	0.2	0.3
Ag	0	0	0	0	0	0	0	0	0	0	0.1	0.1
Au*	14	6.7	3.4	12	17.4	3.8	4.2	11.7	7.1	4.4	1.6	2.5
Hg	0	0.01	0.01	0.01	0.01	0	0.01	0.02	0.01	0.01	0.02	0.04
Tl	0.3	0.2	0.3	0.3	0.2	0.2	0.1	0.1	0.2	0.1	0.2	0.2
Se	0	0	0.5	0	0.5	0	0.5	0	0.5	0	0	0
Be	0	0	0	1	0	0	0	0	0	0	0	0
Co	20.3	18.5	17.5	21.5	10.4	22.5	12.1	14	28.1	11.9	18.6	26.1
Cs	6.5	5.6	5.9	8	3.9	6.9	5.9	1.9	6.8	5.8	7.6	8.4
Ga	15.2	10.5	14	19.2	10.6	13	8.4	9.7	10.6	7.1	11.1	12.2
Hf	3.9	4.5	3.9	4.8	3.1	4.3	1.9	1.9	2.3	2.1	2.3	2.5
Nb	11.5	8	10.2	14.4	8.7	10.9	5.4	4.5	6.5	4.9	7.5	7.7
Rb	74.4	59.4	66.4	96.8	52.5	75.5	40	20.2	64.1	41.9	71.3	75
Sn	2	1	2	3	2	2	1	0	1	1	0	0
Sr	323.8	515.4	355.6	273.2	719.8	237.6	335.1	707.9	350.9	506.4	435.3	308.5
Ta	0.8	0.7	0.8	1	0.5	0.7	0.4	0.4	0.5	0.4	0.5	0.6
Th	9.5	7.6	8.2	11	7.9	6.8	4.5	6	5.7	3.9	5.4	5.1
U	1.4	1.9	1.4	1.7	1.2	1.5	1.7	1.8	2.4	3.2	6.3	3.5
V	92	79	85	118	69	108	64	74	77	83	78	87
W	1.4	0.7	1.3	1.3	0.8	1.5	0.5	0.5	0.8	1	0	0
Zr	127.2	138.7	132.5	164.2	109	148.3	69.6	65.7	77.6	81.4	82.9	83.1
Y	23.6	17.8	18.8	18.7	18.5	17.4	13.3	11.4	17.5	16	18.2	20.9
La	28.7	21.6	22	22.6	20.1	19.2	13.3	13.3	15.8	12.7	18	18.8
Ce	57.2	45.9	49.7	65.4	42.1	46.2	24.8	27.3	30.5	25.5	33.4	34.3
Pr	6.65	4.7	5.2	5.58	4.67	4.56	3.14	3.02	3.67	3.04	4.12	4.3
Nd	24.6	19.5	19.6	22.9	20	17.5	12.4	12.9	13.6	12.7	17.4	17.9
Sm	5.1	3.5	4.1	4	3.6	3.5	2.5	2.5	3.5	2.5	3.6	3.9
Eu	1.05	0.76	0.83	0.83	0.75	0.73	0.61	0.62	0.68	0.57	0.8	0.84
Gd	4.1	3.01	3.3	3.07	3.22	2.86	2.23	2	2.8	2.17	3.02	3.55
Tb	0.77	0.57	0.63	0.55	0.49	0.6	0.39	0.41	0.5	0.47	0.49	0.53
Dy	3.85	2.96	3.1	3.2	2.91	2.83	2	1.92	3	2.44	3.03	3.29
Ho	0.8	0.57	0.63	0.63	0.56	0.64	0.44	0.41	0.57	0.56	0.61	0.64
Er	2.33	1.63	1.81	1.84	1.59	1.74	1.22	1.12	1.55	1.38	1.7	1.8
Tm	0.36	0.26	0.32	0.3	0.27	0.3	0.21	0.16	0.26	0.27	0.26	0.28
Yb	2.36	1.64	2.15	2.11	1.59	1.84	1.21	1.23	1.8	1.43	1.6	1.88
Lu	0.38	0.26	0.36	0.32	0.25	0.33	0.19	0.18	0.25	0.25	0.26	0.29

* Concentration in ppb.

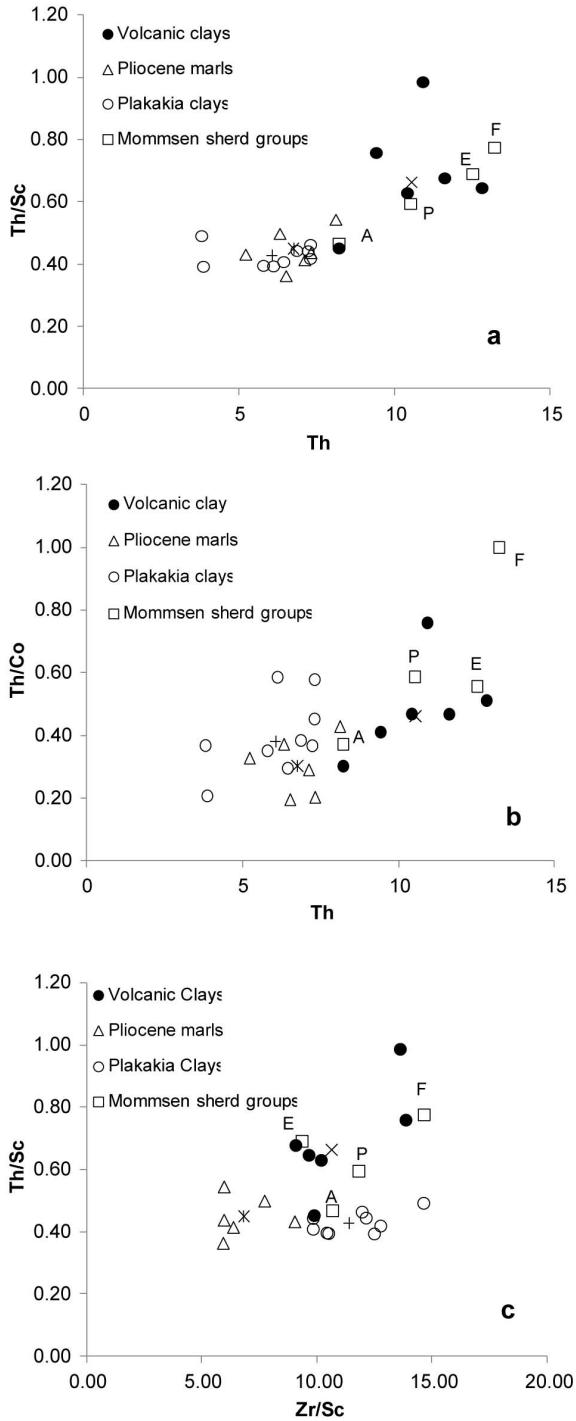

Figure 8. Trace-element concentration ratios of the Pliocene volcanic clay, the Pliocene marl, and the Plakakia clays (Hein *et al.*, 2004). (a) Th/Sc *vs*. Th; (b) Th/Co *vs*. Th; (c) Zr/Sc *vs*. Th/Sc. The trace-element composition from the A, E, F, and P groups of the Aeginetan sherds (Mommsen *et al.*, 2001) are plotted as solid squares with the Pliocene volcanic clay. + = mean composition of the Plakakia clays, × = mean composition of the Pliocene volcanic clay and ⚹= mean composition of the Neogene marls. See text for discussion.

in bulk composition between rocks, because Th is an incompatible element in igneous processes, whereas Sc, Co, and Ni are compatible elements and are transported in terrigenous sediments during sedimentary processes (McLennan *et al.*, 1993). The Zr/Sc ratio is also indicative of zircon enrichment, with Zr being present in zircon and Sc, while not hosted in zircon, is indicative of provenance. The Pliocene volcanic clays are separated from the Pliocene marls by having greater Th/Sc and Zr/Sc ratios. The Plakakia clays in general have similar Th/Sc and Th/Co ratios to the Pliocene marls suggesting a common provenance (Figure 8a,b). The Zr/Sc ratio is greater, however, indicating a larger zircon content in the Plakakia clays (Figure 8c), in accordance with the reported heterogeneity of the Pliocene marls (Benda *et al.*, 1979). The Mommsen sherd groups plot in the same area as the Pliocene volcanic clay, with sherd group A plotting at the boundary with the plotted areas of the Plakakia clays and the Pliocene marls. The volcanic clay sample, A83, has smaller Th/Sc and Th/Co ratios than the remaining volcanic clay samples and plots very close to sherd group A, confirming that the volcanic clay is also geochemically heterogeneous.

The Pliocene volcanic clay is significantly enriched in *REE* compared to the Pliocene marl samples, as indicated in the chondrite-normalized plot (Figure 9). The Pliocene volcanic clay has a greater Ce/Yb ratio

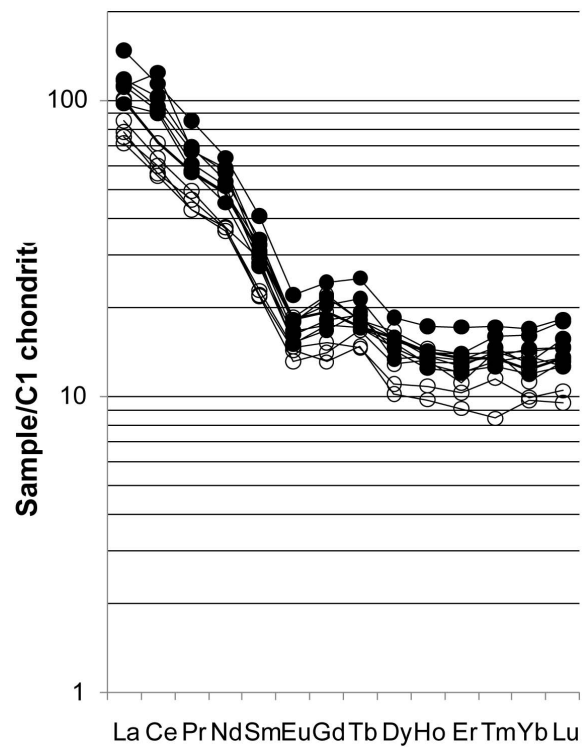

Figure 9. Chondrite-normalized *REE* plots of the Pliocene volcanic clay (black circles) and the Pliocene marl (open circles). See text for discussion.

Table 2. Chemical compositions of the A, E, F, and P chemical groups of Mommsen *et al.* (2001), and the Pliocene marls from the Plakakia area (Hein *et al.*, 2004).

	Mommsen Aeginetan sherd Groups				Marls from the Plakakia area					
	A	E	F	P	Plaka1	Plaka2	Plaka3	Plaka7	Plaka8	Plaka9
Concentrations (%)										
Ti	0.39	0.41	0.35	0.40	0.23	0.26	0.18	0.17	0.22	0.28
Fe	4.15	3.61	4.09	5.03	2.96	1.70	3.26	1.43	3.16	3.62
Ca	11.00	8.50	3.20	3.70	10.40	22.60	9.80	25.20	10.30	8.00
Na	1.04	1.28	1.90	1.70	1.08	0.49	0.69	0.45	1.23	1.58
K	1.98	2.37	1.89	2.04	0.98	0.65	1.29	0.58	1.35	1.26
Concentrations (ppm)										
Ba	306	387	540	630	114	110	128	30	98	114
Ni	332	255	58	89	284	187	354	149	288	347
Cr	402	322	71	126	401	215	407	175	397	470
Sc	16.1	14	14.8	20.3	11.4	7.2	13.7	5.6	12.7	12.6
Zn	90	86	73	84	62	35	74	33	73	76
As	9.3	8.4	7.5	4.7	4.2	1.7	5.2	1.3	10.8	2.2
Sb	0.77	0.64	0.36	0.50	0.54	0.29	0.75	0.27	0.79	0.65
Co	20.3	17.4	11.5	20.6	12.9	13.7	12.7	7.5	10.2	14.6
Cs	5.69	5.79	4.77	5.54	4.15	2.69	5.4	2.43	6.14	5.91
Hf	4.06	4.18	5.35	5.39	2.98	1.80	3.34	1.64	3.25	3.28
Rb	74	84	83	97	47	32	63	27	68	61
Ta	0.65	0.66	0.80	0.87	0.43	0.27	0.56	0.23	0.55	0.48
Th	7.55	9.69	11.50	12.10	4.53	2.84	5.75	2.76	5.90	5.61
U	2.14	2.15	1.67	1.93	1.20	0.83	1.51	0.59	1.51	3.67
W	n.a.	n.a.	n.a.	n.a.	1.13	0.78	1.07	0.66	1.39	1.40
Zr	172	131	217	240	119	90	175	82	152	153
La	22.2	24.1	26.7	28.6	16	12.5	15.9	13	17.3	17.5
Ce	46.1	48.6	60.8	63.5	31.2	22.8	36.1	24.4	33	35.1
Nd	20	19.6	21.5	25	7.9	9.3	12.8	8	14.3	19.2
Sm	3.8	3.62	4.43	4.55	2.69	1.76	2.73	1.59	2.82	2.93
Eu	0.94	0.96	1.12	1.16	0.73	0.53	0.75	0.49	0.76	0.74
Tb	0.57	0.57	0.64	0.66	0.52	0.41	0.47	0.35	0.51	0.53
Yb	2.3	2.23	2.58	2.67	1.94	1.55	1.78	1.35	1.79	0.26
Lu	0.35	0.35	0.39	0.43	0.29	0.22	0.28	0.18	1.89	0.28

n.a. = not available.

than the Pliocene marl (Table 1). The Plakakia samples have *REE* concentrations similar to the Pliocene marl samples, in agreement with the common provenance of the two sediments (Tables 1, 2). The enrichment of *REE* in the volcanic clay is due partially to dilution from calcite, but it also reflects differences in the non-carbonate sources. This is because the Pliocene volcanic clay samples A62 and A58U, which are rich in CaO, have greater abundances of *REE* (especially of the *LREE*) than the Pliocene marls with comparable CaO contents (Table 1). As mentioned previously, the *REE* data have been recalculated on a volatile-free basis. Hence, the lower abundance of *REE*, especially the light *REE* of the Pliocene marl samples, is partly attributed to the contribution of the ultrabasic component, as indicated by the presence of serpentine and talc. The *REE* concentrations of the Pliocene volcanic clay samples, after correction for dilution by calcite, are comparable to those of the volcaniclastic dacitic volcanic rocks of the island (Tables 1, 3).

Table 3. *REE* concentrations (ppm) of the Aeginetan dacitic volcaniclastic flows.

	Aeginetan dacitic epiclastic flows and altered dacites			
	A76	A81A	A81B	C5
La	20.7	30.4	25.1	27
Ce	46.5	75.3	59.4	48.9
Pr	4.42	7.2	5.66	5.65
Nd	17.2	28.1	22	22.9
Sm	3.3	5.7	4.5	4.3
Eu	0.81	1.06	1.04	0.98
Gd	3.23	4.5	3.72	3.56
Tb	0.55	0.86	0.66	0.52
Dy	3.18	4.45	3.61	3.16
Ho	0.65	0.83	0.7	0.66
Er	2	2.53	2.1	1.85
Tm	0.29	0.41	0.36	0.29
Yb	1.97	2.76	2.08	2.04
Lu	0.34	0.47	0.37	0.34

DISCUSSION

The Pliocene volcanic clay as a possible source of the Aeginetan ceramics

The two clay-rich sedimentary horizons present in the northwestern part of Aegina display distinct mineralogical and geochemical characteristics which reflect different sources and depositional environments. The Plakakia clays (Hein *et al.*, 2004) are actually Pliocene marls as shown in the previous section (*cf.* Tables 1, 2), in agreement with the suggestion of Gauß and Kiriatzi (2011) and this is reflected in the mineralogical and geochemical signatures of the sediments, which display different patterns (Figures 7–9). This evidence does not address the issue of which of these sediments was the source for ancient Aeginetan Ware, however. That question requires a comparison of the geochemistry and mineralogy of selected Aeginetan Ware sherds with the source-clay data.

The different *REE* patterns and the concentration ratios of the two sediment types studied have been utilized as part of the compelling evidence that shows that the Pliocene volcanic clay was the main raw material used for the fabrication of Aeginetan ceramics in the Bronze Age represented by the A, E, F, and P groups of Mommsen *et al.* (2001) (Figures 8, 10). The *REE* of the sherds derived from different types of ceramics plot in the same field as the samples from the Pliocene volcanic clay (Figure 10a). The *REE* geochemical characteristics of the Neogene marls (Figure 10b) do not match those of the ceramic articles for groups A, E, F, and P in the database of Mommsen *et al.* (2001). According to their trace-element composition, the Aeginetan sherds of groups E, F, and P (Mommsen *et al.*, 2001) have comparable affinities with the Pliocene volcanic clay and are distinctively different from the Pliocene marls, including the Plakakia clays of Hein *et al*. (2004). The comparison with the existing data of Mommsen *et al.* (2001) for Aeginetan sherd material demonstrates that, at least from a geochemical point of view, the main source material for Aeginetan Ware might have been the Pliocene volcanic clay. The *REE* data suggest that the Pliocene volcanic clays might have been the raw materials used for the manufacture both of the fine- and the coarse-grained Aeginetan ceramics (Figure 10a).

The Aeginetan sherds of group A (Mommsen *et al.*, 2001) plot separately from the other three groups, in the margin of the plotting area of the volcanic clay samples and in contact with the Pliocene marls and the Plakakia clays (Figure 8). Moreover, the Th/Sc and Th/Co ratios of group A sherds are comparable to those of the Plakakia clays and sample A83 of the volcanic clays. This indicates that the source materials of this sherd group might either be a mixture of the volcanic clay and Pliocene marl at a ratio of ~0.3:0.7 to ~1:1, considering the average compositions of the sediment types (Figure 8), or it could be a volcanic clay with composition similar to that of sample A83. The suggestion of mixing between the Pliocene marls and a small amount (up to 20%) of volcanic clay was invoked by Gauß and Kiriatzi (2011) for FG2 sherds in that study, which were considered to be equivalent to Mommsen's sherd groups A and E. Although the mixed-sources scenario may be valid, however, it has three shortcomings. First, the sherd group E of Mommsen *et al.* (2001), included in the FG2 sherds (Gauß and Kiriatzi, 2011), clearly has

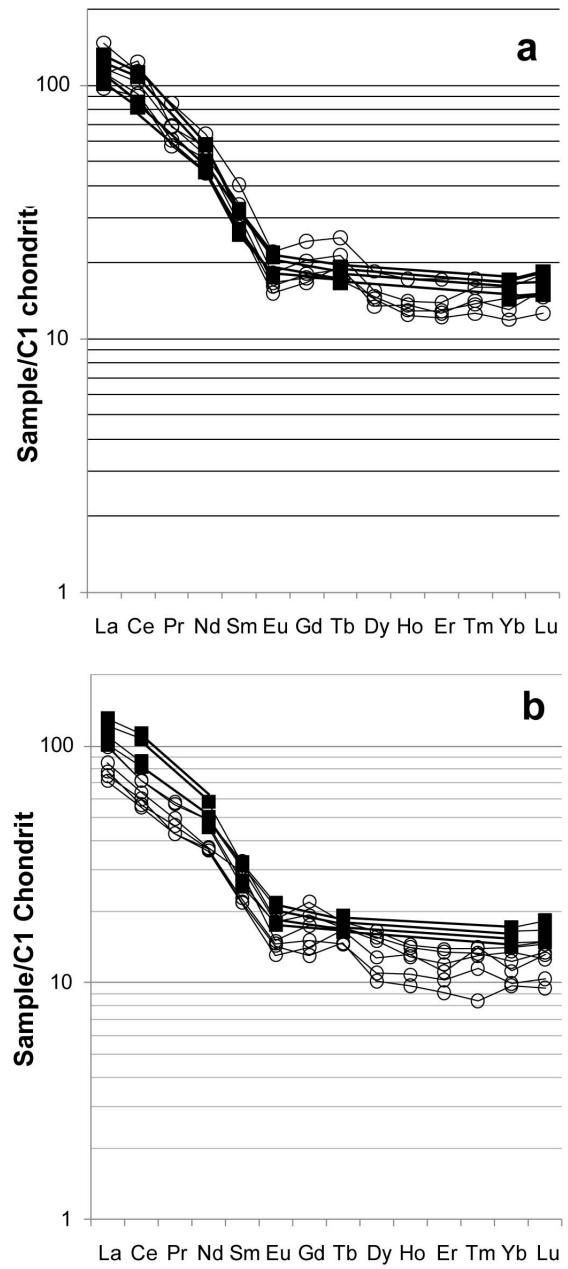

Figure 10. Chondrite-normalized *REE* plots of the Aeginetan sherd groups A, E, F, and P of Mommsen *et al.* (2001) (solid squares) and (a) the Pliocene volcanic clay and (b) the Pliocene marl. See text for discussion.

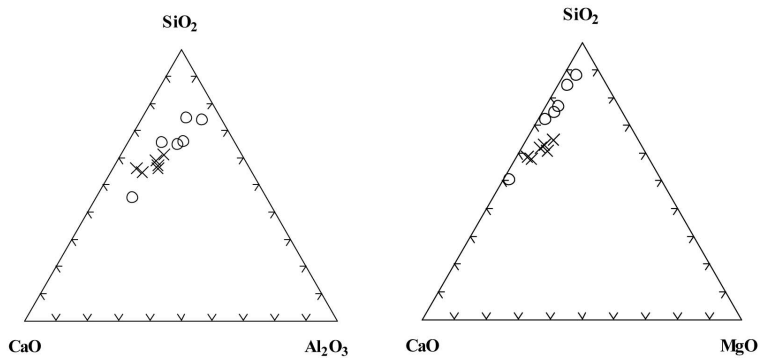

Figure 11. SiO_2-CaO-Al_2O_3 and SiO_2-CaO-MgO plots for the Pliocene volcanic clay (○) and the Pliocene marl (×). See text for discussion.

geochemical affinities typical of the Pliocene volcanic clays (Figure 8, 10). Second, volcanic clay samples are found with geochemical characteristics similar to sherds of group A (*e.g.* sample A83). Third, if there had been mixing then the group A sherds would have had coarse volcanic fragments, which is not the case. This suggests that the volcanic clay would have been processed possibly by levigation prior to mixing. Hence, use of the Pliocene marls, or their equivalent Plakakia clays, might not have been necessary, at least as main components of the ceramic mass, and also for the sherds of group A.

Mineralogy is a less sensitive tool for discrimination purposes, because in most sedimentary basins clastic sediments are supplied from common precursor rock types. The role of mineralogy may become more significant if volcanic or chemical sediments are important components of the sediments. In such cases, the sources of non-clastic sediments should be recognized. However, the mineralogical composition of the raw materials affects the firing characteristics and the properties of the ceramics, with the presence or lack of calcite being a significant controlling parameter (Peters and Iberg, 1978; Cultrone *et al.*, 2001; Traoré *et al.*, 2003; Trindade *et al.*, 2010). The Pliocene volcanic clay yielded end products without a significant degree of melting and abundant high-temperature phases after firing up to 1050ºC (Shriner *et al.*, in press). Firing of the Pliocene marls produced significant amounts of melt and deformation of the ceramics after prolonged firing at ~1000ºC (C. Shriner, unpublished data).

The two sediment types plot in the same areas in the SiO_2-CaO-Al_2O_3 and the SiO_2-CaO-MgO ternary diagrams, with the Pliocene marl samples plotting closer to the CaO corner due to their greater CaO contents (Figure 11). At firing temperatures of >800ºC the Pliocene marl samples yield end products with similar Ca-silicates to the Pliocene volcanic clay (diopside and gehlenite). However, at lower temperatures, calcite disappears at 700ºC after 3 h of firing in the Pliocene marls (Figure 12), whereas, in the Pliocene volcanic clay it persists up to 900ºC (Shriner *et al.*, in press). The

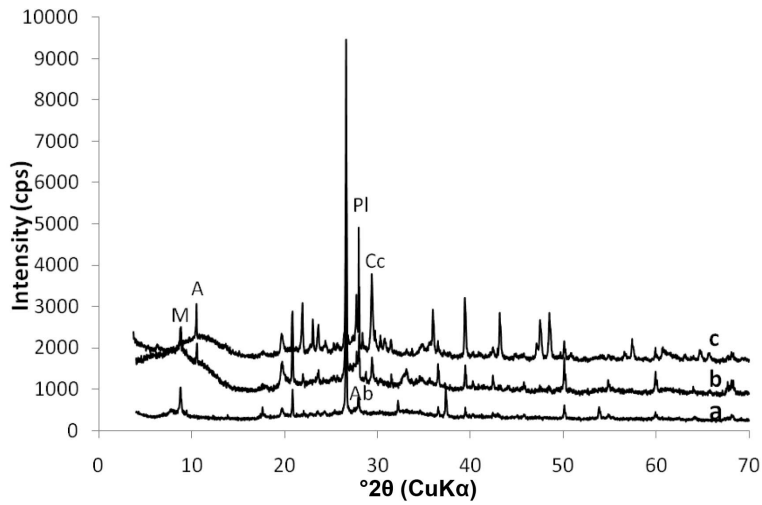

Figure 12. XRD traces of (a) Pliocene marl fired at 700ºC for 3 h; (b) Pliocene volcanic clay fired at 700ºC for 3 h; and (c) Aeginetan sherd from Felten/Berger collection fired at low temperature. Note the striking similarity between traces b and c. See text for discussion. A = amphibole, M = mica, Pl = plagioclase, Ab = albite, Cc= calcite.

mineralogical composition of the Bronze Age Aeginetan ceramics fired at low temperatures is comparable with the Pliocene volcanic clay, not the Pliocene marl, both fired at 700ºC (Figure 12). It seems that the Aeginetan ceramists were using the Pliocene volcanic clay for its special firing properties, and were targeting special temperature-time ranges, which were different for the coarse- and fine-grained ceramics (Shriner *et al.*, in press).

Comparison of the geochemical correlation with existing statistical methods

The geochemical correlation of the Pliocene volcanic clay and the Pliocene marls involved a correction for dilution of calcite by recalculation of the major and trace-element concentrations for LOI, so that the geochemical features of the different sediment types could be comparable. Correction is only partial, for two reasons, however. First, it accounts only for the CO_2 but not for the CaO of the calcite and dolomite, the latter being present in the Pliocene marls. Second, LOI includes the weight loss due to dehydroxylation of phyllosilicates including the clay minerals. The Pliocene marls are richer in clay minerals than the Pliocene volcanic clay. Therefore, part of the greater LOI is due to the greater H_2O loss during dehydroxylation, which partly counterbalances the greater CaO content of the marls due to carbonates. With the existing data it is not possible to estimate the relative contribution of the dehydroxylation of phyllosilicates to the LOI.

The methods used so far for correction of calcite dilution for grouping of pottery sherds use the concentration ratios instead of elemental concentrations (Buxeda i Garrigos, 1999) and the "best relative fit factor" (Beier and Mommsen, 1994; Mommsen, 2004). Although concentration ratios overcome the problem of calcite dilution, they reduce the available degrees of freedom in the system and hence reduce the significance of the geochemical information available for discrimination/correlation purposes, in the same manner as two lines having the same slope may be parallel and may not coincide. Moreover, the ratios may lead to erroneous assumptions when applied to distinguish geologic formations in a sedimentary unit. Indeed, different abundances of two hypothetical elements A and B in two distinct rock types may yield comparable elemental ratios and, hence, misleading results. Careful selection of concentration ratios is necessary, therefore, which in the case of sedimentary formations should have geochemical/geologic significance, such as those frequently used in diagrams for analysis of sedimentary processes and provenance analysis of sedimentary rock units at a large scale (*e.g.* McLennan and Taylor, 1991; McLennan *et al.*, 1993). In the present study the use of carefully selected concentration ratios helpful in understanding geologic processes (Th/Sc, Th/Co, Zr/Sc) provided indications of the use of the Pliocene volcanic clay as the main source of Aeginetan ceramics. The results are meaningful because the two main sediment types in Aegina have different origins and geotectonic affinities (volcanic *vs*. clastic). Scandium has been used to normalize geochemical data prior to multivariate analysis in archeometric pottery studies (Dias and Prudencio, 2008), although the observed trends and deviations from these trends were not addressed in detail. As quartz and calcite are essential components of the source rocks in Aegina, corrections during provenance analysis are necessary only if there is evidence that they are present as tempers in the sherds, which is not the case. Detailed petrographic analysis has shown that the calcite nodules in FG1 Aeginetan ceramics are pedogenic (Gauß and Kiriatzi, 2011), *i.e.* mineralogical constituents of the sediments, in accordance with the present study (Figure 3).

Similarly the best relative fit factor may not yield reliable conclusions if a significant proportion of the calcite or quartz present in the sherds is not temper. Hein *et al.* (2004) applied a best relative fit factor to the elemental composition of sherd groups A, E, F, and P of Mommsen *et al.* (2001) and concluded that the Plakakia clays have geochemical similarity with the group A sherds, but not with sherds from groups E, F, and P. After application of the same statistical approach to the Pliocene volcanic clay the concentrations of all elements other than Na and Sb showed differences of $<2\sigma$. The Na and Sb showed differences slightly greater than 2σ (Figure 13a). Likewise, in the Pliocene marls, all elements other than Hf showed differences of $<2\sigma$. Following the reasoning of Hein *et al.* (2004), all three sediments could be considered as the raw materials for group A sherds. The Pliocene volcanic clay displays very good geochemical similarity with sherd groups E, F, and P, suggesting that the Pliocene volcanic clay could well be the source of all the Aeginetan sherds. Indeed in the case of group E the concentrations of all elements except for Na and Sb showed differences of $<2\sigma$ (Figure 13b). In the case of the P group the concentrations of all elements except for Na and Sb showed differences of $<2\sigma$ (Figure 13c). Finally, in the F-group sherds the concentrations of all elements except for Na showed differences of $<2\sigma$ (Figure 13d). The difference observed for Na and Sb was also valid for the Pliocene marls, which are equivalent to the Plakakia clay, and is attributed to analytical constraints, *i.e.* the analytical method used probably underestimated the Na and Sb contents of the rocks.

Application of the 2-tailed t-test to the Pliocene volcanic clay data and the fitted group A, E, P, and F data as hypothetical means showed a 5% level of significance for most elements. A 1% level of significance was observed for K, Ni, U, and Zn in the A group, for U and Zn in the E group, for As, Ni, and Cs in the P group and for Cs in the F group. For Na and Sb the test showed significant differences in all groups due to the

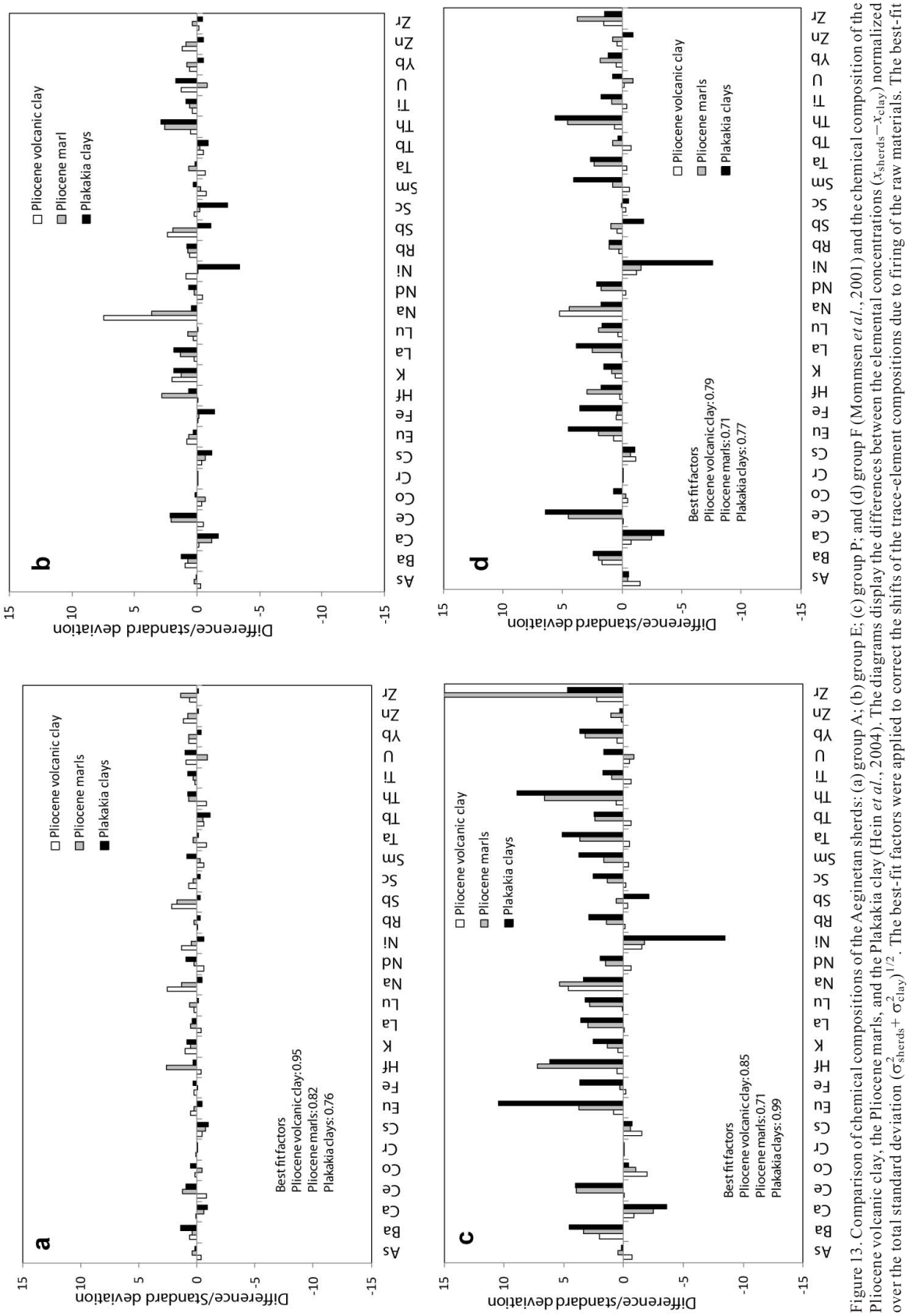

Figure 13. Comparison of chemical compositions of the Aeginetan sherds: (a) group A; (b) group E; (c) group P; and (d) group F (Mommsen *et al.*, 2001) and the chemical composition of the Pliocene volcanic clay, the Pliocene marls, and the Plakakia clay (Hein *et al.*, 2004). The diagrams display the differences between the elemental concentrations ($x_{sherds} - x_{clay}$) normalized over the total standard deviation $(\sigma^2_{sherds} + \sigma^2_{clay})^{1/2}$. The best-fit factors were applied to correct the shifts of the trace-element compositions due to firing of the raw materials. The best-fit factors for the Plakakia clays are from Hein *et al.* (2004).

analytical constraints noted previously. Finally, the test showed significant differences between the sherds and the Pliocene volcanic clay for Ba, Ni, and Zr in groups P and F. The different Ba, Ni, and Zr contents of the F and P groups of Mommsen *et al.* (2001) relative to the Pliocene volcanic clay are attributed to the presence of a slightly different volcanic component, the possible product of a different volcanic eruption from the same volcanic centre. Hence, application of the best relative fit factor (Beier and Mommsen, 1994) yielded satisfactory results for sherd groups E, F, and P as it excluded the Plakakia clays as a possible source of these sherds (Hein *et al.*, 2004). Nevertheless, it did not yield an unequivocal conclusion about the source of group-A sherds because, apart from the Pliocene volcanic clay, both the Plakakia clays and their equivalent Pliocene marls could also be considered as source materials.

As an independent test of evidence, canonical discriminant analysis and principal component analysis (PCA) were applied to identify any possible relationships between the three sedimentary horizons under consideration, *i.e.* the Pliocene volcanic clay, the Pliocene marls and the Plakakia clays, with the A, E, F, and P sherd groups of Mommsen *et al.* (2001). Both analyses were performed with the *SYSTAT* version 8.0 code. Geochemical fingerprinting with multivariate statistical methods has been used to distinguish between or to correlate clay horizons such as bentonites, which may extend over large areas (Huff *et al.*, 1991) and can be used in exploration for economic clay deposits (Christidis, 2001).

Nineteen trace elements (As, Ba, Ce, Co, Cr, Cs, Hf, La, Lu, Nd, Ni, Rb, Sc, Sm, Ta, Th, U, Zn, and Zr) and one minor element (Ti) were selected for the analysis (variables), based on the availability of data in Mommsen *et al.* (2001) and Hein *et al.* (2004) and their geochemical affinity (compatible *vs*. incompatible during igneous processes). The plot of the discriminant scores, using the first two discriminant functions, is shown in Figure 14a. The boundaries of the different fields of the horizons correspond to the lines of equidistance between group means. The first two discriminant functions explain 94.9% of the total variance among the samples. The three different sedimentary horizons are clearly separated and the A, E, F, and P sherd groups of Mommsen *et al.* (2001) plot very close to the Pliocene volcanic clays. When Cr is not included in the analysis, the four sherd groups coincide entirely with the Pliocene volcanic clays (data not shown). Separation of the sherd discriminant scores and the scores of the Neogene marls and the Plakakia clays occurs along both discriminant functions (Figure 14a). Similar results were obtained from the plot of the scores for the first two principal components obtained from the PCA (Figure 14b). In this analysis the first principal component accounts for 64% of the variance of the data and the second component for 18% of the variance. The Pliocene marls and the Pliocene volcanic clays clearly plot in the same area, separately from the Pliocene volcanic clays. The A, E, F, and P sherd groups of Mommsen *et al.* (2001) plot with (groups A and E) or close to (groups P and F) the Pliocene volcanic clays.

Nevertheless, although the canonical discriminant analysis clearly indicates that the Pliocene volcanic clays might be the only source for the A, E, F, and P sherd groups of Mommsen *et al.* (2001), the Plakakia clays plot as a clearly different horizon from the Pliocene marls, which should not be the case. Moreover, in the PCA, the P and F sherd groups of Mommsen *et al.* (2001) plot at the margins of the Pliocene volcanic clays plotting area, although detailed petrographic analysis has shown that they have typical Aeginetan volcanic fabric (Gauß and Kiriatzi, 2011 and the present study). These remarks indicate that statistical analysis of the chemical data alone may not be sufficient for similar studies, because they do not take into account compositional variations within geologic formations, and underline the necessity for thorough geologic-

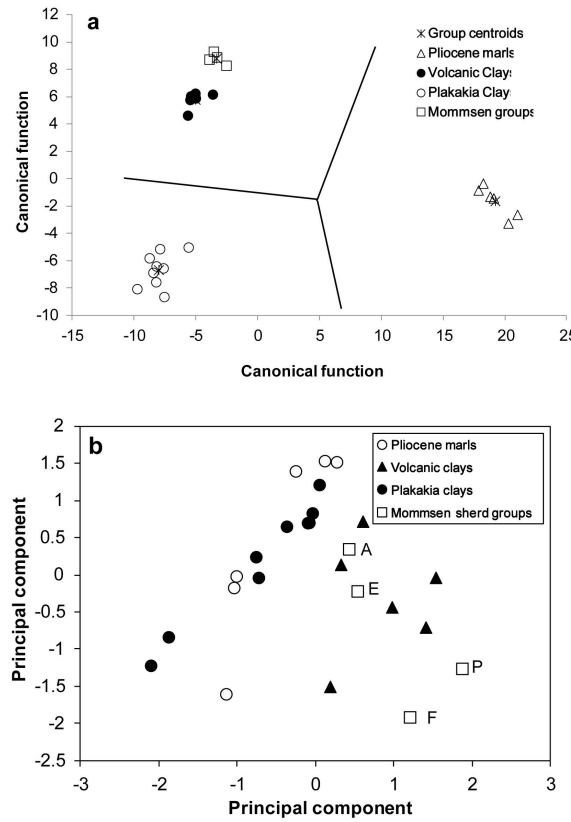

Figure 14. (a) Canonical discriminant plots of the samples using the first two discriminant functions. The plot clearly separates the three sediment types. See text for discussion. (b) Principal component analysis plots of the scores for the first two principal components. The plot separates the Plakakia clays and the Pliocene marls from the Pliocene volcanic clay. See text for discussion.

mineralogical-geochemical investigation of the potential source rocks of ancient ceramics during provenance analysis, which is discussed below.

Development of an integrated geoarcheological provenance model and approach

The characterization of ceramic articles with petrographic techniques and chemical analysis of major and especially trace elements are important tasks in modern archeological science (Middleton and Freestone, 1991; Mommsen *et al.*, 1994; Day and Kiriatzi, 1999; Demirci *et al.*, 2004; Riederer, 2004; Josephs, 2005; Alden *et al.*, 2006; Stoltman, 2006; Abbott *et al.*, 2008; Mommsen and Japp, 2009; Braekmans *et al.*, 2011; Gauß and Kiriatzi, 2011). The subdiscipline which is responsible for provenance studies of ceramic artifacts is termed geoarcheology. The field of geoarcheology has evolved into a scientific discipline that utilizes a variety of elaborate analytical techniques (Brothwell and Pollard, 2001 and references therein).

Usually, a geoarcheological approach focuses on the characterization and study of ancient pottery production, distribution, and consumption rather than the importance of the raw materials used. Chemical analysis by itself is widely accepted as being adequate for provenancing pottery articles (*e.g.* Mommsen, 2004). However, the more sophisticated "integrated methodology" (Tite, 1999), which proposes a combination of petrographic examination and chemical analysis of ceramic sherds with conventional archeological methods, has also been considered. The latter approach suggests determination of the ceramic production center, investigation of the regional geology where the pottery originated, and collection of representative raw materials (Tite, 1999). Although the aforementioned studies assist in reconstructing the technology used in pottery production and in understanding the social relationships and changes in prehistoric and historic periods, provenancing of raw materials used to fabricate the ceramics is based mainly on petrographic observations and to a lesser degree on grain-size analysis of quartz temper or analysis of heavy minerals present in the sherds. In this sense they are 'end-product oriented' rather than 'raw-material oriented'. This difference in approach affects the interpretation of technological changes and social implications (Tite, 1999 and references therein).

Provenance studies in geoarcheology are based on the assumption that the chemical and physical characteristics of ceramics must reflect the physical and chemical characteristics of the clay from which they were fabricated. It is important, therefore, to establish safe criteria that will enable direct comparison of the possible raw materials with ceramics data. In most cases thus far, these criteria are geochemical (Dias and Prudencio, 2008; Ma *et al.*, 2012) or a combination of geochemical and petrographic criteria (Gauß and Kiriatzi, 2011). Reliable criteria for provenance of raw materials used in the fabrication of ceramics have not been proposed to date, however. Several of the existing approaches, integrated or not, focus on the provenance of the ceramic articles rather than on the raw materials employed (Tite, 1999 and references therein; Mommsen, 2004; Li *et al.*, 2005; Braekmans *et al.*, 2011; Dias *et al.*, 2013, among many others). In studies where provenance analysis is considered, either the results which used *REE* are qualitative (Ma *et al.*, 2012) or the geochemical differences between the ceramics and the raw materials are simply attributed to the inhomogeneity of the latter (Prudencio *et al.*, 2006), or they do not refer directly to ancient ceramics but record geochemical differences between sediments (Marques *et al.*, 2010) and/or their fired products (Trindade *et al.*, 2010) and consider their possible use as raw materials in ancient ceramics. The proposed integrated model, which is valid for clay raw materials used in the production of ceramics, comprises five criteria, which all should be considered, namely: geographic/geologic, petrographic, mineralogical, mineral-chemical, and geochemical criteria. These criteria are complementary and interrelated.

The geographic/geologic criterion requires that the raw material should have been close to the main ceramics production center. From an archeological perspective the ancient production sites should have been built close to the clay sources so that the craftsmen had access to a constant supply of raw materials in order to make proper blends if necessary. Ceramic articles were used in everyday life. Hence, continual production was necessary. In contrast, raw materials that played different roles, such as precious metals or metals used for production of weapons (*i.e.* 'strategic' raw materials), could be transported from greater distances or imported. On Aegina, the main production and exporting center for ceramics was the archeological site of Kolonna (Figure 1b). Therefore, the source of the clay raw materials is expected to have been in the vicinity of the site. Both the Pliocene volcanic clay and the marls crop out within a few km of Kolonna, fulfilling the geographic criterion. Moreover, the location of the Pliocene volcanic clay provides reliable answers to the questions about the thickness of the volcanic clay (Gauß and Kiriatzi, 2011): the mechanism of eruption allowed transportation and deposition of the volcanic ejecta mainly toward the north in seawater, leading to 0.4−4 m-thick pyroclastic deposits, which would sustain the production of ceramics for 2000 years. The thickness of these pyroclastic deposits is not extensive in the E-SE part of the island, either due to the mechanism of the eruption or/and due to the depositional environment in that area, which was terrestrial. This is indicated by the lack of Poros marly limestones in the Portes area (Figure 1). Finally, the presence of Poros marly limestone is associated with the formation of pedogenic calcite nodules and palygorskite. The existence of pedogenic calcite is ubiquitous in the Aeginetan ceramics (Gauß and Kiriatzi, 2011).

The textural variations, which were mentioned in the results, and by default, the chemical variations among coarse- and fine-grained Aeginetan Ware sherds, may reflect differences in the particle size and the transport mechanisms of the original volcanic ash (Christidis *et al.* in press). Thus, coarser materials were deposited closer to the volcanic center of Skotini and finer were transported further away from the volcanic vent. This is important geographic evidence for the archeological community. The sorting of the volcanic material during transport may explain the geochemical differences among the volcanic clay samples (*e.g.* sample A83). The presumed archeological theory (Lindblom, 2001 and references therein) has been that the Aeginetans placed a coarse 'temper' (presumably a local andesite) in a fine-grained clay (presumably a marl, adjoining the settlement of Kolonna). An alternative scenario for mixture of two sources has also been proposed at least for some ceramic groups (Gauß and Kiriatzi, 2011). The possibility of an alternative source or that the 'temper' might have been a natural component of the clay deposit has not been considered. The existence of reference materials renders the issue less clear. If this was not a mixture with a generic marl, the use of a clay source other than that presumed needs to be suggested. It is completely different social behavior for a group of potters to (1) intentionally add a temper to a pre-existing clay, than (2) to look for a natural clay deposit that fulfills their functions as potters and the demands of a changing market and environment.

The petrographic criterion can assist in distinguishing potential source materials according to their fabric, as volcanic, sedimentary, or metamorphic (Tite, 1999; Braekmans *et al.*, 2011; Gauß and Kiriatzi, 2011) (Figure 4a,b). Betancourt and Myer (in Zerner, 1986) reported the original petrographic sample for "Aeginetan Ware" and named the fabric the "Volcanic Ash Group", but they did not differentiate between coarse and fine ceramic samples. Their sherd samples of both the coarse- and fine-grained 'Aeginetan Ware' had a comparable volcanic matrix or groundmass and attested to a single source. Petrographic analysis in this study confirms that fine- and coarse-fabric groups of Aeginetan Ware consist of a fine-grained volcanic ash-like matrix that contains dispersed fragments of various igneous minerals (*e.g.* quartz, feldspar, and hornblende), as well as fragments of volcanic rock. However, use of the petrographic criterion as a single test of evidence for provenance has two main shortcomings. First, it does not prove that the raw material originated from Aegina. Textures similar to those of the Aeginetan rocks are observed in volcanic rocks from other volcanic centers of the SAVA, such as Methana and Poros which are close to Aegina. Second, if a volcanic rock was used as a non-plastic temper in clayey or marly sediment, as is often the case in ancient ceramics, then it might be difficult to distinguish the nature of the raw material, as was also suggested for the fine-grained Aeginetan Ware (*e.g.* Gauß and Kiriatzi, 2011). Hence the petrographic criterion should be used cautiously and always in combination with other criteria.

Mineralogical and mineral-chemistry criteria are important tools for provenance analysis because they can assist in identification of the clay source and allow prediction of the high-temperature phases after firing. Microanalytical data of amphiboles in ceramic sherds from Aegina have been used to suggest a single source for Aeginetan pottery and to propose the establishment of trade routes in the area (Dorais and Shriner, 2002a, 2002b; Dorais *et al.*, 2004). The main difficulty in applying this criterion is the selection of suitable tracer minerals and the necessity for a large database with analytical data from the broader area for this mineral, in order to provide a reliable compositional range typical for the particular source rocks. For Aegina, amphiboles have proven to be reliable tracers, because they are chemically distinct from their counterparts in other volcanic centers of the SAVA (Dietrich *et al.*, 1988; Dorais and Shriner, 2002a; Brophy *et al.*, in press; http://www.indiana.edu/~sava/). The sherds contain hornblende with Na_2O and K_2O contents which are identical to their counterparts in the Aeginetan dacites and the Pliocene volcanic clay. Nevertheless, there is a partial overlap with the composition of the amphiboles from the volcanoes of Methana and Milos (Brophy *et al.*, in press; http://www.indiana.edu/~sava/), suggesting that the use of mineral chemistry alone as a provenance tool sometimes may not be conclusive. Feldspars can also be used as mineralogical tracers in the present study. The presence of different feldspars in the two sediment types (andesine and K-feldspar in the Pliocene clay *vs.* albite in the Pliocene marl) and the persistence of feldspar in fired products formed under low firing conditions (Figure 13) provide a significant mineral-chemical criterion for provenancing in Aegina. However, such a criterion would not be useful in other areas if the different sediments contain similar types of feldspars.

The geochemical criterion is relatively reliable and has been used and tested for stratigraphic correlation purposes (Huff *et al.*, 1991). Moreover, it has been used by Hein *et al.* (2004) to assign a clay source to the group-A sherds of Mommsen *et al.* (2001). The present authors consider that the geochemical criterion is a strong component of the model because it relies on the information provided by a large number of chemical elements, not on a single parameter. However, it must be used cautiously when there is indication of addition of tempers or mixing of raw materials from different sources. There are two ways to use the geochemical criterion: either (1) by direct comparison of the chemical composition of the materials or rocks in question using binary or ternary plots (Figures 7–11); or (2) by applying statistical methods, including multivariate

methods. The former approach is straightforward and may provide useful information if mixing of materials has not taken place, the number of rock units examined is limited, and the units have distinct chemical compositions. In both approaches the geochemical criterion must be used after correction for dilution by carbonates and quartz temper. In the present study the elemental concentrations were normalized on a volatile-free basis. The use of concentration ratios instead of simple element concentrations might assist in this regard (Dias and Prudencio, 2008), provided that suitable ratios with geochemical/geologic significance are selected (McLennan and Taylor, 1991; McLennan *et al.*, 1993). The statistical methods should be applied as a means of verification of the conventional geochemical approach (Figures 13–14). The selection of suitable chemical elements as tracers can assist in the recognition of the correct source. In the case of Aegina, the Pliocene volcanic clay is geochemically distinct from the Pliocene marls in terms of both major and trace elements, including the *REE* (Figures 7–11). In the present study, the geochemical criterion was conclusive for the source of the Aeginetan sherds.

Application of statistical methods may assist in a better separation of the possible clay source rocks, especially if several rock types are present (Figure 14). Alternatively, they may compare the average elemental concentrations between different populations (Figure 13, Hein *et al.*, 2004). Nevertheless, as statistical approaches are not always conclusive (*e.g.* Hein *et al.*, 2004), they may provide misleading results if analysis is not associated with detailed mineralogical study and geologic fieldwork, which will allow recognition of possible alternative clay sources. It may be useful to apply conventional binary or ternary geochemical plots for a rough estimation before applying statistical tools.

The aforementioned discussion clearly demonstrates that there is not a single criterion that may yield reliable results in ceramic provenance studies aiming at determination of the clay sources. Our approach is based on the combination of different criteria that complement each other and are interrelated.

CONCLUSIONS

A late Lower Pliocene volcanic clay unit, which was originally an ash deposit, was identified on Aegina Island, Greece. That volcanic unit has been differentiated from the underlying Lower Pliocene marl previously considered as the main source for Aeginetan Ware (Hein *et al.*, 2004), and has been shown to be the main raw material for Aeginetan Ware. In addition, an integrated approach that may contribute to reliable ceramic provenancing and processing analysis was proposed. The approach uses geographic, petrographic, mineralogical, mineral-chemical and geochemical criteria. All five criteria should be used together in any successful provenance study, because each individual criterion, on its own, could lead to ambiguous conclusions. This approach showed that it is not necessary to assume admixture of different sources for the fabrication of fine-grained Aeginetan ceramics, suggesting that the role of Pliocene marls was probably limited, contrary to previous studies. Thus, the different textures in Aeginetan ceramics may well be explained either by selection of different sections of the same horizon having different particle-size distribution for fabrication of different ceramic styles or/and by use of approaches such as levigation to remove the coarse-grained fractions. The next step is to evaluate effectively the source clays to provide an estimate of the firing temperature of the ancient ceramics – this will be the subject of a future publication.

ACKNOWLEDGMENTS

The authors thank Drs Florens Felten and Lydia Berger for their continued support throughout various aspects of the South Aegean Volcanic Arc (SAVA) research project. In addition to their assistance with archeological sampling and permits, the authors are particularly grateful to them for their willingness to try new approaches. The Institute of Geology and Mineral Exploration (IGME) is also acknowledged for extensive support throughout the raw material-sampling process. Indiana University's Department of Geological Sciences, Bloomington, Indiana, USA and the American School of Classical Studies at Athens offered additional support for this project. Mention must be made of Dr Kenneth Finger (University of California) and his invaluable paleontological analyses. Funding for this and other related projects was supplied by a diverse group of interested agencies: Indiana University's Schrader Archeological Endowment Fund, National Endowment for the Humanities (NEH) 2004–2007 Collaborative Research Grant, Institute of Aegean Prehistory (INSTAP) Renewable Research Grant (2003–2008), and the Cotton Foundation (United Kingdom). The text benefited from constructive reviews by two anonymous reviewers.

REFERENCES

Abbott, D., Lack, A., and Moore, G. (2008) Chemical assays of temper and clay: modeling pottery production and exchange in the uplands north of the Phoenix Basin, Arizona, USA. *Archeometry*, **50**, 48–66.

Alden, J., Minc, L., and Lynch, T. (2006) Identifying the sources of Inka period ceramics from northern Chile: results of a neutron activation study. *Journal of Archaeological Science*, **33**, 575–594.

Beier, T. and Mommsen, H. (1994) Modified Mahalanobis filters for grouping pottery by chemical composition. *Archeometry*, **36**, 287–306.

Benda, L., Jonkers, H.A., Meulenkamp, J.E., and Steffens, P. (1979) Biostratigraphic correlations in the Eastern Mediterranean Neogene. *Newsletters on Stratigraphy*, **8**, 61–69.

Braekmans, D., Degryse, P., Poblome, J., Neyta, B., Vyncke, K., and Waelkens, M. (2011) Understanding ceramic variability: an archaeometrical interpretation of the Classical and Hellenistic ceramics at Düzen Tepe and Sagalassos (southwest Turkey). *Journal of Archaeological Science*, **38**, 2101–2115.

Brophy, J., Christidis, G., Murray, H., and Shriner, C. (in press) Aeginetan Ware (AW) provenancing report. In: *Die Frühhelladisch II – Keramik von Ägina Kolonna* (L. Berger, editor). Ägina-Kolonna, Forschungen und Ergebnisse, Austrian Academy of Science, Vienna.

Brothwell, D.R. and Pollard, A.M. (editors) (2001) *Handbook of Archaeological Sciences*. John Wiley and Sons, Ltd., Chichester, UK, 762 pp.

Buxeda i Garrigos, J. (1999) Alteration and contamination of archeological ceramics: the perturbation problem. *Journal of Archaeological Science*, **26**, 295–313.

Christidis, G.E. (2001) Geochemical correlation of bentonites from Milos Island, Aegean, Greece. *Clay Minerals*, **36**, 295–306.

Christidis, G., Murray, H.H., Shriner, C.M., and Brophy. J. (in press) Source clay provenancing report for Aeginetan ware: Ceramic characterization to ceramic provenancing. In: *Die Frühhelladisch II – Keramik von Ägina Kolonna* (L. Berger). Ägina-Kolonna, Forschungen und Ergebnisse, Austrian Academy of Science, Vienna.

Collinson, J.D. and Thompson, D.B. (1988) *Sedimentary Structures*, 2nd edition. Unwin Hyman, London.

Cullers, R., Chaudhuri, S., Kilbane, N., and Koch, R. (1979) Rare-earths in size fractions and sedimentary rocks of Pennsylvanian-Permian age from the mid-continent of the U.S.A. *Geochimica et Cosmochimica Acta*, **43**, 1285–1301.

Cultrone, G., Rodriguez-Navarro, C., Sebastian, E., Cazalla, O., and De La Torre, M.J. (2001) Carbonate and silicate phase reactions during ceramic firing. *European Journal of Mineralogy*, **13**, 621–634.

Day, P.M. and Kiriatzi, E. (1999) Group therapy in Crete: A comparison between analyses by NAA and thin section petrography of Early Minoan pottery. *Journal of Archaeological Science*, **26**, 1025–1036.

Demirci, S., Caner-Saltik, E., Türkmenoglu, A., Özçilingir-Akgün, S., and Bakirer, O. (2004) Raw material characteristics and technological properties of some medieval glazed ceramics and tiles in Anatolia. *Key Engineering Material*, **264–268**, 2395–2398.

Dias, M.I. and Prudêncio, M.I. (2008) On the importance of using scandium to normalize geochemical data preceding multivariate analyses applied to archaeometric pottery studies. *Microchemical Journal*, **88**, 136–141.

Dias, M.I., Prudêncio, M.I., Pinto De Matos, M.A., and Luisa Rodrigues, A. (2013) Tracing the origin of blue and white Chinese Porcelain ordered for the Portuguese market during the Ming dynasty using INAA. *Journal of Archaeological Science*, **40**, 3046–3057.

Dietrich, V.J., Mercolli, I., and Oberhänsli, R. (1988) Dazite, High-Alumina-Basalte und Andesite als Produkte Amphibol dominierter Differentiation (Ägina und Methana, Ägäischer Inselbogen). *Schweizerische Mineralogische & Petrographische Mitteilungen*, **68**, 21–39.

Dietrich, V., Gaitanakis, P., Mercolli, I., and Oberhansli, R. (1991) *Geological map of Greece, Aegina Island*, *1:25,000*. Stiftung Vulkaninstitut Immanuel Friedlaender, Zurich.

Dietz, S. (1991) *The Argolid at the Transition to the Mycenaean Age. Studies in the Chronology and Cultural Development in the Shaft Grave Period.* The National Museum of Denmark, Copenhagen, 336 pp.

Dombrowski, T. (1993) Theories of origin for the Georgia kaolins: a review. Pp.75–97 in: *Kaolin Genesis and Utilization* (H.H. Murray, W.M. Bundy, and C.C. Harvey, editors). The Clay Minerals Society, Special Publications, **1**, The Clay Minerals Society, Boulder, Colorado, USA.

Dorais, M.J. and Shriner, C.M. (2002a) A comparative electron microprobe study of "Aeginetan" wares with potential raw material sources from Aegina, Methana, and Poros, Greece. *Geoarchaeology: An International Journal*, **17**, 555–577.

Dorais, M.J. and Shriner, C.M. (2002b) An electron microprobe study of P645/T390: Evidence for an Early Helladic III Lerna–Aegina connection. *Geoarchaeology: An International Journal*, **17**, 755–778.

Dorais, M.J., Lindblom, M., and Shriner, C.M. (2004) Evidence for a single clay/temper source for the manufacture of Middle and Late Helladic Aeginetan pottery from Asine, Greece. *Geoarcheology*: *An International Journal*, **19**, 657–684.

Douglass, A.A. and Schaller, D.M. (1993) Sourcing Little Colorado White Ware: a regional approach to the compositional analysis of prehistoric ceramics. *Geoarchaeology: An International Journal*, **8**, 177–201.

Faupl, P., Pavlopoulos, A., and Migiros, G. (1998) On the provenance of flysch deposits in the External Hellenides of mainland Greece: results from heavy mineral studies. *Geological Magazine*, **135**, 421–442.

Forsén, J. (1996) Prehistoric Asea revisited. *Opuscula Atheniensia*, **XXI: 4**, 41–72.

Freestone, I. and Gaimster, D. (editors) (1997) *Pottery in the Making: Ceramic Traditions*. Smithsonian Institution Press, Washington, DC, 240 pp.

Gauß, W. and Kiriatzi, E. (2011) *Pottery Production and Supply at Bronze Age Kolonna, Aegina: an integrated archaeological and scientific study of a ceramic landscape.* Ägina-Kolonna. Forschungen und Ergebnisse **5**. Austrian Academy of Science, Vienna, 527 pp.

Gonzalez-Lopez, J.M., Bauluz, B., Yuste, A., Mayayo, M.J., and Fernandez-Nieto, C. (2005) Mineralogical and trace element composition of clay-sized fractions from Albian siliciclastic rocks (Oliete Basin, NE Spain). *Clay Minerals*, **40**, 565–580.

Hein, A., Mommsen, H., and Zender, G. (2004) Pliocene clays from Aegina (Greece): Reference material for chemical provenance studies on Bronze Age pottery from the Island. *Geoarcheology: An International Journal*, **19**, 553–564.

Huff, W.D., Anderson, T.B., Rundle, C.C., and Odin, G.S. (1991) Chemostratigraphy, K-Ar ages and illitization of Silurian K-bentonites from the Central Belt of the Southern Uplands-Down-Longford terrane, British Isles. *Journal of the Geological Society*, **148**, 861–868.

Jones, R.E. (1986) *Greek and Cypriot Pottery: A Review of Scientific Studies*. Fitch Laboratory Occasional Paper, **1**. The British School at Athens, 938 pp.

Jones, R.E. (1993) Pottery as evidence for trade and colonization in the Aegean Bronze Age: The contribution of scientific techniques. Pp. 11–17 in: *Wace and Blegen: Pottery as Evidence for Trade in the Aegean Bronze Age, 1939–1989* (C. Zerner, P. Zerner, and J. Winder, editors). Gieben, Amsterdam.

Josephs, R. (2005) A petrographic analysis of extended Middle Missouri ceramics from North Dakota. *Plains Anthropologist*, **50**, 111–119.

Kaner, S. (2003) The oldest pottery in the world. *Current World Archeology*, **1**, 44–49.

Kingery, W.D. (1982) Plausible inferences from ceramic artifacts. Pp. 37–45 in: *Archaeological Ceramics* (J.S. Olin, editor). Smithsonian Institution Press, Boston, Massachusetts, USA.

Li, B.-P., Greig, A., Zhao, J.-X., Collerson, K.D., Quan, K.-S., Meng, Y.-H., and Ma, Z.L. (2005) ICP-MS trace element analysis of Song dynasty porcelains from Ding, Jiexiu and Guantai kilns, north China. *Journal of Archaeological Science*, **32**, 251 –259.

Lindblom, M. (2001) *Marks and makers: Appearance, distribution and function of Middle and Late Helladic manufacturers' marks on Aeginetan pottery*. Studies in Mediterranean Archeology, **78**. Paul Aström Förlag, Jonsered, Sweden, 145 pp.

Ma, H., Zhu, J., Henderson, J., and Li, N. (2012) Provenance of Zhangzhou export blue-and-white and its clay source. *Journal of Archaeological Science*, **39**, 1218–1226.

Marques, R., Jorge, A., Franco, D., Dias, M.I., and Prudêncio, M.I. (2010) Clay resources in the Nelas region (Beira Alta), Portugal. A contribution to the characterization of potential raw materials for prehistoric ceramic production. *Clay Minerals*, **45**, 353–370.

Marinoni, L., Setti, M., Salvi, C., and Lopez-Galindo, A. (2008) Clay minerals in Late Quaternary sediments from the south Chilean margin as indicators of provenance and paleoclimate. *Clay Minerals*, **43**, 235–253.

McLennan, S.M. and Taylor, S.R. (1991) Sedimentary rocks and crustal evolution; Tectonic setting and secular trends. *Journal of Geology*, **99**, 1–21.

McLennan, S.M., Hemming, S., McDaniel, D.K., and Hanson, G.K. (1993) Geochemical approaches to sedimentation, provenance and tectonics. Pp. 21–40 in: *Processes Controlling the Composition of Clastic Sediments* (M.J. Johnson and A. Basu, editors). GSA Special Paper, **284**, Geological Society of America, Boulder, Colorado, USA.

Middleton, A.P. and Freestone, I.C. (editors) (1991) *Recent Developments in Ceramic Petrology*. British Museum Occasional Paper, **81**. British Museum, London, vii + 410 pp.

Mommsen, H. (2004) Provenancing of Pottery – the need for an integrated approach? *Archeometry*, **46**, 267–271.

Mommsen, H. and Japp, S. (2009) Neutronenaktivierungsanalyse von 161 Scherben aus Pergamon und Fundorten der Region. *Istanbuler Mitteilungen*, **59**, 269 – 282

Mommsen, H., Beier, T., Heimermann, D., Hein, A., Ittameier, D., and Podzuweit, Ch. (1994) Neutron activation analysis of selected sherds from Prophitis Ilias (Argolid, Greece): a closed Late Helladic II settlement context. *Journal of Archaeological Science*, **21**, 163–171.

Mommsen, H., Gauss, W., Hiller, S., Ittameier, D., and Maran, J. (2001) Charakterisierung bronzezeitlicher Keramik von Ägina durch Neutronaktivierungsanalyse. Pp. 79–96 in: *Archäologisches Zellwerk, Beiträge zur Kulturgeschichte in Europa und Asien* (E. Pohl, U. Recker, and C. Theune, editors). Rahden, Westfalen, Germany.

Morris, A. (2000) Magnetic fabric and palaeomagnetic analyses of the Plio-Quaternary calc-alkaline series of Aegina Island, south Aegean volcanic arc, Greece. *Earth and Planetary Science Letters*, **176**, 91–105.

Müller, P., Kreutzer, H., Lenz, H., and Harre, W. (1979) Radiometric dating of two extrusives from a Lower Pliocene marine section on Aegina Island, Greece. *Newsletters on Stratigraphy*, **8**, 70–78.

Nordquist, G.C. (1987) *A Middle Helladic Village. Asine in the Argolid.* Boreas, **16**. Uppsala University Press, Uppsala, Sweden, 195 pp.

Pe-Piper, G., Piper, D.J.W., and Reynolds, P.H. (1983) Paleomagnetic stratigraphy and radiometric dating of the Pliocene volcanic rocks of Aegina, Greece. *Bulletin Volcanologique*, **46**, 1–7.

Peters, T. and Iberg, R. (1978) Mineralogical changes during firing of calcium-rich clays. *Ceramic Bulletin*, **57**, 503–509.

Prudêncio, M.I., Oliveira, F., Dias, M.I., Sequeira Braga, M.A., Delgado, M., and Martins, M. (2006) Raw materials identification used for the manufacture of Roman "Bracarense" ceramics from NW Iberian Peninsula. *Clays and Clay Minerals*, **54**, 639–651.

Pullen, D.J. (2000) The prehistoric remains of the Acropolis at Halieis: A final report. *Hesperia*, **69**, 133–187.

Pullen, D.J. (2011) *Early Bronze Age Village on Tsoungiza Hill (Nemea Valley Archaeological Project I)*. American School of Classical Studies at Athens, Princeton, New Jersey, USA.

Rathossi, C., Tsolis-Katagas, P., and Katagas, C. (2004) Technology and composition of Roman pottery in northwestern Peloponnese, Greece. *Applied Clay Science*, **24**, 313–326.

Riederer, J. (2004) Thin section microscopy applied to the study of archaeological ceramics. *Hyperfine Interactions*, **154**, 143–158.

Rotroff, S. (2006) *Hellenistic Pottery: the Plain Wares*. The Athenian Agora, v. 33. American School of Classical Studies at Athens, Princeton, New Jersey, USA, 438 pp.

Ruby, B.J. and Shriner, C.M. (2005) Ceramic vessel compositions and styles as evidence of the local and non-local social affiliations of ritual participants at the Mann Site, Indiana. Pp. 553–572 in: *Gathering Hopewell: Society, Ritual and Ritual Interaction* (C. Carr and D.T. Case, editors). Plenum, New York.

Rutter, J.B. (1989) A ceramic definition of Late Helladic I from Tsoungiza. *Hydra*, **6**, 1–19.

Rutter, J.B. (1990) Pottery groups from Tsoungiza of the end of the Middle Bronze Age. *Hesperia*, **59**, 375–458.

Setti, M., Marinoni, L., and Lopez-Galindo, A. (2004) Mineralogical and geochemical characteristics (major, minor, trace elements and REE) of detrital and authigenic clay minerals in a Cenozoic sequence from Ross Sea, Antarctica. *Clay Minerals*, **39**, 405–421.

Shriner, C.M. (1999) Ceramic Technology at Lerna, Greece in the Third Millennium B.C.: Economic and Social Implications. PhD dissertation, Indiana University, Bloomington, Indiana, USA, 261 pp.

Shriner, C. and Dorais, M.J. (1999) A comparative electron microprobe study of Lerna III and IV ceramics and local clay-rich sediments. *Archeometry*, **41**, 25–49.

Shriner, C.M., Christidis, G., Brophy, J., Finger, K., and Murray, H. (2007) Clay mineralogical studies of the source material for Aeginetan Ware, Aegina, Greece. P. 150 in: *The Clay Minerals Society, 44th Annual Meeting Program and Abstracts, June 2–7, 2007.* Santa Fe, New Mexico.

Shriner, C., Christidis, G., and Murray, H.H. (in press) Ceramic technology report for Aeginetan ware: Unraveling archaeological problems using provenance and processing. In: *Die Frühhelladisch II – Keramik von Ägina Kolonna* (L. Berger). Ägina-Kolonna, Forschungen und Ergebnisse, Austrian Academy of Science, Vienna.

Slack, J.F. and Stevens, B.P.J. (1994) Clastic metasediments of the Early Proterozoic Broken Hill Group, New South Wales, Australia: Geochemistry, provenance and metallogenic significance. *Geochimica et Cosmochimica Acta*, 58, 3633–3652.

Stamatakis, M.G. and Magganas, A.C. (1989) Thermally induced silica transformation in Pliocene diatomaceous layers from Aegina Island, Greece. Pp. 141–150 in: *Siliceous Deposits of the Tethys and Pacific Regions* (J.R. Hein and J. Obradovic, editors). Springer Verlag, New York.

Stoltman, J.B. (2006) Petrographic analysis. Pp. 405–407 in: *Hellenistic Pottery: the Plain Wares* (S. Rotroff). American School of Classical Studies at Athens, Princeton, New Jersey, USA.

Tite, M.S. (1999) Pottery production, distribution, and consumption – the contribution of the physical sciences. *Journal of Archeological Method and Theory*, **6**, 181–233.

Traoré, K., Kabré, T.S., and Blanchart, P. (2003) Gehlenite and anorthite crystallization from kaolinite and calcite mix. *Ceramics International*, **29**, 377–383.

Trindade, M.J., Dias, M.I., Coroado, J., and Rocha, F. (2010) Firing tests on clay-rich raw materials from the Algarve Basin (Southern Portugal): study of mineral transformations with temperature. *Clays and Clay Minerals*, **58**, 188–204.

Tsoli-Katagas, P. (1977) Geochemistry of clay formations from the island of Aegina. *Bulletin of the Geological Society of Greece*, **13**, 71–96.

Velde, B. and Druc, I.C. (1999) *Archaeological Ceramic Materials: Origin and Utilization*. Springer, Berlin, 299 pp.

Whitbread, I. (2001) Ceramic petrology, clay geochemistry and ceramic production – from technology to the mind of the potter. Pp. 449–459 in: *Handbook of Archaeological Sciences* (D.R. Brothwell and A.M. Pollard, editors). John Wiley and Sons, Ltd., Chichester, UK.

Whitbread, I.K., Kiriatzi, E., and Tartaron, T. (2002) Middle Bronze Age ceramic production in central and southern mainland Greece: the design of a regional petrographic study. Pp. 121– 128 in: *Modern Trends in Scientific Studies on Ancient Ceramics.* BAR International Series, **1011**, John and Erica Hedges Ltd., Oxford, UK.

Wronkiewitz, D.J. and Condie, K.C. (1990) Geochemistry and mineralogy of sediments from the Ventersdorp and Transvaal Supergroups, South Africa: Cratonic evolution during the early Proterozoic. *Geochimica et Cosmochimica Acta*, **54**, 343–354.

Zerner, C.W. (1986) Middle Helladic and Late Helladic I pottery from Lerna. *Hydra*, **2**, 58–74.

Zerner, C.W. (1993) New perspectives on trade in the Middle and Early Late Helladic Periods on the mainland. Pp. 39–56 in: *Wace and Blegen: Pottery as Evidence for Trade in the Aegean Bronze Age, 1939–1989* (C.W. Zerner, P. Zerner, and J. Winder, editors). Gieben, Amsterdam.

(*Received 11 April 2014; revised 14 December 2014; Ms. 866; AE: E. Garcia-Romero*)

Clays and Clay Minerals, Vol. 62, No. 6, 470–476, 2014.

The 2013 Marilyn and Sturges W. Bailey Distinguished Member Award was presented to Stephen Guggenheim, Department of Earth and Environmental Sciences, University of Illinois at Chicago, Chicago, Illinois, at the 50th Anniversary Annual Meeting of The Clay Minerals Society, University of Illinois at Urbana-Champaign on October 8, 2013. The following article is based on the lecture presented at that time by S. Guggenheim.

AN INTEGRATED EXPERIMENTAL SYSTEM FOR SOLID-GAS-LIQUID ENVIRONMENTAL CELLS

STEPHEN GUGGENHEIM* AND A. F. KOSTER VAN GROOS

Department of Earth and Environmental Sciences, University of Illinois at Chicago, 845 W. Taylor St., Chicago, Illinois, USA

Abstract—The geochemistry of minerals in intermediate to deep sedimentary rocks (2−10 km depth) is not known sufficiently well to predict accurately the effect of human activities, such as carbon dioxide sequestration or fracking. To carry out real-time experiments, a high-pressure environmental chamber (HPEC) was constructed for *in situ* X-ray diffraction (XRD) studies to 1000 bars and to 200ºC. In the HPEC, a liquid, *e.g*. a brine, plus sample in suspension, is pressurized by gas, *e.g*. CH_4 or CO_2, or liquid, *e.g*. supercritical CO_2. The unique aspect of this chamber is that the sample + liquid (~2 mL) form a dynamic system, and particles can move freely in the liquid while being illuminated by the X-ray beam. Several HPECs were constructed of Ti alloy, stainless steel, or carbon-fiber polyether ketone to be resistant to corrosion under basic or acidic conditions. These HPECs are compatible with standard transmission-mode diffractometers with sealed-tube X-ray sources (Mo radiation is being used at the University of Illinois at Chicago − UIC) or with brilliant X-ray sources. In addition, to allow long-duration studies or, for example, to study the effect of micro-organisms on these mineral reactions, a large-bore (~25 mL) reaction vessel system was devised that could be examined regularly at appropriate *P/T* conditions or off-line. Calibration of the HPEC and XRD pattern processing is discussed and illustrated. The potential significance of these devices goes beyond understanding the deep sedimentary environment, because materials and reactions can be studied while using nearly any liquid as an immersion agent. As an example, experimental results are given for the d_{001} values of montmorillonite clay *vs*. temperatures to 150ºC at $P(CO_2)$ = 500 bars in a NaCl-rich brine.

Key Words—Experimental Clay Studies, Reaction Vessels, XRD.

INTRODUCTION

The mineralogy, mineral kinetics, and the interactions of minerals and fluids in intermediate to deep sedimentary rocks (2−10 km depth) are, in general, not sufficiently known to predict the effect of human activities, such as carbon dioxide sequestration or oil and gas production, including fracking. To study this environment at the appropriate natural conditions, experimental techniques are required which allow the direct observation and monitoring of mineral changes at elevated temperatures and pressures in solid-fluid-gas systems. Cells for the analysis of solids in contact with a liquid for studies at elevated temperatures and pressures have been available since the 1960s (*e.g*. Van Valkenburg, 1962; Bassett and Takahashi, 1965; Hazen and Finger, 1982). Cells developed more recently consist of potentially harmful materials (*e.g*. Be in the case of Mauron *et al*., 2011) or require complex and sophisticated high-pressure anvils, image plates, microfocus X-ray sources, *etc*. (*e.g*. Toulemonde *et al*., 2014). Most of these environmental cells are not optimized to simulate the conditions of sedimentary basins at moderate pressures (<1−2 kbar) and temperatures (<200ºC), and these cells do not allow studies that characterize the changes in the physical and chemical properties of the solid phase as well as of the coexisting liquid and gas phases. In addition to a system allowing for the direct observation and monitoring of reactants at elevated temperatures and pressures, a system is needed that also allows small amounts of sample to be removed at the pressure and temperature of the experiment for *ex situ* analysis without ending the experiment. Such an environmental cell should be easy to use for in-house experiments, including loading of samples, assembly of the cell, and repair.

Because sedimentary basins contain clay minerals that may affect porosity and permeability, expansion (layer-to-layer distances), interlayer cation and molecular composition, and interlayer structure are important parameters. These structural and chemical parameters are believed to vary rapidly with changes in temperature and pressure. Clay minerals, therefore, are expected to back-react quickly when experiments are brought to ambient conditions. Thus, clay-mineral studies require

* E-mail address of corresponding author:
xtal@uic.edu
DOI: 10.1346/CCMN.2014.0620602

an environmental cell that allows the properties of the phases to be monitored *in situ*, which commonly involves the use of an analytical tool such as X-rays or another electromagnetic radiation. These types of reactions and kinetics are rapid and require that, for example, the environmental cell can be mounted for a relatively short period of time, several hours or days, on analytical instrumentation, such as an X-ray diffractometer. Previously, Koster van Groos *et al*. (2002) described a chamber for gas–solid interactions at low temperatures (less than ambient temperature) and elevated pressures (<100 bar). This chamber utilizes reflection-mode XRD methods that are compatible with studies on rapidly evolving reactions. For example, the stability range of clay–hydrate complexes could be determined (Guggenheim and Koster van Groos, 2003; Koster van Groos and Guggenheim, 2009) by using this chamber to explore the stability of phases in the montmorillonite–methane and nontronite–methane systems.

Maintaining an environmental cell on an X-ray diffractometer to investigate physical and chemical processes over much longer durations (weeks or months) may be impractical or cumbersome. For example, in a study of carbon dioxide sequestration in deep sedimentary reservoirs, the CO_2 may be stored in the reservoir principally as interstitial gas without significant reaction or by carbonate formation through reactions of CO_2 with the mineral constituents. The latter reaction rates would be expected to be much slower than clay-mineral intercalation reactions. In such a study, a gas-pressurized reaction vessel heated in an oven may be more suitable than heating in an environmental chamber on a diffractometer, provided that samples (liquid, powder) can be routinely extracted periodically from the vessel without terminating the experiment. The extracted samples may then be examined by *ex situ* methods.

In this paper, an integrated experimental system is described. For real-time experiments, a high-pressure environmental chamber (HPEC) was constructed for use with *in situ* XRD in studies to 1000 bars and to 200ºC. In the HPEC, a liquid, *e.g*. a brine, plus sample in suspension, is pressurized by gas, *e.g*. CH_4 or CO_2, or liquid, *e.g*. supercritical CO_2. The unique aspect of this chamber is that the sample + liquid (~2 mL) form a dynamic system, and particles can move freely in the liquid while being illuminated by the X-ray beam. The dynamic aspects of the HPEC allow the study of clay minerals in fluids, even if flocculation occurs. In addition, to allow studies of long duration or the effect of micro-organisms on these mineral reactions, a large-bore (~25 mL), high-pressure reaction vessel and sampling system were devised. Experiments could then be examined regularly *via* injection at appropriate *P/T* conditions into the HPEC. The potential significance of these devices goes beyond deep sedimentary environments because materials and reactions can be studied while using nearly any liquid as an immersion agent.

EQUIPMENT

High-pressure environmental chamber (HPEC) system

The HPEC system is a closed-circuit channel that may contain a fluid (liquid, liquid-gas mixture) suspension of fine particles that is mobilized by an internal circulation pump. The fluid may be pressurized by a gas (*e.g*. CH_4) or a liquid (*e.g*. pressurized CO_2) using an external high-pressure pump. The HPEC has two high-pressure windows (Figure 1) to allow the suspension to be analyzed continuously using XRD. A transmission-mode X-ray diffractometer is used to minimize the path length of the X-ray beam to reduce absorption by the suspension. The dynamic nature of the system provides sufficient flow so that the particles can move freely while being illuminated by the X-ray beam, even if flocculation of the particles occurs. The HPEC may be heated using a series of cartridge heaters placed in appropriately spaced drill holes in the HPEC. Combined with the moving suspension, the temperature gradient in the chamber, therefore, is minimized. The system may be cooled instead by circulating a cooling fluid through these drill holes and a set of containment covers. A thermocouple, positioned within 2 mm of the sample flow near the X-ray windows, is used to measure and control temperature.

HPEC. Three different versions of the HPEC are available. A Ti alloy (6AL-4V ELI, ASTM Grade 5) HPEC is suitable for studies with neutral and acidic

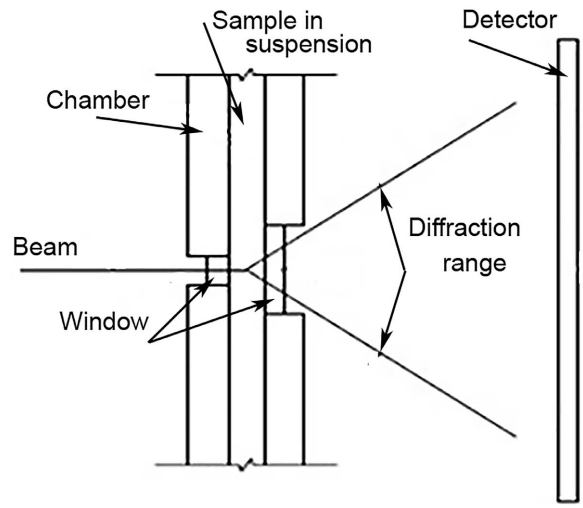

Figure 1. A schematic (not to scale) view of the diffraction component for the HPEC design. The HPEC, mounted on a Bruker 3-circle diffractometer, employs (graphite monochromatized) Mo radiation in a transmission-mode arrangement with a sample-to-detector distance of 12 cm. The single-crystal, (100) plane, vapor-deposited synthetic diamond windows are 1.0 mm thick, with the incident window of 3.0 mm diameter and the exit window of 6.0 mm diameter. The diffraction range is $2\theta = 70^{o}$. The detector in use is a CCD Bruker APEX.

fluids. This version eliminates contamination that may occur with the stainless steel version using acidic fluids. At the UIC, this version has become the 'workhorse'. A stainless steel (#316) unit performed well with various brines/seawater pressurized with Ar or He, but it exhibited significant corrosion in the presence of CO_2 + H_2O (*i.e.* carbonic acid) at elevated pressures. A third unit is made from black PEEK (carbon-fiber-reinforced polyether ether ketone) for studies with corrosive basic fluids. This unit is not being used currently.

The HPEC has two parts (Figure 2): the upper-body section (Figure 2A) contains the main portion of the closed-circuit channel. This section accommodates the diamond high-pressure window assembly, the (internal) circulation pump, and two ports, one located at the top and the other at the side of the unit. The lower-body section (Figure 2B) has a U-shaped channel that completes the closed circuit. This section has two ports. All ports are for access to the experiment as inlet or outlet ports, using appropriate valves. In addition, the ports are useful clean-outs that facilitate easy maintenance after a completed experiment. The channels in the lower and upper bodies are connected through two hollow cylinders and sealed using O-rings (Buna-N). Four assembly bolts hold the two components together.

The assembled HPEC (Figure 3) is mounted onto a dove-tail sled assembly and placed on a specially designed track on the diffractometer. The HPEC unit is aligned using adjustment screws. The (internal) circulation pump consists of an electromagnetic driven piston (sealed PEEK rod with an iron core) and a check valve

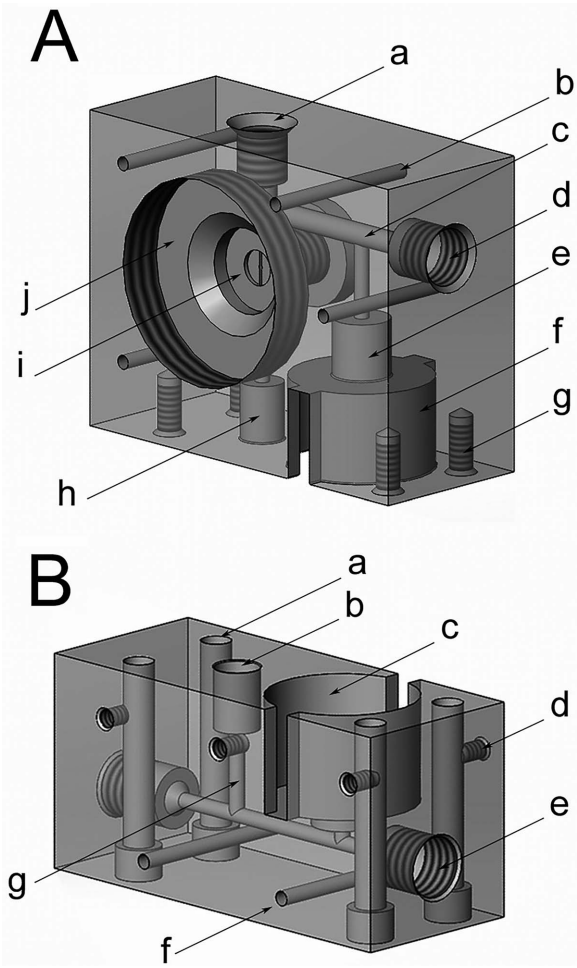

Figure 2. The 'transparent' drawing of the HPEC. Part A shows the upper section and B the lower part. Part A includes: (a) pressure port; (b) hole for insertion of cartridge heater element (or for cooling liquid); (c) portion of the closed-circuit channel; (d) access port; (e) well for connecting (large) hollow cylinder; (f) well for (electromagnetic pump) solenoid; (g) threaded assembly-bolt hole; (h) well for connecting (small) hollow cylinder; (i) well for exit window and PEEK-compression seal; and (j) well for a cone-shaped nut to compress the exit window assembly (see Figure 3). Part B includes: (a) assembly-bolt hole, see A(g); (b) well for connecting (small) hollow cylinder, see A(h); (c) well for (electromagnetic pump) solenoid, see A(f); (d) mounting hole for cooling plate, (e) access port; (f) hole for insertion of cartridge heater element (or for cooling liquid); and (g) portion of the closed-circuit channel.

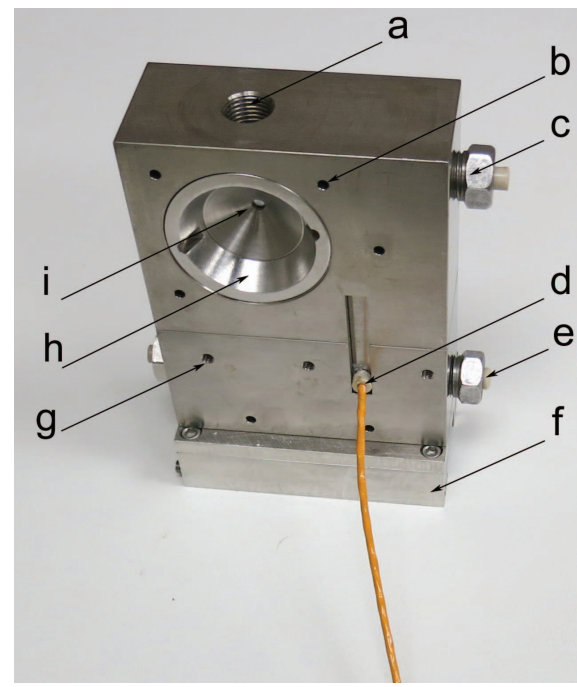

Figure 3. An assembled Ti-alloy HPEC: (a) pressure port, see Figure 2A(a); (b) hole for cartridge heater element, see 2A(b); (c) access port, see Figure 2A(d); (d) electrical lead controlling electromagnetic pump solenoid; (e) access port, see Figure 2B(e); (f) dove-tail sled assembly for placement on the diffractometer; (g) threaded mounting hole for cooling plate; (h) cone-shaped nut for exit-window assembly, see 2A(j); and (i) diamond exit window.

(PEEK tube with a ceramic sealing ball) assembly in the large-diameter cylinder (see above). The ball mechanism of the check valve reduces back flow and is self-cleaning of fine particles. The two solenoids, used for the reversing action of the electromagnetic pump drive, are placed around this cylinder. The entrance X-ray window is a synthetic diamond plate (chemical vapor deposition, 3 mm diameter, 1 mm thick), as is the exit diamond window (6 mm diameter, 1 mm thick). The exit window allows 2θ measurement to 70º (Mo radiation, 0.7107 Å). Both windows are sealed using PEEK compression seals. The suspension flows between the windows through a 1.2 mm channel, where it is illuminated by the X-ray beam. The total X-ray path in the HPEC, therefore, is 5.2 mm.

Diffractometer. The Bruker (Bruker-AXS Inc., 5465 East Cheryl Parkway, Madison, Wisconsin, USA) three-circle, single-crystal diffractometer used with the HPEC requires only a minimal modification, thereby allowing rapid conversion (~10 min, including the alignment) to and from single-crystal mode. This diffractometer is commonly available in chemistry departments, single-crystal service departments, and most synchrotron facilities. The diffractometer is equipped with an APEX area detector and *SMART* and *GADDS* software.

A Nonius (now part of Bruker) short-style, micro-capillary (MonoCap) collimator, modified with a sleeve to allow mounting on the Bruker collimator track, is used to direct and intensify the incident X-ray beam. A curved incident-beam monochromator assembly is currently available (from Bruker) and may provide greater intensity, but this monochromator has not been tested at UIC. For the conversion to accommodate the HPEC, the omega and phi circles are fixed at 0.0º, and the diffractometer base plate is replaced with a thick base plate with a cam lock to engage the HPEC position in a repeatable location. This base plate has a mounted dove-tail base track for the HPEC and a beam stop.

Control Cabinet. To operate the HPEC, all necessary equipment is housed in an adjacent control cabinet. The cabinet includes a pressure-generating unit consisting of a high-pressure pump (SC Hydraulic Engineering, 1130 Columbia St, Brea, California, USA, with 180:1 pump ratio, that was modified at UIC to pressurize gases), a manifold with a supply valve to the HPEC and an exhaust valve, and a low-pressure air-control system (filter, regulator, 0−100 psi gauge, shut-off valve). The control cabinet also contains the electronics for the (internal) circulation-pump power supply with adjustable timers, panel meters for temperature measurement/control and pressure measurement, and appropriate switches, panel lights, draws, *etc*.

High-pressure reaction vessel and sampling system

A corrosion-resistant, high-pressure system to study reactions at pressures to 1000 bars and temperatures to 200ºC was developed that allows sampling of the material at pressure. The Ti alloy (6AL- 4V ELI, ASTM Grade 5) hydrothermal pressure reaction vessel (Figure 4) is 150 mm long with a 44 mm OD and a 1.9 mm bore. The internal volume is ~36.5 mL. The entrance of the bore is cone-shaped with a width of 25 mm and an angle of 45º. The vessel is sealed using a 50 mm-wide screw cap that presses a 'mushroom'-shaped, 50 mm-long Ti tube against the pressure vessel, using a cone-shaped PEEK ring seal. Up to six vessels, with the shut-off valve attached, may be mounted in a rotating holder (1 rpm) that is located in an oven. When the vessel is charged with solid-liquid sample, several ceramic balls (*e.g.* 6 mm radius) may be added to the sample to prevent clumping of the solid grains by agitating the mixture during rotation and to remove any reaction-product coatings from grains, thus facilitating reaction.

The shut-off valve is designed to allow sampling of the vessel contents, including the solid phase, without damage to the valve. Commercially available high-pressure needle valves are not suitable for extraction of suspended particles, because these particles are likely to damage the valve needle or valve seat. In addition, these valves are not sufficiently corrosion-resistant when using CO_2-H_2O fluids, and result in Fe-contamination of the sample. To address these problems, a corrosion-resistant valve was developed.

The sample may be transferred from the vessel to a sample-holder tube (Figures 4, 5) with only a small loss (~2%) of pressure in the reaction vessel and sampling tube. The transferred sample may be used for further analysis (*e.g.* X-ray or chemical analysis), using a 1 mL

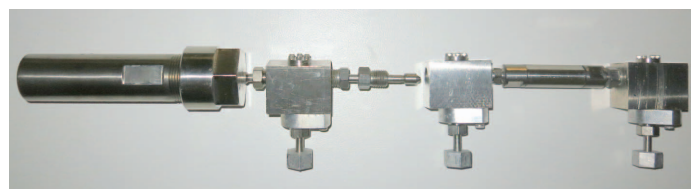

Figure 4. High-pressure Ti-alloy reaction vessel (left) and sampling system (right). This vessel is shown with a Ti-alloy shut-off valve so that suspended particulates may be extracted at pressure along with the fluid phase. The width of the valve body is 5 cm. The sampling system is shown with a hollow 1 mL sampling tube. The sampling tube is bound on either side by a shut-off valve. A connecting tube (shown) may be used to allow the transfer of material from the reaction vessel.

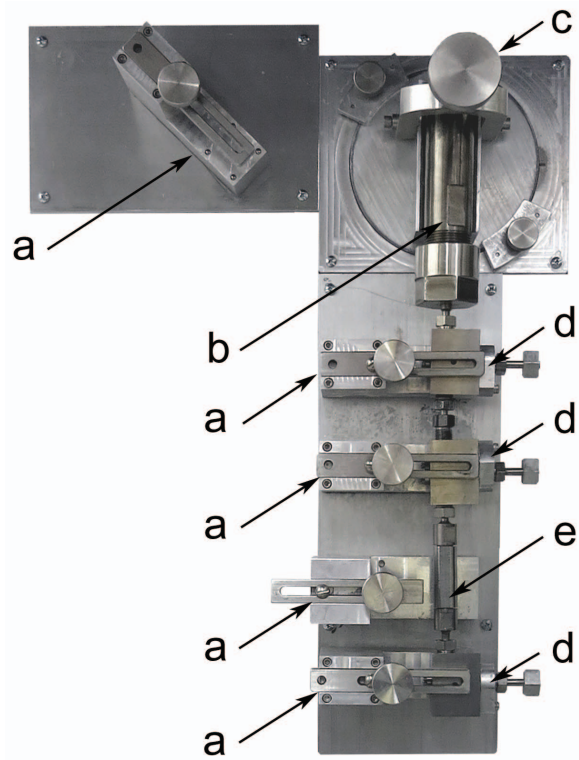

Figure 5. Wall-mounted holder assembly for pressurizing the reaction vessel or for the transfer of sample from a reaction vessel to a sampling tube. Parts of the wall-mounted holder assembly are: (a) clamp, (b) reaction vessel, (c) clamp for reaction vessel, (d) shut-off valve, and (e) sampling tube. The exchange of sample is accomplished in the vertical position so that the sample suspension is located at the bottom of the reaction vessel. The holder assembly may also be used to pressurize the reaction vessel, but pressurization requires the reaction vessel shut-off valve to be higher than the horizontal to avoid fluid from entering the pressure-intensifier assembly (not shown). For this application, the reaction vessel is rotated (note circular portion at the top of the assembly) so that the shut-off valve is positioned at clamp (a) on the far left of the figure. One clamp not in use adjacent to the hollow tube of the sampling system is present to accommodate the HPEC so that material from the reaction vessel may be injected directly into the HPEC.

size sampling tube or loaded into the HPEC (2.5 mL size) to allow the study of non-quenchable products. During sample transfer, neither the temperature of the reaction vessel nor the transfer sample-holder tube is maintained at the run temperature. The mass of each, however, is significant and temperature-loss can be minimized by a rapid transfer. Sample exchange is facilitated by a wall-mounted holder assembly (Figure 5). Because the sampling tube can be used to remove portions of the products sequentially, the rate of reactions may be monitored without having to re-start the experiment from the beginning. The reaction vessel can also be used as an incubation chamber for micro-organisms, which allows the study of the effect of organisms on mineral reactions.

CALIBRATION AND PATTERN PROCESSING

HPEC calibration

The HPEC pressure is measured using an inline pressure transducer. The temperatures are measured using a sheathed K-type thermocouple that is located in a well within 2 mm of the irradiated sample. As the HPEC is thermally conductive and the sample fluid is circulating relatively rapidly, the measured temperatures are assumed to be uniform throughout the chamber.

Pattern processing

Pattern calibration of the APEX detector position with respect to the sample (HPEC) is required. Three parameters define the detector position: *dist* is the (refined) distance between the HPEC (window-to-window) center and the detector window (in mm), *x(center)* is the (refined) horizontal position of the detector window (in pixels), and *y(center)* is the (refined) vertical position of the detector window (in pixels). To obtain a broad range of 2θ values, *e.g.* using Mo radiation, the detector is placed at three 2θ positions, at 0, 20, and 35º, and the detector distance is set to near 120 mm. A single set of *x(center)*, *y(center)*, and *dist* values is obtained by taking the average from the three 2θ positions. If a single detector position is of greater importance, the 2θ value is fixed and average values are not used. For example, because the d_{001} value of smectite is of greatest interest in clay mineralogy, the *x(center)*, *y(center)* and *dist* values at only one detector position (2θ = 0º, near 120 mm) are obtained by using chlorite [d_{001} = 14.2 Å] for calibration. Where all three 2θ detector positions are useful, LaB_6 powder is used for calibration and the respective *x(center)*, *y(center)*, and *dist* values are averaged from each 2θ position. Bruker provides software (*GADDS*, Bruker-AXS, 2003) for calibration, for merging frames of various detector positions, and for the conversion of Debye rings (Figure 6) to a standard diffraction pattern (Intensity *vs*. 2θ pattern). In cases where there is high background, and the pattern of interest is reduced in intensity or obscured by background, a Bruker utility program is available to subtract frames. Thus, a frame involving only pure water may be subtracted from a frame obtained from a sample in water to obtain a frame with minimal background. Then, after conversion to a standard diffraction pattern from a frame, the pattern can be used as input to a data pattern analysis program (*e.g. MDI JADE*, Materials Data Inc., 1224 Concannon Blvd., Livermore, California, USA) for phase identification, cell-parameter refinement, or other analysis. Procedures for obtaining and processing powder diffraction patterns on the Bruker single-crystal diffractometer were presented in abstract form (Guggenheim, 2004) and as a Bruker application note (Guggenheim, 2005).

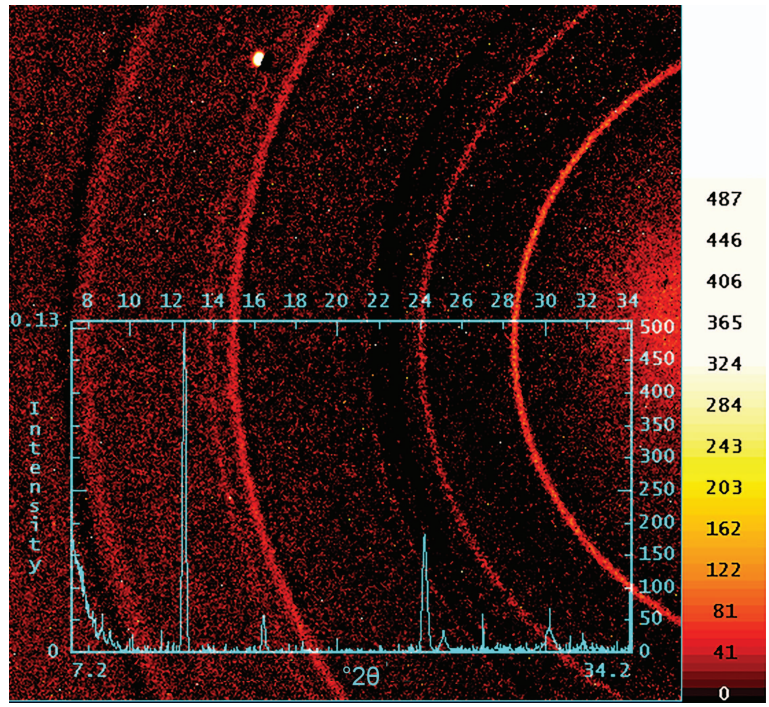

Figure 6. Frame of TiO_2 (NIST Standard Reference Material 674a) with the rutile structure, illustrating GADDS (Bruker) software that allows the conversion of Debye rings to a 'standard' powder diffraction pattern (Intensity *vs*. 2θ pattern), which is superimposed over the frame. A water suspension of ~150 mg of TiO_2 was used. The illustrated frame was produced by a (pixel-to-pixel) subtraction of a frame involving the diffraction of (pure) water from a frame involving the diffraction of TiO_2 + water. Both initial frames were for 20 min at 2θ = 20º at a detector distance of 12 cm, Mo radiation at 45 kV, 25 mA, and using a graphite monochromator and a MonoCap collimator under ambient conditions. Six Debye rings were obtained to produce a determined cell refinement of a = 4.602(7), c = 2.960(7) Å.

High-pressure reaction vessel

The pressure of the high-pressure reaction vessel is determined initially using a pressure transducer. By weighing the pressure vessel before and after an experiment, any loss of the pressurizing gas will be accompanied by a weight-loss. Because an oven is used as an external heat source, temperature within the oven is monitored with a standard thermometer or by using a thermocouple/temperature recorder.

APPLICATIONS AND PERFORMANCE

The design of the HPEC allows studies at ocean-floor or bore-hole conditions in aqueous liquids that may be saturated with various gases (*e.g*. CH_4, CO_2, O_2). Mixing these gases with inert gases (*e.g*. He, Ar) allows control of the fugacity. An example of an application of the HPEC is the work of Giesting *et al*. (2012a,b), which used a prototype HPEC to study the effect of CO_2 (gas and supercritical fluid) on the XRD patterns of Na-, K-, or Ca-exchanged montmorillonite to pressures of 640 bars and temperatures to ~50ºC.

To illustrate the utility of the current system, the observed d_{001} values *vs*. T in a series of experiments (Figure 7) are given for ~200 mg of montmorillonite (The Clay Minerals Society Source Clay, SWy-2, from Wyoming) in ~2 mL of brine (NaCl at 250% content of sea water, or 100 g/L), under CO_2 pressure of ~500 bars. After pressure was attained at 500 ± 10 bars, a valve

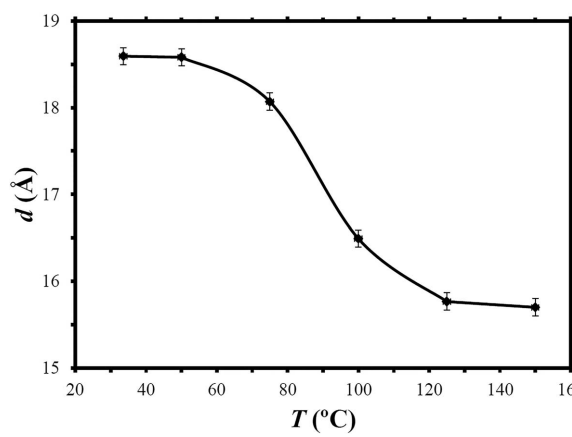

Figure 7. A d_{001} *vs*. T plot illustrating the change in d value as a function of temperature in a brine at $P(CO_2)$ = 500 bars. Pressure was not corrected for the increase in temperature above ambient because the HPEC remained closed during heating. See text for details.

located adjacent to the pressure port was closed. X-ray patterns [d_{001}] were obtained at 33.6, 50, 75, 100, 125, and 150ºC. Samples were allowed to rest for 30 min at each temperature prior to exposure, which was for 20 min. The closed valve prevented loss of fluids over the course of the heating experiments, but the temperature increase above 33.6ºC increased pressure accordingly. The d_{001} values ranged from 18.6 to 15.7 Å. A more detailed account of the experiments will be provided elsewhere.

ACKNOWLEDGMENTS

The authors thank Ms Jacqueline Kowalik, University of Illinois at Chicago, for Figure 7.

REFERENCES

Bassett, W.A. and Takahashi, T. (1965) Silver iodide polymorphs. *American Mineralogist*, **50**, 1576–1594.

Bruker-AXS (2003) General Area Detector Diffraction System, GADDS, v. 4.1.14.

Giesting, P., Guggenheim, S., Koster van Groos, A.F., and Busch, A. (2012a) Interaction of carbon dioxide with Na-exchanged montmorillonite at pressures to 640 bars: Implications for CO_2 sequestration. *International Journal of Greenhouse Gas Control*, **8**, 73–81.

Giesting, P., Guggenheim, S., Koster van Groos, A.F., and Busch, A. (2012b) X-ray diffraction study of K- and Ca-exchanged montmorillonites in CO_2 atmospheres. *Environmental Science & Technology*, **46**, 5623–5630.

Guggenheim, S. (2004) Simulations of Debye-Scherrer and Gandolfi powder patterns using the Bruker SMART/APEX three-circle diffractometer system. *American Crystallographic Association Annual Meeting*, Chicago, Il., 18–22 July 2004.

Guggenheim, S. (2005) Simulations of Debye-Scherrer and Gandolfi patterns using a Bruker SMART/APEX diffractometer system. *Bruker-AXS Application Notes Series*, **373**, 1–8.

Guggenheim, S. and Koster van Groos, A.F. (2003) A new gas hydrate phase: Synthesis and stability of clay–methane hydrate intercalate. *Geology*, **31**, 653–656.

Hazen, R.M. and Finger, L.W. (1982) *Comparative Crystal Chemistry*, John-Wiley and Sons, New York, 231p.

Koster van Groos, A.F. and Guggenheim, S. (2009) The stability of methane hydrate intercalates of montmorillonite and nontronite: Implications for carbon storage in ocean-floor environments. *American Mineralogist*, **94**, 372–379.

Koster van Groos, A.F., Guggenheim, S., and Cornell, C. (2002) Elevated-pressure, low-temperature environmental chamber for powder X-ray diffractometers. *Reviews of Scientific Instruments*, **74**, 273–275.

Mauron, Ph., Bielmann, M., Remhof, A., and Züttel, A. (2011) High-pressure and high-temperature x-ray diffraction cell for combined pressure, composition, and temperature measurements of hydrides. *Review of Scientific Instruments*, **82**, 065108-1–065108-7.

Toulemonde, P., Goujon, C., Laversenne, L., Bordet, P., Bruyère, R., Legendre, M., Leynaud, O., Prat, A., and Mezouar, M. (2014) High pressure and high temperature in situ X-ray diffraction studies in the Paris-Edinburgh cell using a laboratory X-ray source. *High Pressure Research*, **34**, 167–175.

Van Valkenburg, A. (1962) High-pressure microscopy. Pp. 87–94 in: *High-Pressure Measurement* (A.A. Giardini and E.C. Lloyd, editors). Butterworth, Washington, D.C..

(*Received 25 September 2014; revised 16 December 2014; Ms. 918; AE: M.A. Velbel*)

Clays and Clay Minerals, Vol. 62, No. 6, 477–499, 2014.

MINERALOGICAL AND GEOCHEMICAL CHARACTERISTICS AND GENESIS OF THE GÜZELYURT ALUNITE-BEARING KAOLINITE DEPOSIT WITHIN THE LATE MIOCENE GÖRDELES IGNIMBRITE, CENTRAL ANATOLIA, TURKEY

Selahattin Kadir[1,*], Tacit Külah[1], Muhsin Eren[2], Nergis Önalgil[1], and Ali Gürel[3]

[1] Eskişehir Osmangazi University, Department of Geological Engineering, TR-26480 Eskişehir, Turkey
[2] Mersin University, Department of Geological Engineering, TR-33343 Mersin, Turkey
[3] Niğde University, Department of Geological Engineering, TR-51200 Niğde, Turkey

Abstract—The Güzelyurt kaolinite deposit is an important source of raw material for the ceramics industry in Turkey. No detailed mineralogical or geochemical characterizations of this deposit have been undertaken previously and these were the goals of the present study. The Güzelyurt alunite-bearing kaolinite occurs along a fault zone in the Late Miocene Gördeles ignimbrite, which consists of dacitic and andesitic tuffs. Horizontal and vertical mineralogical zonations with gradual transitions were observed within the alteration zone. The inner kaolinite, alunite, and 7 Å halloysite zones progress horizontally outward to a smectite zone; and native sulfur- and cinnabar-bearing alunite with 7 Å halloysite and porous silica zones increase as one progresses up through the profile. Fe-(oxyhydr)oxide phases associated with native sulfur and cinnabar demonstrate that multiple hydrothermal-alteration processes resulted in kaolinization and alunitization of the deposit. The kaolinization of feldspar, Fe-(oxyhydr)oxidation of hornblende and mica, the presence of kaolinite as stacked and, locally, book-like forms, and of 7 Å halloysite tubes, and smectite flakes as a blanket on altered volcanic relicts indicate an authigenic origin for this deposit. The leaching of Si + Mg + K and Ba + Rb, the retention of Sr, the enrichment of light rare earth elements relative to the heavy rare earth elements, and the negative Eu anomalies suggest that fractionation of plagioclase and hornblende occurred within the volcanics. The oxygen- and hydrogen-isotopic values of the kaolinite, 7 Å halloysite, smectite, and smectite + kaolinite fractions reflect a steam-heated environment at temperatures in excess of 100ºC. An increase in the δD and $\delta^{18}O$ values of 7 Å halloysite relative to kaolinite suggests its formation under steam-heated magmatic water, the mixing of steam and meteoric water near the surface, and evaporation. The oxygen- and sulfur-isotopic compositions of alunite suggest the direct influence of steam-derived sulfur. The Güzelyurt alunite-bearing kaolinite deposit is inferred to have formed after an increase in the (Al±Fe)/Si ratio and the leaching of alkali elements, which are driven by the sulfur-bearing low-temperature hydrothermal alteration of feldspar, hornblende, and volcanic glass under acidic conditions within the Neogene dacitic and andesitic tuffs.

Key Words—Alunite with 7 Å halloysite, Geochemistry, Hydrothermal Alteration, Ignimbrite, Kaolinite, Micromorphology, Turkey.

INTRODUCTION

Kaolinite deposits generated by hydrothermal action or weathering, or both, within volcanic units, are common in Anatolia (Kadir and Karakaş, 2002; Arslan *et al*., 2006; Ece and Schroeder, 2007; Ece *et al*., 2008; Kadir and Akbulut, 2009; Kadir *et al*., 2011; Erkoyun and Kadir, 2011; Kadir and Erkoyun, 2013). In the Güzelyurt area, the kaolinite deposit has a reserve of ~2,000,000 tons as estimated by a systematic exploration program of the General Directorate of Mineral Research and Exploration of Turkey (MTA) during the period 1975–1977 (Küçüksille, 1979). A previous study, based on the geology and mineralogy of the Güzelyurt kaolinite deposit and its use as an industrial raw material, was completed by Fujii *et al*. (1995). No detailed information was provided in terms of polarized-light microscopy; differential thermal and thermogravimetric analyses; scanning and transmission electron microscopy; geochemical modeling of mass gains and losses of major, trace, and rare-earth elements during alteration; crystal chemistry; or stable isotope composition of this kaolinite deposit which is an important source of raw materials for the ceramics and paper industries in Turkey. The present study focused on the mineralogy, micromorphology, geochemistry, and stable-isotope geochemistry of the Güzelyurt kaolinites within the volcanic units which developed in a tectonically controlled hydrothermal system. New data are provided to help explain the physicochemical conditions of the hydrothermal alteration processes and genesis of the kaolinite, 7 Å halloysite, and associated alunite within the volcanic units in Anatolia.

* E-mail address of corresponding author:
skadir_esogu@yahoo.com
DOI: 10.1346/CCMN.2014.0620603

GEOLOGICAL SETTING AND GENERAL FEATURES OF THE KAOLINITE DEPOSIT

The basement rocks of the study area consist of Paleozoic metamorphic rocks (calc-schist, quartz-schist,

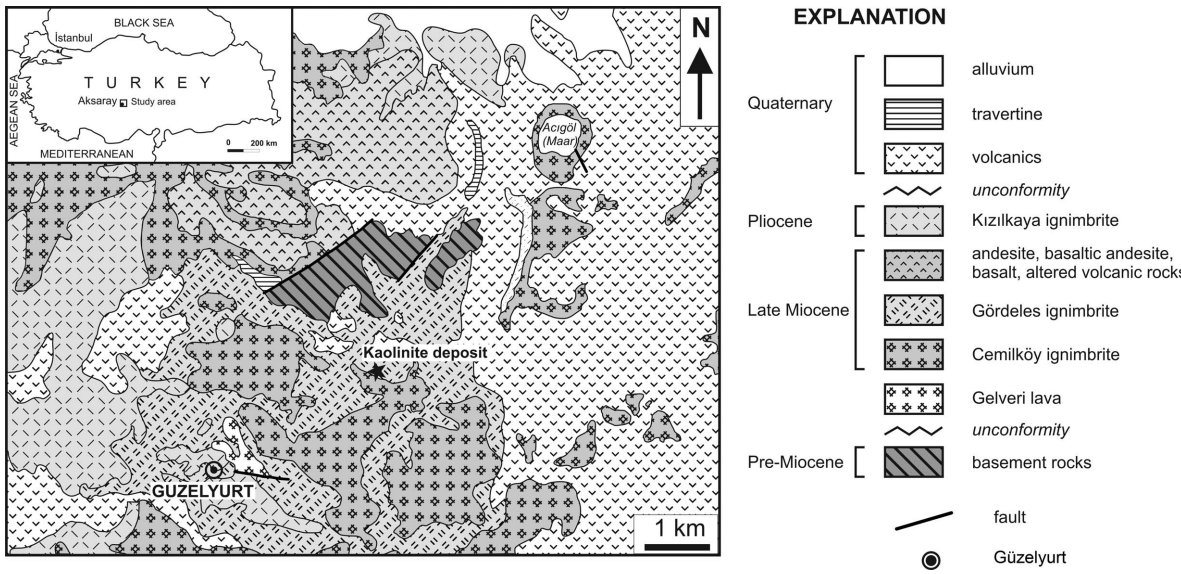

Figure 1. Simplified geological map of the Güzelyurt area (modified from Dönmez *et al.* 2005).

gneiss, and marble) of the Kırşehir Massif. These rocks are overlain tectonically by Mesozoic ophiolitic rocks and were intruded by Senonian plutonic rocks (Figures 1, 2). The basement rocks are overlain unconformably by lacustrine sediments intercalated with volcanic rocks of the Late Miocene Ürgüp Formation. These volcanics are the Sarımadentepe, Cemilköy, and Gördeles ignimbrites, and the Gelveri lava. The Quaternary units consist mainly of volcanics including basalt, andesite, rhyolite, cinder cones, pyroclastics, travertine, and alluvium. The Güzelyurt kaolinite deposit is found within the Ürgüp Formation and extends along a NE–SW-trending normal fault related to the major Tuz Gölü Fault. The kaolinite deposit is ~300 m long, 100 m wide, and 25 m thick (Figures 3, 4), and is underlain mainly by pinkish-white, massive, and fractured marble consisting of coarse- or

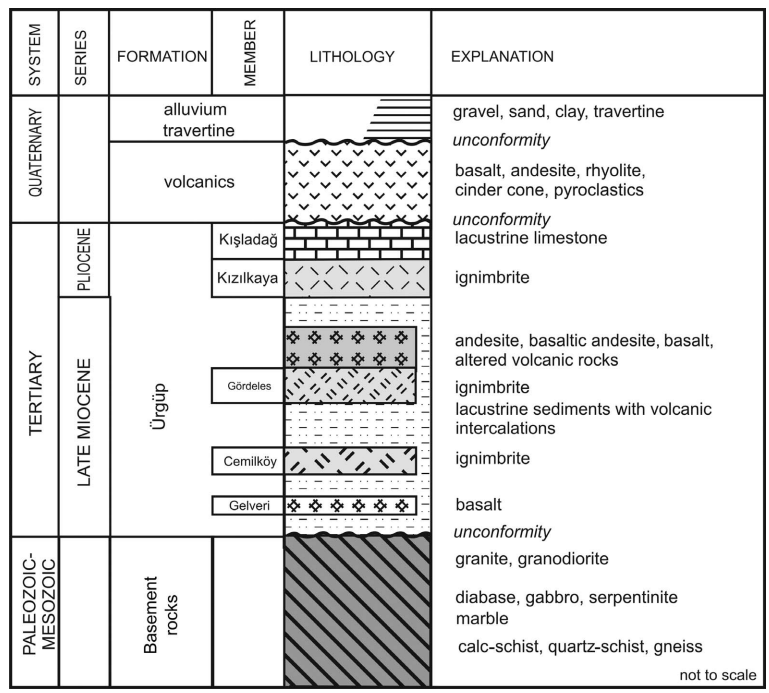

Figure 2. Generalized stratigraphic column of the study area (modified after Dönmez *et al.*, 2005).

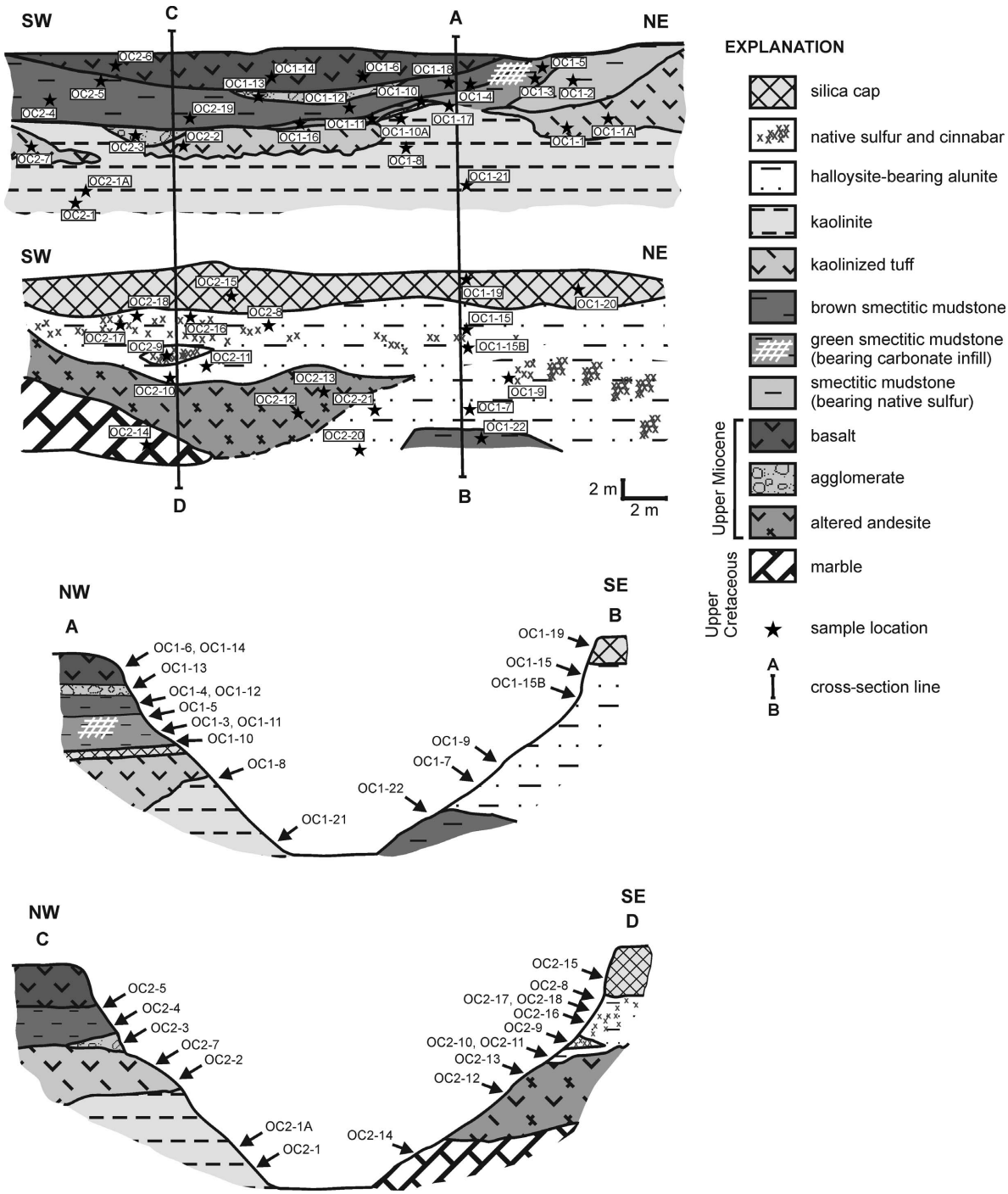

Figure 3. Sketch and profiles of the Güzelyurt kaolinite deposit.

medium-grained calcite crystals. The kaolinite deposit was formed by hydrothermal alteration of dacite- and andesite-type Gördeles ignimbrite (Temel *et al.*, 1995). Alteration zones are present in these deposits. Kaolinized dacitic and andesitic tuffs crop out at the lower part of the deposit, and the alunite + 7 Å halloysite zone crops out in the andesitic unit in the central and upper parts of the deposit. The intensity of kaolinization decreases and alunite increases upward. These units enclose native sulfur and cinnabar disseminations and are covered by a porous silica cap. A smectite zone occurs outside the kaolinite deposit. The lower part of the smectite zone is

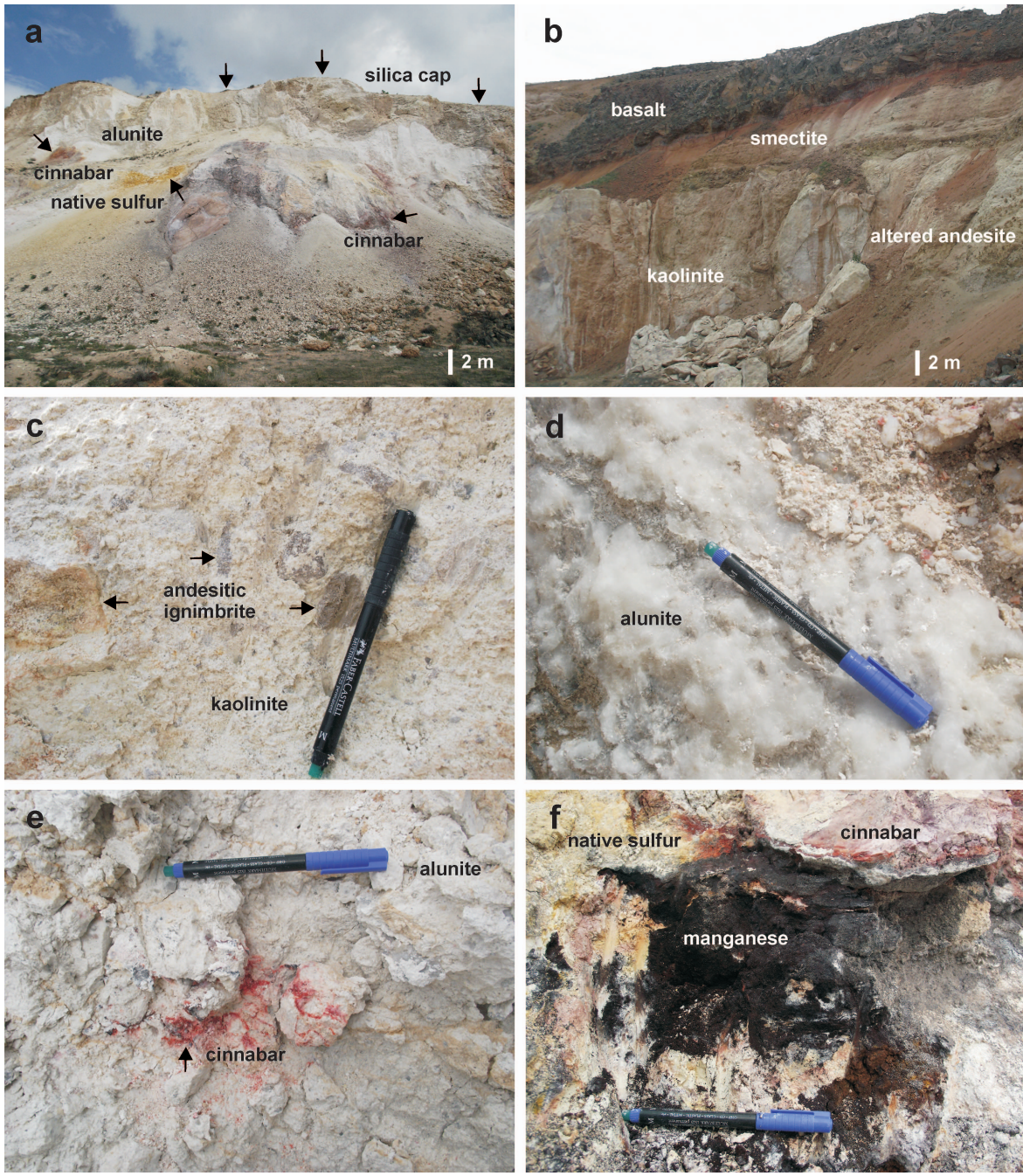

Figure 4. Field view of: (a) silica cap on the uppermost kaolinite deposit; (b) development of smectite between kaolinite and basaltic lava; (c) presence of andesite clasts in kaolinized units; (d) close-up view of alunite; (e) close-up view of the cinnabar associated with alunite; and (f) close-up view of cinnabar, manganese, and native sulfur associated with alunite.

pale green while the upper part is a reddish-brown, laminar, plastic, and silty smectitic mudstone. This mudstone is fractured and encloses light purple-colored native sulfur and cinnabar. The smectite zone also encloses agglomeratic pyroclastic flow lenses that have an andesitic character and are overlain by black, gray–dark gray and brown fractured basaltic lava.

MATERIALS AND METHODS

In the field, typical stratigraphic sections were measured to study vertical and lateral variations within the Güzelyurt kaolinite deposit that occurred in the Gördeles ignimbrite. Characteristic fresh and altered samples were collected (Figure 3) and examined under a polarizing microscope (Nikon-LV 100Pol).

The mineralogical characteristics of the samples were determined by powder X-ray diffraction (XRD) (Rigaku Geigerflex), scanning electron microscopy (SEM-EDX) (JEOL JSM 84A-EDX), and transmission electron microscopy (TEM) (JEOL JEM-21007). The clay mineralogy was determined after separation of the clay fraction (<2 μm) by sedimentation, followed by centrifugation of the suspension after an overnight dispersion in distilled water. The clay particles were dispersed by ultrasonic vibration for ~15 min. Three oriented specimens of the <2 μm fraction of each sample were prepared by air drying, ethylene-glycol solvation at 60ºC for 2 h, and thermal treatment at 550ºC for 2 h. The mineralogy of the bulk samples was determined by XRD with CuKα radiation and a scanning speed of 1º2θ min^{-1} at the Turkish Petroleum Corporation (TPAO). Semi-quantitative abundances of rock-forming minerals were obtained using Brindley's (1980) external standard method, whereas the relative abundances of clay-mineral fractions were determined using their basal reflections and the mineral intensity factors described by Moore and Reynolds (1989).

Representative clay-dominated bulk samples were prepared for the SEM-EDX analysis by adhering the fresh, broken surface of each sample onto an aluminum sample holder with double-sided tape and coating thinly (350 Å) with gold using a Giko ion coater. The clay particles for TEM analysis were dispersed in an ultrasonic ethanol bath for ~30 min, and one drop of each clay suspension was placed on carbon-coated copper grids and dried at room temperature.

Differential thermal and thermogravimetry analyses (DTA-TG Rigaku TAS 100 E) were performed on the selected samples at Eskişehir Osmangazi University. The DTA-TG curves were obtained from 10 mg of powdered sample in a Pt sample holder, heated at an average rate of 10ºC/min with an alumina reference.

Chemical analyses of 20 fresh and altered volcanic whole-rock samples were performed at the Acme Analytical Laboratories Ltd. (Canada) using inductively coupled plasma–atomic emission spectroscopy (ICP-AES) for major and trace elements and inductively coupled plasma–mass spectroscopy (ICP-MS) for rare-earth elements (*REE*). The detection limits for the analyses were between 0.01 and 0.1 wt.% for major elements, between 0.1 and 5 ppm for trace elements, and between 0.01 and 0.5 ppm for the *REE*.

Enrichment and depletion of elements were estimated using the procedure of MacLean and Kranidiotis (1987). In these calculations, zirconium was assumed to be the most immobile element, based on calculated correlation coefficients with other elements. All samples were grouped on the basis of degree of alteration (average result from each group), and the gains and losses of components were calculated using a starting mass of 100 g of average fresh, anhydrous sample. The equation used in calculations can be written for SiO_2 (MacLean and Kranidiotis, 1987) as follows:

$$SiO_2 = \frac{SiO_2 \text{ wt.\% altered}}{\text{Zr ppm altered}} \times \text{Zr ppm fresh}$$

Gain and loss of mass (ΔC_i) for each element were determined by subtracting the calculated values of reconstructed compositions (RC) from the concentrations of components in the least-altered samples using the formula given above.

Approximate structural formulae for kaolinite, 7 Å halloysite, and smectite were determined for the <2 μm clay samples with the largest 7 Å halloysite and smectite contents. These samples were sieved to <2 mm; 100 g of the sieved sample was mixed with deionized water and disaggregated using a Stir-pak mixer head and mixer controller. The <2 μm fractions were subsequently isolated from the silt (2–50 μm) using repeated siphoning of the dispersed material. The clay fractions were separated by sedimentation of the suspension after 24 h of dispersion in distilled water and removal of the upper 5 cm, followed by centrifugation for 10 min at $2451 \times g$ (4000 rpm) using a Hettich Rotofix 32A centrifuge. The silica and phosphorous content were corrected for impurities such as amorphous materials and accessory P_2O_5, which was not removed and not detected by XRD.

The approximate structural formulae of kaolinite and 7 Å halloysite were calculated based on $O_{10}(OH)_8$, and of smectite based on $O_{20}(OH)_4$ by the following procedure: the tetrahedral sites of kaolinite and of 7 Å halloysite were filled with Si and Al to a sum of four, and tetrahedral sites of smectite were filled with Si and Al as needed to a sum of eight. The remaining Al in kaolinite, 7 Å halloysite, and smectite was assigned to octahedral sites. All iron, considered to be ferric, and all Mn and Ti were assigned to the octahedral site. Ca, Na, and K were deemed to be exchangeable interlayer cations.

Eight kaolinite-, 7 Å halloysite-, smectite-bearing clay fractions were purified and analyzed for the H and O stable isotopes in the Cornell Isotope Laboratory at Cornell University, New York. The isotope corrections were performed using a two-point normalization (regression) based on international standards (IAEA CO-1 and IAEA CO-8) for $\delta^{18}O$ and CH-7 and benzoic acid for δD. The analyses were performed using a Thermo Delta V isotope ratio mass spectrometer interfaced with a temperature-conversion elemental analyzer. The delta values for ^2H and ^{18}O were measured against the primary reference scale of Clayton and Mayeda (1963). The data are reported in standard delta notation as per mil deviations from V-SMOW (Vienna Standard Mean Ocean Water). The standard deviation for internal standard benzoic acid for $\delta^{18}O$ is 1.01‰ and for δD is 1.24‰.

The $\delta^{34}S + \delta^{18}O$ were determined on seven alunite samples which were selected carefully by handpicking under a binocular microscope. Stable-isotope analyses ($\delta^{34}S + \delta^{18}O$) were conducted at the University of Arizona Department of Geosciences using an MAT

261-8 mass spectrometer. The results of $\delta^{34}S$ (referenced to V-CDT – Vienna Canyon Diablo Troilite) and $\delta^{18}O_{sulfate}$ (referenced to V-SMOW) are listed in Table 6.

$\delta^{34}S$ was measured on SO_2 gas in a continuous-flow gas-ratio mass spectrometer (ThermoQuest Finnigan Delta PlusXL, Tucson, Arizona, USA). The samples were combusted at 1030ºC with O_2 and V_2O_5 using an elemental analyzer (Costech, Tucson, Arizona, USA) coupled to the mass spectrometer. Standardization is based on international standards OGS-1 and NBS123 (Hosono *et al*. 2014), and several other sulfide and sulfate materials for sulfur that have been compared between laboratories. Calibration is linear in the range −10 to +30‰. Precision is estimated to be ±0.15‰ or better (1σ) based on repeated internal standards.

The $\delta^{18}O$ of sulfate was measured on CO gas in a continuous-flow gas-ratio mass spectrometer (Thermo Electron Delta V, Tucson, Arizona, USA). The samples were combusted with excess C at 1350ºC using a thermal combustion elemental analyzer (ThermoQuest Finnigan, Tucson, Arizona, USA) coupled to the mass spectrometer. Standardization is based on international standard OGS-1. Precision is estimated to be ±0.4‰ or better (1σ), based on repeated internal standards.

RESULTS

Mineralogical determinations

The dacitic and andesitic ignimbrite has a porphyritic texture and consists of plagioclase, hornblende, biotite, andesitic rock fragments, and devitrified volcanic glass (Figure 5). The plagioclase often shows argillization, whereas the hornblende and mica crystals are (oxyhydr)-oxidized (Figure 5a–d).

The XRD analyses of the bulk samples and clay fractions taken from the Güzelyurt kaolinite deposit are listed in Table 1 and traces are shown in Figure 6. Kaolinite, 7 Å halloysite, alunite, and smectite-type alteration products are accompanied by feldspar, quartz, and opal-CT and locally by calcite and accessory hornblende and dolomite. Kaolinite and alunite are present in

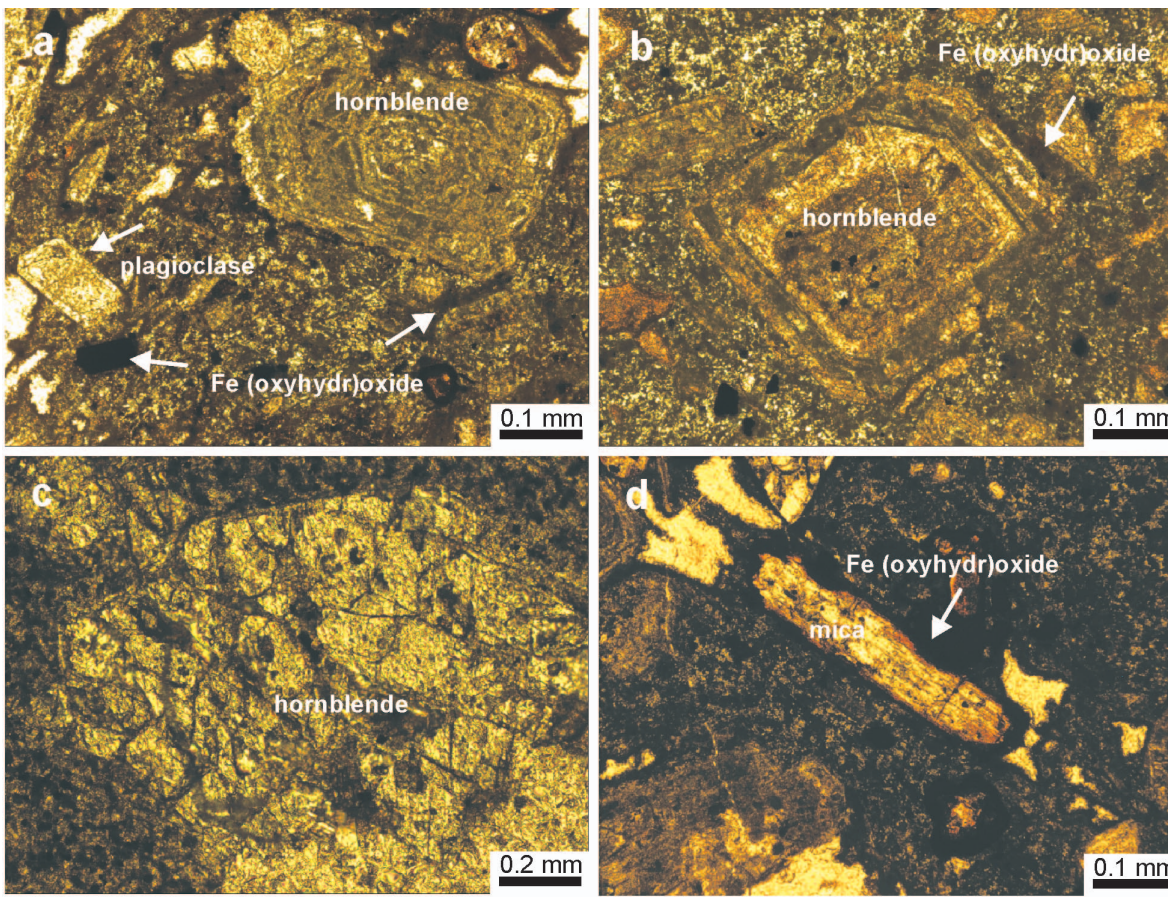

Figure 5. Photomicrographs of: (a,b) Fe-(oxyhydr)oxide hornblende crystals; plain-polarized light (OC2-3); (c) altered amphibole crystal associated with Fe-(oxyhydr)oxide; plain-polarized light (OC1-4); and (d) Fe-(oxyhydr)oxide mica crystal; plain-polarized light (OC2-3).

Table 1. Mineralogical compositions of the fresh and altered samples.

Sample	Rock type	kln	hal	alu	sme	qz	opl	hbl	fsp	dol
OC1-1	Altered tuff		+	+++		acc				
OC1-1A	Altered tuff			+++++						
OC1-2	Mudstone	++++			+					
OC1-3	Mudstone	+			++++	acc			acc	
OC1-4	Mudstone			acc	+++++			acc		
OC1-5	Mudstone				+++++					
OC1-7	Altered tuff	+		++++		acc				
OC1-8	Altered tuff	+++			++	acc				
OC1-10	Altered tuff	acc			++++	acc			acc	
OC1-10A	Altered tuff	++++			+	acc				
OC1-15	Altered tuff		++++			+	acc			
OC1-15B	Altered tuff		++++	++		acc	acc			
OC1-16	Mudstone	+			+++++	acc			acc	
OC1-17	Mudstone	++++			+	acc				
OC1-18	Mudstone				+++++					
OC1-19	Silica					+++	++			
OC1-20	Silica					+++++				
OC2-1	Altered tuff	++++		+		acc	acc			
OC2-2	Altered tuff		++++	+		acc	acc			
OC2-5	Mudstone				+++++	acc			acc	
OC2-7	Altered tuff		++++	+		acc	acc		acc	
OC2-8	Altered tuff			+++++					acc	acc
OC2-9	Mudstone	acc		+++++		acc				
OC2-10	Altered tuff			+++++		acc	acc		acc	
OC2-11	Altered tuff	acc		+++++			+			
OC2-12	Altered tuff			+++		+	acc			
OC2-13	Altered tuff			+		+	+++	acc		
OC2-15	Silica					+++++				
OC2-16	Altered tuff		++++	+		acc				
OC2-17	Altered tuff		++++	+	+	acc				
OC2-18	Altered tuff		++	++++			acc			
OC2-19	Mudstone	acc			+++++	acc			acc	
OC2-20	Altered tuff			+++++		acc				
OC2-21	Altered tuff			+++++		acc	+			

kln: kaolinite, hal: 7 Å halloysite, alu: alunite, sme: smectite, qz: quartz, opl: opal-CT, hbl: hornblende, fsp: feldspar, dol: dolomite, acc: accessory, +: relative abundance of mineral.

the central part of the deposit. Kaolinite appears in the NW part of the deposit, whereas alunite and alunite-bearing kaolinite are present in the SE part of the deposit. Kaolinite dominates in the lower level, and 7 Å halloysite-bearing alunite dominates in the middle and upper levels of the SE part of the kaolinite deposit. An inverse relationship exists between kaolinite and alunite + 7 Å halloysite in the deposit. Smectite was formed as a result of the alteration of basaltic units and predominates in the green and reddish-brown mudstones, stratigraphically above and laterally away from the deposit.

Kaolinite and 7 Å halloysite are identified by sharp peaks at ~7.18 and 3.58 Å and non-basal reflections of doublets and triplets at 4.47, 4.37, 2.57, 2.50, 2.38, 2.34, and 2.30 Å (Brindley, 1980; Wilson, 1987) (Figure 6). The basal reflection at 7.2 Å is not affected by ethylene-glycol treatment. The 7.2 Å peak collapsed at 550ºC due to dehydroxylation. Alunite is identified by sharp peaks at 5.72, 4.95, 3.49, 2.98, 2.88, 2.28, 1.90, and 1.49 Å.

Smectite was identified by a narrow peak at 15.17 Å which expanded to 18.09 Å with ethylene-glycol treatment and then collapsed to 10.39 Å after heating at 550ºC for 2 h (Figure 6). The d_{060} value of 1.50 Å indicated dioctahedral smectite (Moore and Reynolds, 1989). The XRD background of some of the alunite-kaolinite-bearing samples is slightly elevated, possibly due to the presence of a poorly crystalline phase. The opal-CT is recognized by 4.32 and 4.06 Å reflections and a slight elevation of the XRD background of some of the kaolinite-bearing samples, possibly due to the presence of a poorly crystalline phase.

SEM-EDX, TEM, and mineral chemistry

Kaolinite occurs as platy crystals with euhedral to subhedral hexagonal outlines, mostly arranged face-to-face in elongated book-like stacks or as vermiform crystals (Figure 7a,b). The kaolinite plates have dimensions of 2 μm × 5 μm. In the altered volcanic units, 7 Å

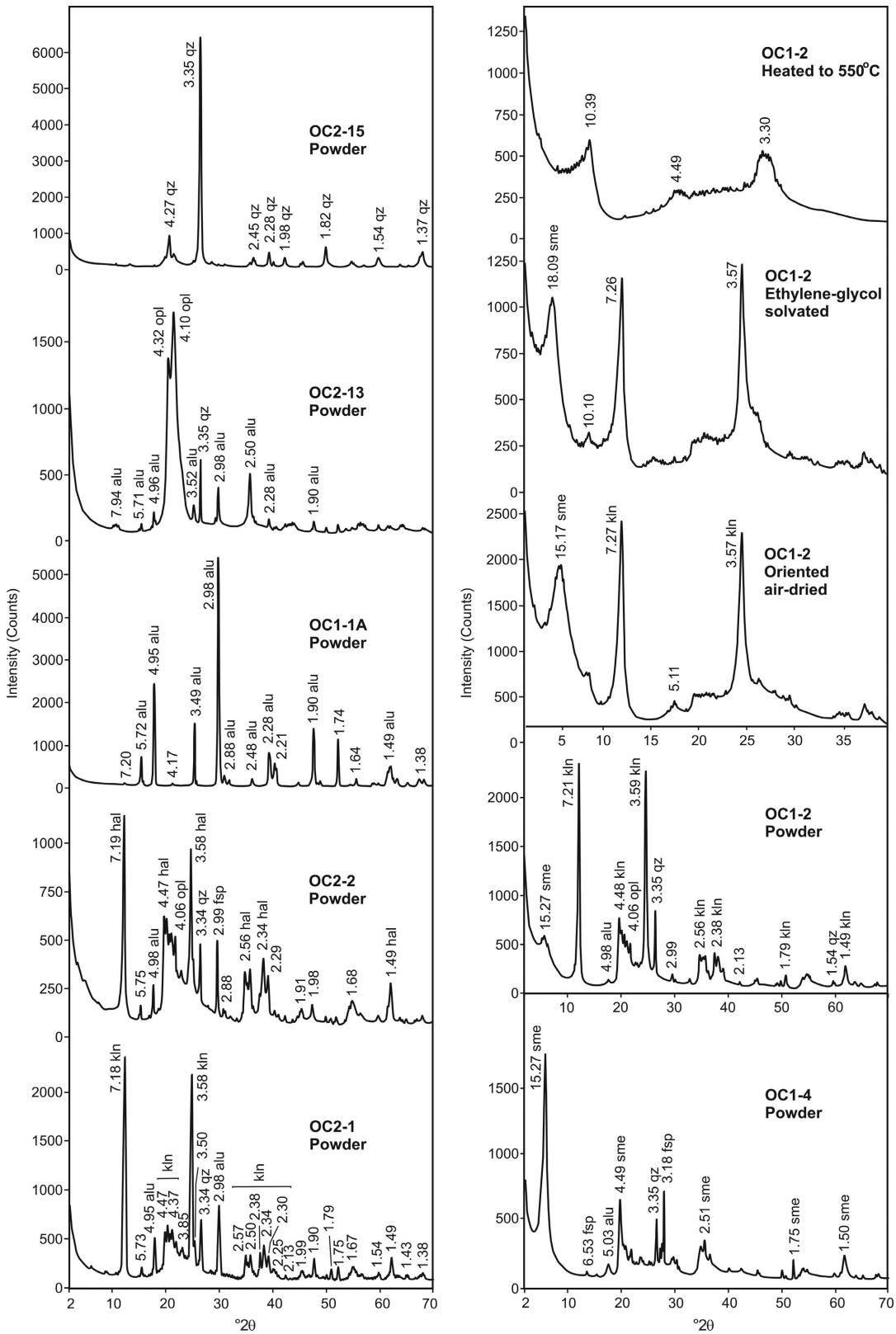

Figure 6. XRD patterns of altered volcanic samples. kln: kaolinite, hal: 7 Å halloysite, alu: alunite, sme: smectite, qz: quartz, fsp: feldspar, opl: opal-CT.

halloysite occurs as masses of rod-like forms coexisting with cubic alunite crystals (2–7 μm) and devitrified volcanic glass (Figure 7c–f).

Smectite crystals exhibit a well defined, web-like morphology, which developed authigenically as grain coatings on relict feldspar and volcanic grains (Figure 7g–j). These individual flaky crystals range from 1 to 5 μm in diameter.

The silica-cap samples are characterized by lepispheres composed of sub-rounded accumulations of acicular crystals (~3 μm) of opal-CT (Figure 7k). The gypsum crystals have a highly porous, elongate, irregular prismatic lath texture (Figure 7l).

The approximate structural formulae of kaolinite, 7 Å halloysite, and smectite were calculated from chemical analyses of the clay fractions (Table 2). The resulting

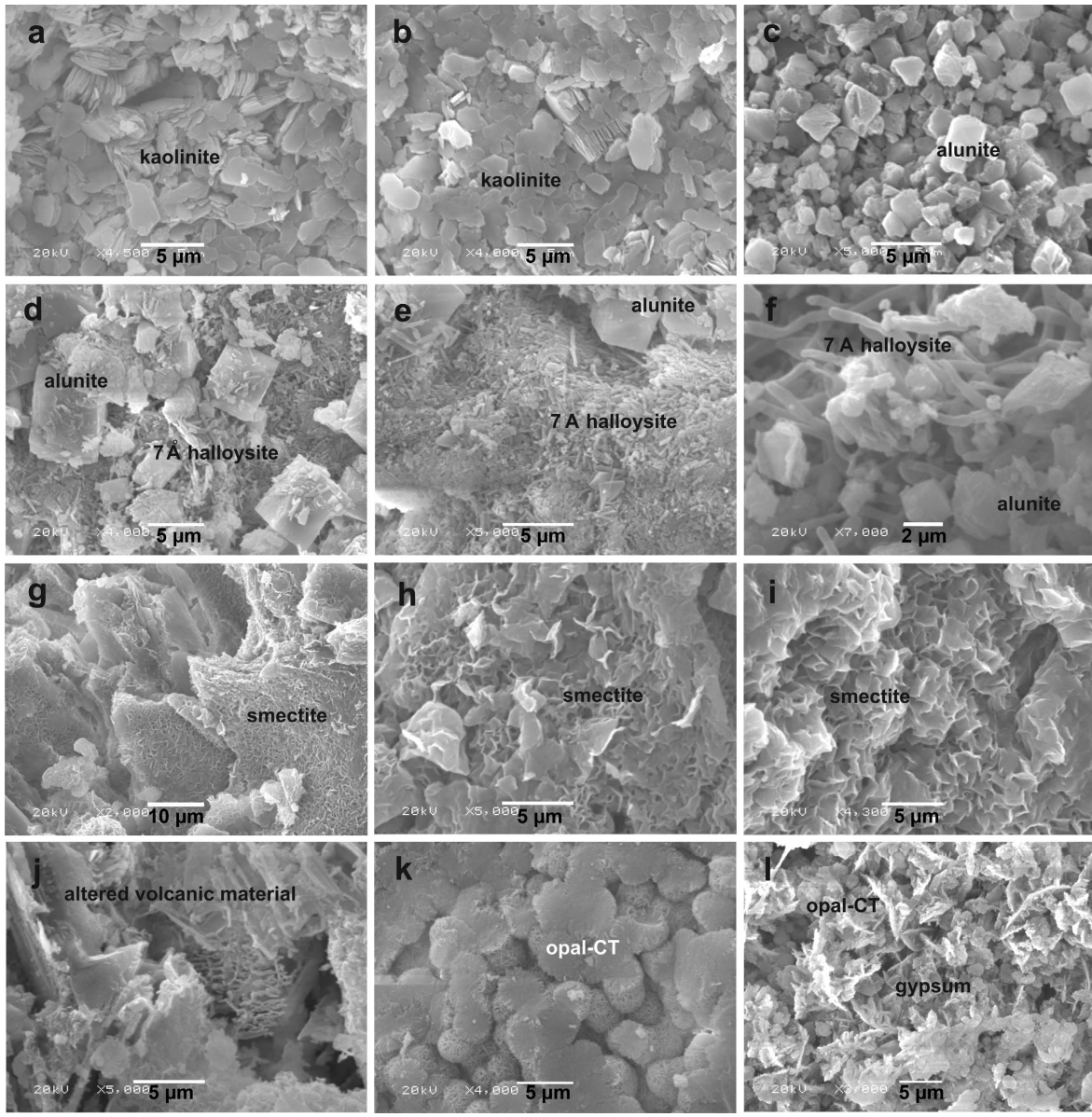

Figure 7. SEM images of: (a,b) euhedral kaolinite-crystal stacks, with vermiform structure (OC2-1); (c) euhedral cubic alunite crystals (OC1-1A); (d) euhedral cubic alunite crystals in association with rod-like 7 Å halloysite (OC2-2); (e) subparallel 7 Å halloysite rod coexisting with alunite in a microfracture (OC2-2); (f) development of a sub-parallel 7 Å halloysite rod between alunite crystals (OC1-1); (g–i) the formation of smectite flakes in dissolution voids of altered volcanic materials (OC1-4); (j) highly altered volcanic materials associated with a highly porous structure (OC1-2); (k) acicular crystal accumulation and development of lepisphere structures of opal-CT coexisting with minor gypsum crystals (OC2-15); and (l) prismatic laths of gypsum with a rosette-like structure (OC2-15).

Table 2. Chemical compositions (wt.%) and structural formulae for purified kaolinite, 7 Å halloysite, and smectite samples.

Major oxides (wt.%)	OC2-1 kaolinite	OC2-2 7 Å halloysite	OC2-5 smectite
SiO_2	44.14	44.16	51.79
Al_2O_3	36.40	36.09	15.61
ΣFe_2O_3	1.71	2.28	7.86
MgO	0.39	0.71	3.14
CaO	0.34	0.61	2.21
Na_2O	0.62	0.05	0.20
K_2O	1.27	0.34	0.47
TiO_2	0.96	0.65	0.43
MnO	0.01	0.01	0.06
LOI	14.00	14.90	17.90
Total	99.84	99.80	99.67
CIA	94.23	97.30	84.42
SiO_2/Al_2O_3	1.21	1.22	3.31
SiO_2/R_2O_3	1.16	1.15	2.20
Tetrahedral			
Si	3.90	3.92	7.67
Al	0.10	0.08	0.33
Σ	4.00	4.00	8.00
Octahedral			
Al	3.69	3.69	2.39
Fe	0.11	0.15	0.88
Mg	0.05	0.09	0.69
Ti	0.06	0.04	0.05
Mn	0.001	0.001	0.01
Σ	3.91	3.98	4.02
Interlayer			
Ca	0.03	0.06	0.35
Na	0.11	0.01	0.06
K	0.14	0.04	0.09
Σ	0.28	0.11	0.51
Tetrahedral charge	0.10	0.09	0.32
Octahedral charge	0.24	0.08	0.60
Total charge	0.34	0.17	0.92
Interlayer charge	0.31	0.16	0.85
xt/xo	0.41	1.02	0.53

formulae of kaolinite, 7 Å halloysite, and smectite are as follows: $(Si_{3.90}Al_{0.10})(Al_{3.69}Fe_{0.11}Mg_{0.05}Ti_{0.06}Mn_{0.001})(Ca_{0.03}Na_{0.11}K_{0.14})O_{10}(OH)_8$, $(Si_{3.92}Al_{0.08})(Al_{3.69}Fe_{0.15}Mg_{0.09}Ti_{0.04}Mn_{0.001})(Ca_{0.06}Na_{0.01}K_{0.04})O_{10}(OH)_8$, and $(Si_{7.67}Al_{0.33})(Al_{2.39}Fe_{0.88}Mg_{0.69}Ti_{0.05}Mn_{0.01})(Ca_{0.35}Na_{0.06}K_{0.09})O_{20}(OH)_4$, respectively.

The tetrahedral sites of kaolinite, 7 Å halloysite, and smectite are filled with Si cations which have been substituted by some of the Al. Al^{3+} is the abundant octahedral cation of kaolinite, 7 Å halloysite, and smectite. Traces of Fe^{3+}, Mg, Ti, and Mn, referred to as 'R', substitute for some of the Al. Thus, these clays are characterized as Fe-bearing kaolinite, 7 Å halloysite, and smectite.

The SiO_2/Al_2O_3 and SiO_2/R_2O_3 ratios of 1.21 and 1.16 for pure kaolinite, of 1.22 and 1.15 for pure 7 Å halloysite, and of 3.31 and 2.20 for pure smectite, respectively, are consistent with the ideal ratios reported by Jepson and Rowse (1975).

Determinations by TEM revealed that the Güzelyurt kaolinite exhibits euhedral, hexagonal forms with regular outlines characteristic of well crystallized kaolinite (Figure 8a–f). The kaolinite plates are up to 200 nm × 300 nm in size and 10–20 nm thick. The 7 Å halloysite exhibits tube-like forms, with a 70–100 nm diameter, and are ~10 nm thick and 450 nm long (Figure 8d–f).

DTA-TG

The DTA-TG curves for kaolinite, 7 Å halloysite, alunite, and smectite represent typical thermal reactions and are consistent with the results of XRD, SEM-EDX, TEM, and chemical analyses. The reaction of the Güzelyurt kaolinite and 7 Å halloysite upon heating

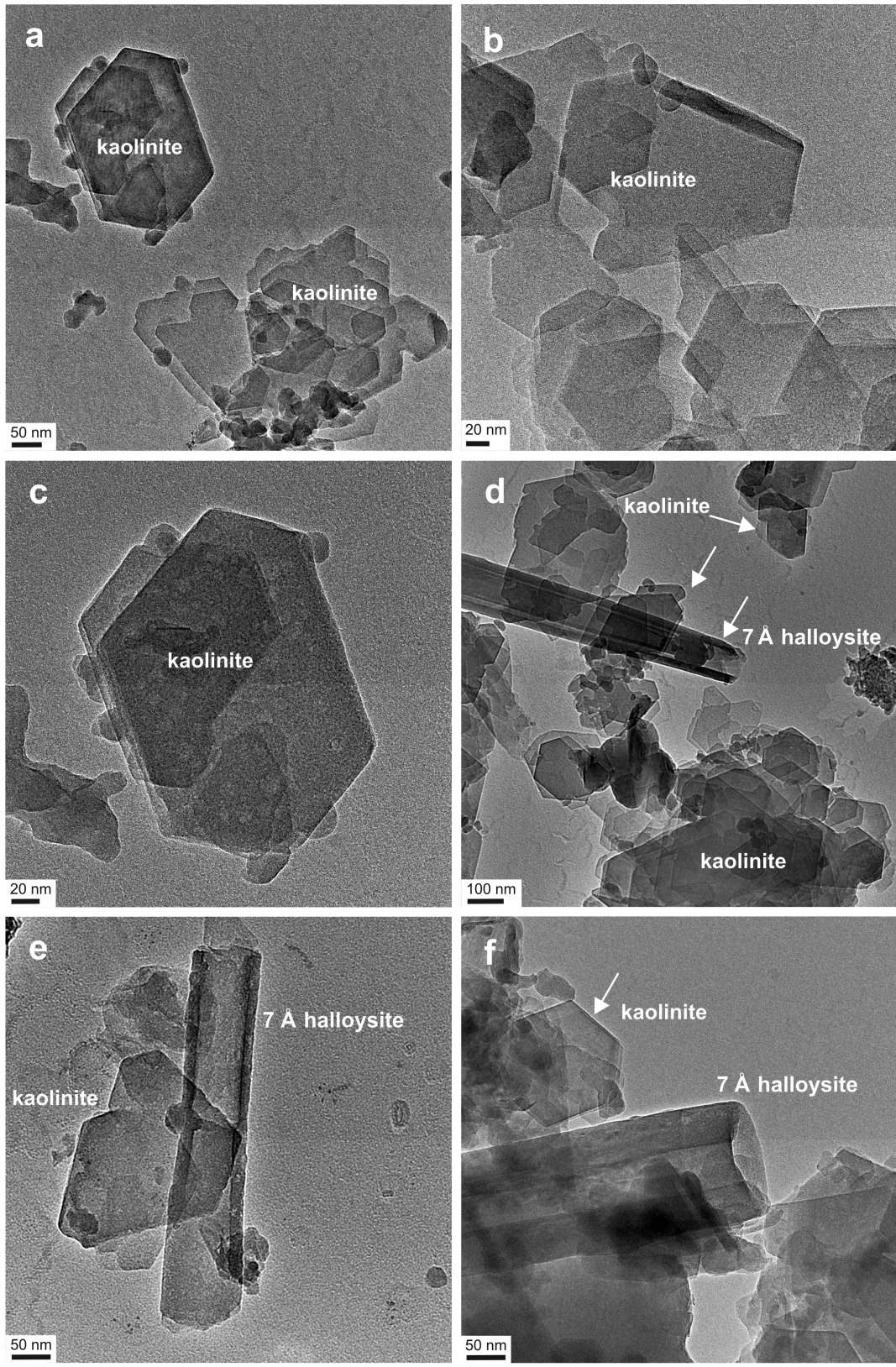

Figure 8. TEM image of: (a–c) hexagonal platy kaolinite crystals (OC2-1) and (d–f) rod-like 7 Å halloysite (OC2-2).

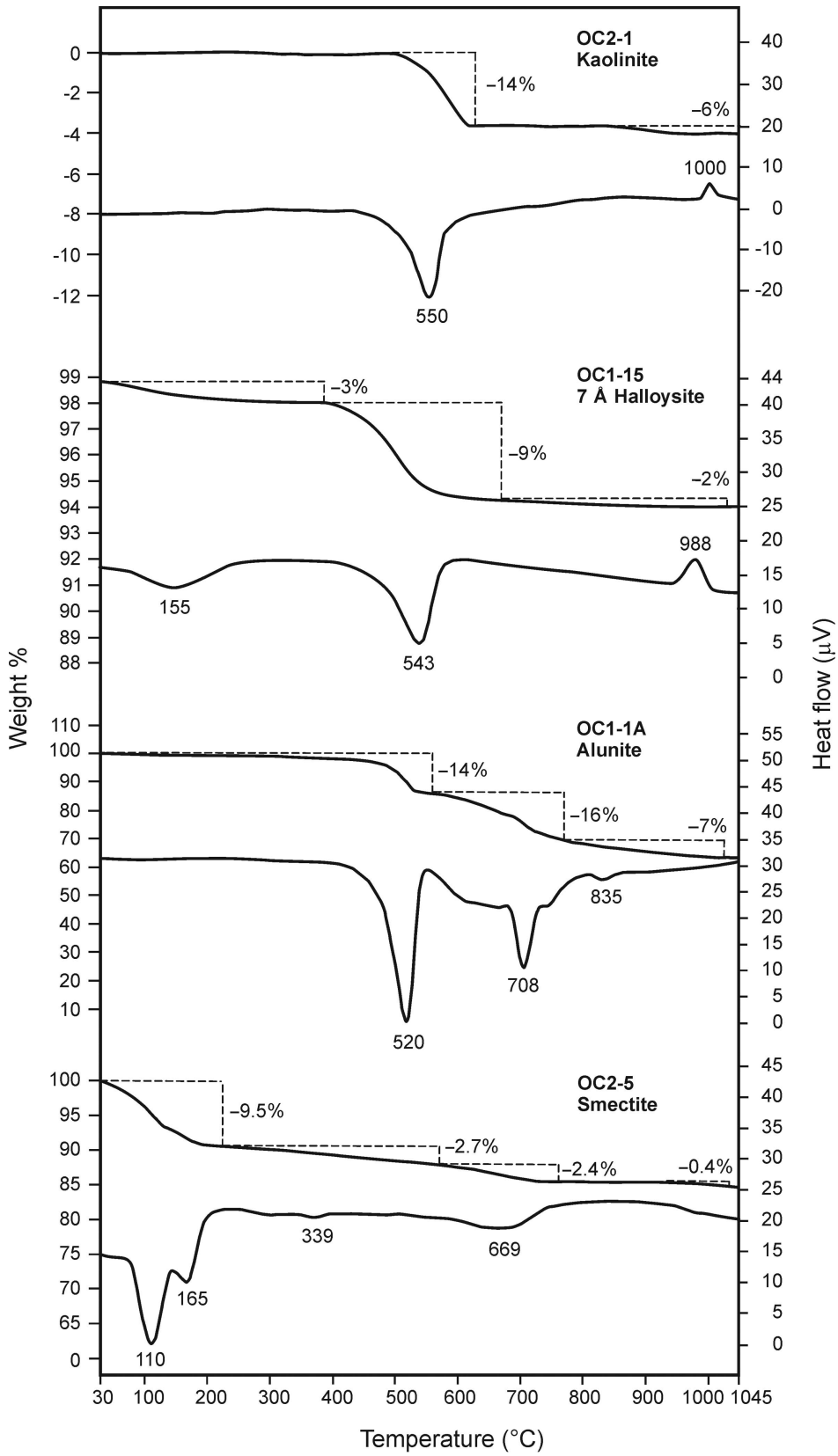

Figure 9. DTA-TG curves for kaolinite (OC2-1), 7 Å halloysite (OC1-15), alunite (OC1-1A), and smectite (OC2-5) samples.

show similar peaks (Figure 9). Kaolinite sample OC2-1 shows a strong and symmetrical endothermic peak at ~550ºC (weight loss = 14%) and an exothermic peak at 1000ºC (weight loss = 6%). The endothermic and exothermic peaks are attributed to the dehydroxylation of kaolinite rather than dickite and nacrite. Both dickite and nacrite have dehydroxylation peaks at higher temperatures, ~680ºC (MacKenzie, 1957; Paterson and Swaffield, 1987; Yuan and Murray, 1993; Chen *et al*., 2001; Lanson *et al*., 2002; Njoya *et al*., 2006). The 7 Å halloysite sample OC1-15 is characterized by two endothermic peaks at 155ºC (weight loss = 3%) and 543ºC (weight loss = 9%) and an exothermic peak at 988ºC (weight loss = 2%) (MacKenzie, 1957; Paterson and Swaffield, 1987).

The DTA-TG curves of alunite sample OC1-1A exhibited the first strong asymmetric endothermic peak at a temperature of 520ºC (weight loss = 14%), the second widespread peak at 708ºC (weight loss = 16%), and the last and faintest peak at 835ºC (mean 835ºC, weight loss = 7%) (Figure 9). The first endothermic peak is attributed to the initial dehydroxylation, the second and the final peaks represent elimination of sulfur due to the decomposition of alunite structure, as reported by Ece and Schroeder (2007).

The DTA-TG analysis of the smectite-dominated OC2-5 sample shows a large asymmetric endothermic peak at ~110−165ºC (weight loss 9.5%), a medium-sized endothermic peak at ~339ºC (weight loss = 2.7%), and a final, small endothermic peak at 669ºC (weight loss = 2.4%) (Figure 9). Similar peaks were obtained by Mackenzie (1957), Imai *et al*. (1969), Smykatz-Kloss (1974), Paterson and Swaffield (1987), and Jones and Galán (1988). The DTA curve shows a decline starting at ~900ºC, possibly reflecting decomposition to sintering phases.

Geochemistry

Chemical analyses of the Güzelyurt kaolinite samples are given in Table 3. The samples are characterized by large values of Al_2O_3 (avg. 11.14−23.87%), Fe_2O_3 (avg. 2.7−4.71%), SiO_2 (avg. 55.1−39.3%), and loss on ignition (LOI) (avg. 17.4−25.07%). The LOI is an important indicator for degree of alteration. Compared with kaolinite, the amount of Al_2O_3 + K_2O + LOI and SO_3 + Hg increases upward through the deposit sequence, concomitant with an increase in alunite and 7 Å halloysite. Sample OC1-9 is dominated by SO_3 (42.66%) and Hg (9.55 ppm), however, reflecting the presence of native sulfur and cinnabar, respectively.

Using mass gains and losses (MacLean and Kranidiotis, 1987), enrichments and depletions of major and trace elements from fresh to altered samples were observed (Table 4; Figure 10). Si, Mg, K, Ba, Rb, Y, and Pb were depleted during the alteration of feldspar, hornblende, biotite, and volcanic glass derived from the volcanic units. Conversely, Al, Fe, Ca, Hg, Sr, V, As, and Σ*REE* were enriched during this process.

Light *REE*s (*LREE*) such as La, Ce, and Nd were enriched relative to the heavy *REE*s (*HREE*) (Figure 11). The *LREE*s had an increasing intensity of degree of alteration within the volcanic units and exhibited a negative Eu anomaly in the kaolinized and alunitized materials.

Stable-isotope geochemistry

The results of D- and O-isotopic analyses of purified kaolinite, 7 Å halloysite, smectite, and smectite + kaolinite fractions are listed in Table 5 and plotted in Figure 12. The δD and $\delta^{18}O$ values of kaolinite and 7 Å halloysite range from −132.92‰ to −101.81‰, and from 0.56‰ to 7.64‰, respectively. The δD and $\delta^{18}O$ values of the smectite and smectite + kaolinite fraction

Table 3. Chemical compositions of the fresh and altered tuff samples.

Major oxides	Fresh tuff				Altered tuff						
(wt.%)	OC3-3	OC3-6	OC3-7	Average	OC1-1	OC1-1A	OC1-2	OC1-4	OC1-7	OC1-8	OC1-9
SiO_2	70.2	57.3	37.9	55.1	37.2	2.3	56.6	52.5	40.6	59.6	<0.1
Al_2O_3	9.25	14.06	10.1	11.14	31.10	36.47	23.81	16.52	22.45	22.78	<0.01
ΣFe_2O_3	3.49	2.08	2.53	2.7	0.38	0.34	3.16	5.8	0.08	1.59	<0.01
MgO	0.8	0.58	22.21	7.86	0.22	0.19	0.6	2.24	0.2	0.75	32.91
CaO	0.15	0.1	1.18	0.48	0.15	0.02	0.97	2.64	0.03	0.72	<0.01
Na_2O	0.76	0.54	1.4	0.9	0.94	3.50	0.03	0.63	0.96	0.1	<0.01
K_2O	3.03	4.24	1.55	2.94	2.60	5.13	0.33	0.97	4.41	0.49	<0.01
MnO	0.04	0.02	0.43	0.16	<0.01	<0.01	0.02	0.04	<0.01	0.01	<0.01
TiO_2	0.56	0.4	0.29	0.42	0.29	0.01	0.7	0.67	0.52	0.44	<0.01
P_2O_5	0.25	0.43	0.07	0.25	0.27	0.45	0.08	0.07	0.27	0.08	<0.01
Cr_2O_3	0.014	0.011	0.009	0.011	0.002	0.006	0.005	0.009	0.005	0.002	0.003
LOI	11.45	19.75	20.99	17.4	26.57	43.04	14.56	18.11	29.64	14.04	21.02
Total	100.17	99.76	98.81	99.58	99.84	91.63	100.88	100.23	99.26	100.63	53.96
TOT/C	0.32	0.13	4.31	1.59	0.05	0.07	0.02	0.03	0.02	0.02	<0.02
TOT/S	1.81	4.97	<0.02	2.26	5.48	14.15	0.13	0.03	8.05	0.08	18.03
SO_3	0.112	0.454	1.762	0.776	0.157	6.750	0.003	0.41	0.679	0.028	42.662
V_2O_5	0.018	0.012	0.01	0.013	0.020	0.034	0.022	0.017	0.028	0.016	<0.002

Trace elements (ppm)											
Cu	<0.001	<0.001	<0.001	0.001	<0.001	<0.001	<0.001	<0.001	<0.001	<0.001	<0.001
Ni	0.003	0.001	0.003	0.002	<0.001	0.002	0.008	<0.001	<0.001	<0.001	<0.001
Pb	0.012	<0.001	<0.001	0.004	<0.001	0.006	<0.001	<0.001	<0.001	<0.001	<0.001
Sr	0.084	0.095	0.02	0.066	0.131	0.205	0.027	0.017	0.085	0.024	0.018
Zn	0.003	0.002	0.006	0.004	0.002	0.002	0.006	0.009	0.002	0.005	0.002
Ba	1563	2666	1184	1804	956	1726	157	216	576	273	<1
Be	<1	<1	<1	1	<1	<1	<1	2	<1	2	<1
Co	1.7	0.2	16.5	6.1	0.2	<0.2	1.5	12.1	<0.2	1.2	<0.2
Cs	14.7	28.3	26.4	23.1	15.9	1.9	29.7	17.9	21.4	49.4	<0.1
Ga	39.9	49.4	11.3	33.5	15.9	25.9	21.3	17.5	45.6	17.4	<0.5
Hf	7.2	4.9	3.9	5.3	1.5	<0.1	7	5.2	8.4	5.7	<0.1
Nb	15.8	11.3	8.7	11.9	4.3	0.2	17.9	12.2	26.1	13.6	<0.1
Rb	78.3	75	90.2	81.2	33.9	82.1	19	77.1	48.6	51.3	<0.1
Sn	1	<1	<1	1	<1	<1	3	1	2	1	<1
Sr	861.3	1005.3	216	694.2	1381	2236	277.9	156.5	884.8	195.3	228.5
Ta	1.1	0.9	0.5	0.8	0.2	<1	1.1	0.7	1.5	1.1	<0.1
Th	57.5	32.8	12.9	34.4	24.0	34.1	17.4	15.8	20.5	20.1	0.8
U	4.6	2.9	2.3	3.3	1.9	0.6	1.5	1.4	5	3.3	<0.1
V	95	71	57	74	114	208	115	97	162	93	<8
W	2.2	1.4	1.7	1.8	1.2	0.7	2.2	2.3	1.3	1.6	<0.5
Zr	290.5	192.8	160.8	214.7	60.3	2.4	281.5	209.9	309.1	223.5	0.3
Y	13.4	8.6	13.4	11.8	4.3	3.7	12.9	25.3	3.2	15.1	<0.1
La	58.3	81.7	23.5	54.5	83.4	145.7	31.5	32.6	49.7	31.1	3.4
Ce	81.6	127.4	45.3	84.8	111.0	170.4	55.6	56	75.9	53	5.3
Pr	7.29	13.27	4.26	8.27	7.35	11.69	5.22	6.4	6.89	5.71	0.45
Nd	22.5	39.5	12.6	74.6	15.8	26.9	15.7	23.4	22.8	20.1	1.6
Sm	3.26	3.67	2.38	3.1	1.42	2.08	2.22	4.47	3.64	2.96	0.24
Eu	0.44	0.46	0.52	0.47	0.30	0.35	0.41	1.07	0.61	0.57	0.04
Gd	2.28	1.63	2.13	2.01	1.45	1.45	1.8	4.75	1.26	2.22	0.08
Tb	0.37	0.26	0.35	0.33	0.24	0.22	0.33	0.72	0.13	0.39	<0.01
Dy	2.25	1.71	1.98	1.98	1.13	1.01	1.83	4.03	0.56	2.45	0.05
Ho	0.52	0.32	0.46	0.43	0.19	0.20	0.47	0.91	0.1	0.58	<0.02
Er	1.47	0.94	1.48	1.3	0.51	0.45	1.5	2.9	0.34	1.77	<0.03
Tm	0.23	0.14	0.24	0.2	0.06	0.04	0.23	0.4	0.08	0.27	<0.01
Yb	1.72	1.07	1.54	1.44	0.41	0.27	1.77	2.42	0.62	1.97	<0.05
Lu	0.3	0.21	0.29	0.27	0.07	0.05	0.31	0.48	0.11	0.34	<0.01
Mo	1.2	0.6	0.7	0.8	<0.1	<0.1	0.1	<0.1	<0.1	0.4	<0.1
Cu	2.7	1.1	5.3	3.0	1.6	0.4	5.3	8.6	<0.1	1.1	<0.1
Pb	99.9	0.7	7.6	36.1	12.0	11.3	3.1	8.4	2.7	10	0.2
Zn	3	<1	15	6.33	1	<1	7	28	<0.1	5	2
Ni	21.5	11.8	17.3	16.9	0.5	0.5	1.4	11.9	0.2	2.9	0.3
As	45	6.9	20.4	24.1	3.5	3.5	7.9	3.2	2.4	12.2	<0.5
Cd	<0.1	<0.1	0.1	0.1	<0.1	<0.1	<0.1	<0.1	<0.1	<0.1	<0.1
Sb	<0.1	<0.1	<0.1	0.1	<0.1	<0.1	<0.1	<0.1	<0.1	0.2	<0.1
Bi	<0.1	<0.1	<0.1	0.1	<0.1	<0.1	0.2	0.3	<0.1	<0.1	<0.1
Ag	<0.1	<0.1	<0.1	0.1	<0.1	<0.1	<0.1	<0.1	<0.1	<0.1	<0.1
Au (ppb)	1.9	1.6	4.5	2.7	2.3	1.6	2.4	2.1	1.9	1.2	2
Hg	0.11	0.06	0.03	0.07	1.09	0.36	7.54	0.03	1.31	1.32	9.55
Ti	<0.1	<1	0.2	0.13	<0.1	<0.1	<0.1	0.2	<0.1	<0.1	<0.1
Se	<0.5	<0.5	<0.5	0.5	<0.5	<0.5	<0.5	<0.5	<0.5	<0.5	<0.5

Table 3 *contd*.

Major oxides (wt.%)	Altered tuff										
	OC2-1	OC2-7	OC2-8	OC2-9	OC2-12	OC2-13	OC2-15	OC3-2	OC3-4	OC3-8	Average
SiO_2	60.4	49.6	17.7	25.4	37	94.1	96.8	23.2	48.4	26	39.3
Al_2O_3	21.9	20.73	29.99	24.79	11.44	0.58	0.1	28.96	19.37	0.25	23.87
ΣFe_2O_3	1.12	4.14	0.15	6.06	28.77	0.13	0.2	1.62	8.08	1.21	4.71
MgO	0.23	0.3	0.26	0.25	0.25	0.18	0.11	0.54	2.5	30.48	0.66
CaO	0.15	0.24	0.02	0.03	0.02	0.01	0.02	0.07	2.05	8.08	0.55
Na_2O	0.56	0.73	2.21	1.19	0.23	0.02	0.07	1.86	0.52	<0.01	1.04
K_2O	0.82	2.13	5.36	5.24	2.73	0.06	<0.01	4.44	0.36	<0.01	2.69
MnO	<0.01	0.01	<0.01	<0.01	<0.01	<0.01	<0.01	<0.01	0.09	0.14	0.03
TiO_2	0.46	0.33	0.61	0.53	0.61	0.74	0.34	0.16	0.82	0.02	0.47
P_2O_5	0.1	0.13	0.87	0.82	0.89	0.03	<0.01	0.15	0.05	<0.01	0.33
Cr_2O_3	0.001	0.003	0.01	0.014	0.013	0.004	0.057	0.004	0.007	0.018	0.006
LOI	15.09	21.36	37.86	33.99	17.33	4.27	2.99	35.87	18.49	31.98	25.07
Total	100.86	99.78	95.39	98.52	99.61	100.14	100.78	97.03	100.75	98.18	98.8
TOT/C	0.03	0.02	0.1	0.09	0.06	0.02	0.03	0.16	0.06	8.85	0.06
TOT/S	1.79	3.99	11.99	9.91	4.66	0.09	0.05	10.23	0.06	0.03	5.43
SO_3	0.057	0.507	3.811	1.251	0.205	0.072	0.064	1.197	0.097	1.771	1.166
V_2O_5	0.005	0.02	0.034	0.049	0.068	0.004	0.004	0.023	0.031	0.004	0.028
Trace elements (ppm)											
Cu	<0.001	<0.001	<0.001	<0.001	<0.001	<0.001	<0.001	<0.001	0.002	<0.001	0.001
Ni	<0.001	<0.001	<0.001	<0.001	<0.001	<0.001	0.017	<0.001	0.004	0.004	0.005
Pb	<0.001	<0.001	0.007	0.004	0.013	<0.001	<0.001	<0.001	<0.001	<0.001	0.003
Sr	0.018	0.049	0.394	0.381	0.321	0.013	<0.002	0.09	0.011	0.002	0.135
Zn	0.001	0.003	0.002	0.002	0.003	0.003	0.003	0.002	0.008	0.002	0.004
Ba	511	614	3402	1887	3128	536	1705	961	349	64	1135
Be	<1	<1	1	1	1	<1	<1	<1	<1	1	1
Co	<0.2	0.7	0.2	<0.2	<0.2	<0.2	1.4	<0.2	19.9	2.9	2.84
Cs	39.3	25.8	20.3	16.8	36.3	17.2	1.2	13.4	3.3	<0.1	22.4
Ga	15.1	15.3	135.7	120.6	128.1	1.9	<0.5	17	19.1	<0.5	45.7
Hf	6.2	3.7	9.7	5.8	7.5	10.9	8.2	2.1	3.2	<0.1	5.5
Nb	12.7	9.1	17.8	12.4	17	25.1	8.8	4.5	5.7	<0.1	11.8
Rb	46.1	49.5	155	59.8	23.7	2.1	0.3	97.4	19.1	0.4	58.7
Sn	1	1	3	2	2	1	2	<1	1	<1	2
Sr	241.8	534.5	4044.8	4012.6	3292.9	71.9	12.6	942.9	109.2	37.9	1408.5
Ta	1.1	0.7	0.7	0.9	1.1	1.9	0.7	0.3	0.4	<0.1	0.8
Th	11.3	12.1	232.8	121.8	54.5	5.7	1.7	11.9	6	0.2	44.8
U	1.2	1.1	2.9	2.8	3	1.8	1	0.9	1	0.3	2.0
V	33	113	213	316	413	28	11	126	183	21	168
W	1.6	1.1	31.3	27.7	44	35.8	3.2	1	1.7	0.9	9.1
Zr	256.9	158	509.1	249.6	242.2	440.7	286.1	83.6	108.5	0.8	207.3
Y	2.7	2.5	5.6	5.8	8.6	7.1	1.7	2.2	18.6	3.1	8.5
La	20.6	36.5	456.7	385.6	376.8	22.8	1	30.5	14.4	1.9	130.4
Ce	36.5	68.5	439.2	321.5	451.7	19.8	1.3	47.1	44.2	3.9	148.5
Pr	4.52	5.87	35.92	25.52	36.86	2.16	0.11	3.54	3.61	0.53	12.24
Nd	11.8	11.5	88.2	76.2	91.2	6	<0.3	9	13.2	2.7	32.8
Sm	0.69	0.52	9.65	8	8.82	0.57	<0.05	0.72	3.01	0.5	3.71
Eu	0.08	0.05	1.89	1.3	1.62	0.12	<0.02	0.07	0.8	0.11	0.70
Gd	0.44	0.32	5.49	3.99	5.25	0.59	0.13	0.37	3.19	0.5	2.46
Tb	0.06	0.05	0.51	0.36	0.49	0.12	0.02	0.06	0.57	0.07	0.32
Dy	0.27	0.35	1.73	1.14	1.99	1.04	0.17	0.37	3.4	0.41	1.56
Ho	0.1	0.08	0.25	0.2	0.3	0.23	0.05	0.06	0.76	0.07	0.32
Er	0.28	0.27	0.58	1.49	0.93	0.97	0.21	0.26	2.26	0.22	1.04
Tm	0.06	0.04	0.11	0.13	0.13	0.15	0.02	0.04	0.36	0.03	0.15
Yb	0.54	0.44	0.99	0.95	1.07	1.22	0.25	0.31	2.54	0.17	1.10
Lu	0.09	0.06	0.17	0.16	0.16	0.23	0.06	0.06	0.38	0.02	0.19
Mo	0.3	0.5	0.2	8.2	6.5	0.2	4.8	0.3	<0.1	2.9	1.30
Cu	0.7	1.1	2.7	3.7	2	0.2	5.4	1.4	25.5	3.8	4.17
Pb	1.8	2.5	11.4	4.6	11.2	4.3	3.5	2.3	5.9	0.2	6.7
Zn	<1	2	1	2	<1	<1	<1	1	33	9	6.46
Ni	<0.1	0.3	4.1	6	2	1.6	151	1.3	9.6	66.2	3.14
As	1	26.7	34.6	229.7	459.5	6.8	<0.5	18.1	3.7	5.8	62
Cd	<0.1	<0.1	<0.1	<0.1	<1	<0.1	<0.1	<0.1	<0.1	<0.1	0.1
Sb	<0.1	<0.1	0.6	18	19.3	1.5	0.1	<0.1	0.1	0.6	2.9
Bi	<0.1	<0.1	<0.1	<0.1	1.2	0.4	<0.1	<0.1	0.1	<0.1	0.2
Ag	<0.1	<0.1	<0.1	<0.1	<0.1	<0.1	<0.1	<0.1	<0.1	<0.1	0.1
Au (ppb)	1	1.1	1.2	2.3	1.2	1	<0.5	1.2	3.6	2	1.8
Hg	0.05	0.04	4.85	2.61	2.97	0.22	10.98	1.08	0.08	0.4	1.79
Ti	<0.1	<0.1	0.3	0.3	1.2	0.3	<0.1	<0.1	<0.1	0.9	0.1
Se	<0.5	<0.5	<0.5	<0.5	0.8	<0.5	<0.5	<0.5	<0.5	<0.5	0.5

Table 4. Mass gain and loss for the samples based on the composition (ppm) of average fresh composition and constant Zr.

Major oxides (wt.%)	Fresh tuff	Altered tuff	RC	ΔC_i
SiO_2	55.1	42.8	45.64	−9.46
Al_2O_3	11.14	18.3	25.46	14.32
ΣFe_2O_3	2.7	3.7	3.95	1.25
MgO	7.86	4.25	4.53	−3.33
CaO	0.48	0.9	0.96	0.48
Na_2O	0.9	0.8	0.85	−0.05
K_2O	2.94	2.1	2.24	−0.5
MnO	0.16	0.03	0.03	−0.13
TiO_2	0.42	0.43	0.46	0.04
P_2O_5	0.25	0.25	0.27	0.02
Cr_2O_3	0.011	0.009	0.009	−0.002
LOI	17.4	27.72	29.56	12.16
Total	99.58	96.32	102.72	3.14
TOT/C	1.59	0.57	0.61	−0.98
TOT/S	2.26	5.22	5.57	3.31
SO_3	0.776	3.51	3.74	2.96
V_2O_5	0.013	0.02	0.02	0.007
Trace elements (ppm)				
Cu	0.001	0.001	0.001	0
Ni	0.002	0.002	0.002	0
Pb	0.004	0.003	0.003	−0.001
Sr	0.066	0.11	0.11	0.044
Zn	0.004	0.003	0.003	−0.001
Ba	1804	1003.6	1070.3	−733.7
Be	1	1.12	1.19	0.19
Co	6.1	2.45	2.61	−3.49
Cs	23.1	18.24	19.41	−3.69
Ga	33.5	35.2	37.54	4.04
Hf	5.3	5.02	5.35	0.05
Nb	11.9	11.04	5.71	−6.19
Rb	81.2	45.03	48.02	−33.18
Sn	1	1.47	1.57	0.57
Sr	694.2	1097.7	1170.7	476.5
Ta	0.8	0.8	0.83	0.03
Th	34.4	34.75	37.1	2.7
U	3.3	1.75	1.87	−1.43
V	74	132.59	141.4	67.4
W	1.8	9.3	9.92	8.12
Zr	214.7	201.32	214.7	0
Y	11.8	7.21	7.69	−4.11
La	54.5	101.42	108.16	53.66
Ce	84.8	115.35	123.01	38.21
Pr	8.27	9.95	10.61	2.34
Nd	74.6	25.7	27.4	−47.2
Sm	3.1	2.92	3.11	0.01
Eu	0.47	0.55	0.59	0.12
Gd	2.01	1.96	2.12	0.11
Tb	0.33	0.26	0.28	−0.05
Dy	1.98	1.29	1.38	−0.6
Ho	0.43	0.27	0.29	−0.14
Er	1.3	0.9	0.96	−0.34
Tm	0.2	0.13	0.14	−0.06
Yb	1.44	0.94	1	−0.44
Lu	0.27	0.16	0.17	−0.1
Mo	0.8	1.47	1.57	0.77
Cu	3.0	3.75	3.4	0.4
Pb	36.1	5.61	5.98	−30.12
Zn	6.33	5.65	6.03	−0.3
Ni	16.9	15.29	16.31	−0.59
As	24.1	48.21	51.41	27.31
Cd	0.1	0.15	0.16	0.06
Sb	0.1	2.43	2.59	2.49
Bi	0.1	0.2	0.2	0.1
Ag	0.1	0.1	0.1	0
Au (ppb)	2.7	1.68	1.79	−0.91
Hg	0.07	2.62	2.79	2.72
Ti	0.13	0.26	0.28	0.15
Se	0.5	0.52	0.55	0.05

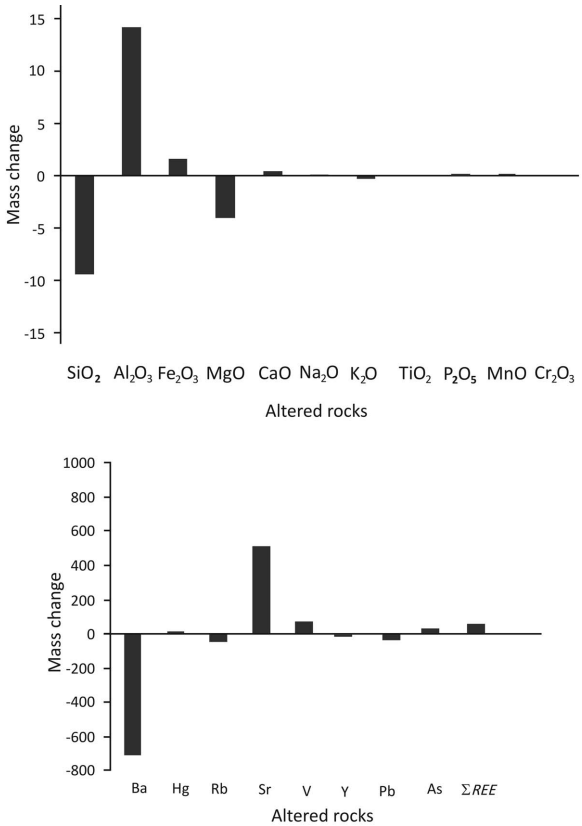

Figure 10. Mass change of the major elements (g/100 g) and trace elements (ppm/100 g) within the study area.

range from −150.09‰ to −123.61‰, and from −4.33‰ to −0.66‰, respectively. These isotopic data fall close to the left side of the kaolinite line in equilibrium with the meteoric waters at temperatures of >100ºC.

The sulfur- and oxygen-isotopic compositions of alunite range from 6.0‰ to 9.4‰ and from 5.5‰ to 10.3‰, respectively. These compositions reflect the involvement of steam-derived sulfur (Table 6; Figure 13; Hedenquist and Lowenstern, 1994; Rye, 2005).

DISCUSSION

The Güzelyurt kaolinite deposit of Aksaray is hosted by the Late Miocene Gördeles ignimbrite and consists of dacitic and andesitic tuffs. The kaolinite formed as a result of hydrothermal activity that developed along an active tectonic fault trending in a NE−SW direction. Lateral and vertical mineralogical zonation is characterized by a gradual transition from an inner kaolinite + alunite ± 7 Å halloysite zone outward to a smectite zone with increase of native sulfur and cinnabar-bearing alunite + 7 Å halloysite, and a porous silica zone upward through the sequences of kaolinite deposits. Fe-(oxyhydr)oxide phases associated with native sulfur and cinnabar demonstrate that multiple hydrothermal-alteration processes resulted in kaolinization and alunitization of the deposit. This inference is also supported by concentrations of Fe_2O_3 (max. 28.77%), SO_3 (max. 42.66%), Hg (max. 10.98 ppm), Ba (max. 3402 ppm), and Sr (max. 4045 ppm) in the altered volcanic units, which are similar to those reported by Nagasawa (1978) and Inoue (1995). The degradation of Fe-bearing hornblende and biotite results in iron oxidation which was found through petrographic determinations.

On the basis of textural and chemical analyses, argillization of feldspar and Fe-(oxyhydr)oxidation of hornblende and mica in the poorly welded, permeable, altered volcanic units are caused by an open hydrologic system. Thus, advanced alteration of feldspar, hornblende, biotite, and volcanic glass in the andesitic rocks resulted in an increase in the (Al ± Fe)/Si ratio and the leaching of alkali elements, which favors the precipitation of kaolinite or 7 Å halloysite under acidic

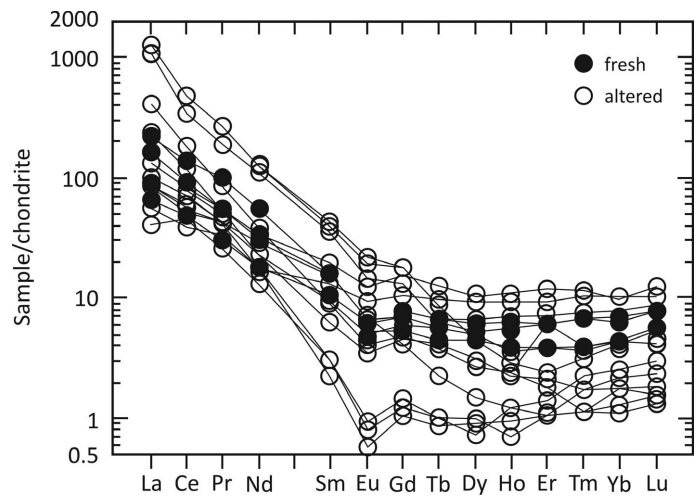

Figure 11. Chondrite-normalized *REE* patterns (Boynton, 1984) for fresh and altered samples from the study area.

Table 5. Oxygen and hydrogen isotopic compositions of kaolinite, 7 Å halloysite, smectite, and kaolinite+smectite from the Güzelyurt kaolinite deposit.

Sample ID	Mineralogy	Weight (mg)	%H	Normalized δ^2H *vs.* VSMOW	%O	Normalized $\delta^{18}O$ *vs.* VSMOW
OC1-15	7 Å halloysite	0.755	0.42	–115.55	5.06	2.32
OC2-1	kaolinite	0.810	1.18	–106.05	13.09	0.84
OC2-2	7 Å halloysite	0.777	2.53	–101.81	42.20	7.64
OC1-2	kaolinite	0.789	1.22	–132.92	10.41	0.56
OC1-3	smectite	0.848	1.02	–136.91	8.30	–0.86
OC1-4	smectite	0.796	0.94	–123.61	7.97	–1.87
OC1-8	kaolinite+smectite	0.820	1.08	–130.49	9.55	–0.66
OC2-5	smectite	0.809	1.42	–150.09	11.83	–4.33

environmental conditions (Figure 14; Nagasawa, 1978; Meunier, 1995; Inoue, 1995; Kadir and Karakaş, 2002; Kadir *et al*., 2008).

The relative increase of the K/(Ca + Na) ratio and S (along with Al) resulted in the precipitation of authigenic alunite, with/without 7 Å halloysite, under acidic environmental conditions, similar to case studies in western Anatolia (Mutlu *et al*., 2005; Sayın, 2007; Ece and Schroeder, 2007; Ece *et al*., 2008). The relative increase in the S-H-bearing steam upward of the volcanic units resulted in an increase in the amount of alunite and 7 Å halloysite, rather than of kaolinite. This increase in the middle and upper parts of the deposit is controlled by hydrothermal processes at or above the water table by the oxidation of H_2S, with a relative increase in porosity and permeability upward of the volcanic units.

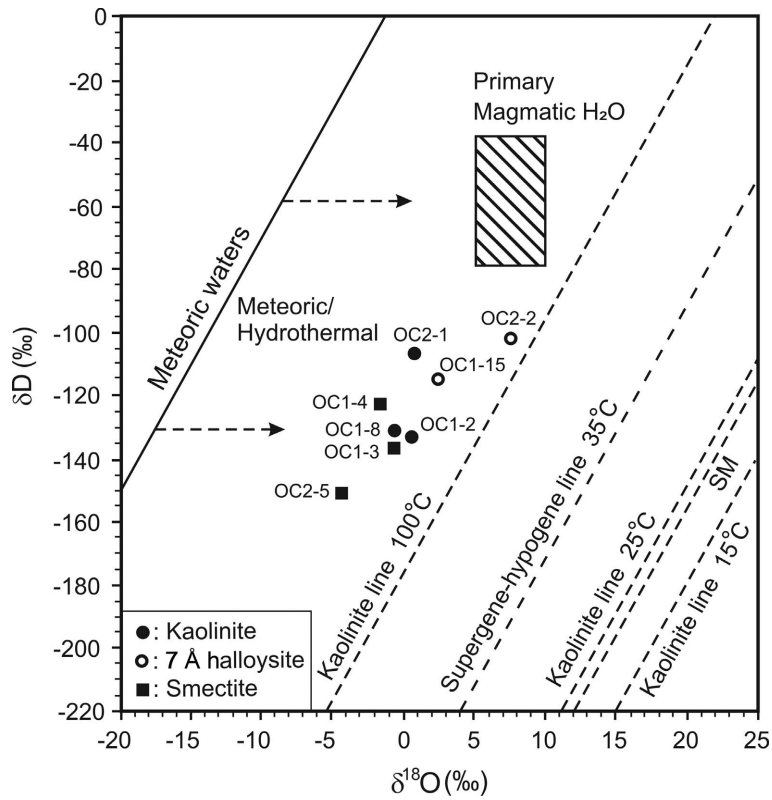

Figure 12. δD *vs*. $\delta^{18}O$ plot showing isotopic compositions of kaolinite, 7 Å halloysite, smectite, and kaolinite + smectite from the Güzelyurt kaolinite deposit (Sheppard, 1986). The kaolinite line in equilibrium with meteoric water at temperatures of 100ºC is from Hayba *et al*. (1985); those at 25ºC and 15ºC are from Sheppard and Gilg (1996). The supergene/hypogene line of kaolinite equilibrium with meteoric water at 35ºC is from Sheppard *et al.* (1969). The smectite line (SM) representing the isotopic composition in equilibrium with meteoric water at 20ºC is from Savin and Epstein (1970). The meteoric water line is from Craig (1961).

Table 6. Oxygen and sulfur isotopic compositions of alunite samples from the Güzelyurt kaolinite deposit.

Sample	Mineralogy	$\delta^{34}S$ (‰)	$\delta^{18}O$ (‰)
OC1-1A	alunite	7.5	5.5
OC1-7	alunite	9.4	6.0
OC2-8	alunite	6.4	9.9
OC2-9	alunite	7.5	9.1
OC2-10	alunite	7.5	10.3
OC2-11	alunite	6.5	8.6
OC2-12	alunite	6.0	7.0

The concentration of released and depleted Mg, Si, Na, and Ca outward in the kaolinite deposit favored precipitation of smectite under alkaline micro-environmental conditions (Berner and Berner, 1996). Local concentrations of S- and Hg-bearing hydrothermal solutions caused the precipitation of native sulfur and cinnabar crystals in a reducing environment associated mainly with alunite or alunite/7 Å halloysite (Ece *et al*., 2013). The depletion of excess silica during alteration under low pressure and temperature and at neutral conditions occurred during hydrothermal fluid and steam flushing, and exhalations that happened close to the surface resulted in the development of a porous silica cap consisting of quartz and opal-CT (Ehrenberg, 1991; Rye *et al*., 1992; Herdianita *et al*., 2000; Meunier and Velde, 2004; Ece *et al*., 2013).

Micromorphologically, the occurrence of kaolinite as stacks in book-like form, the coexistence of 7 Å halloysite rods with alunite, and the development of subparallel orientation along fracture surfaces may reveal *in situ* dissolution and precipitation caused by hydrothermal-fluid flushing. The coexistence of trace gypsum with opal-CT in sample OC2-15 may be due to local increases in Ca and S that were brought about by siliceous hydrothermal-fluid injections. The sharp basal peaks and the reflections of non-basal doublets and triplets, euhedral hexagonal kaolinite, rod-like 7 Å halloysite identified by SEM and TEM, ideal DTA-TG curves, SiO_2/Al_2O_3 and SiO_2/R_2O_3 ratios (1.21 and 1.16; and 1.22 and 1.15), and chemical index of alteration (CIA) values between 94.23 and 97.30 in purified kaolinite and 7 Å halloysite samples suggest well crystallized kaolinite and 7 Å halloysite (Nesbitt and Markovics, 1997; Kadir and Karakaş, 2002; Sousa *et al.*, 2007).

Several different phases of hydrothermal activity in the study area caused changes in the reddish-brown coloration within the smectite-dominated altered volca-

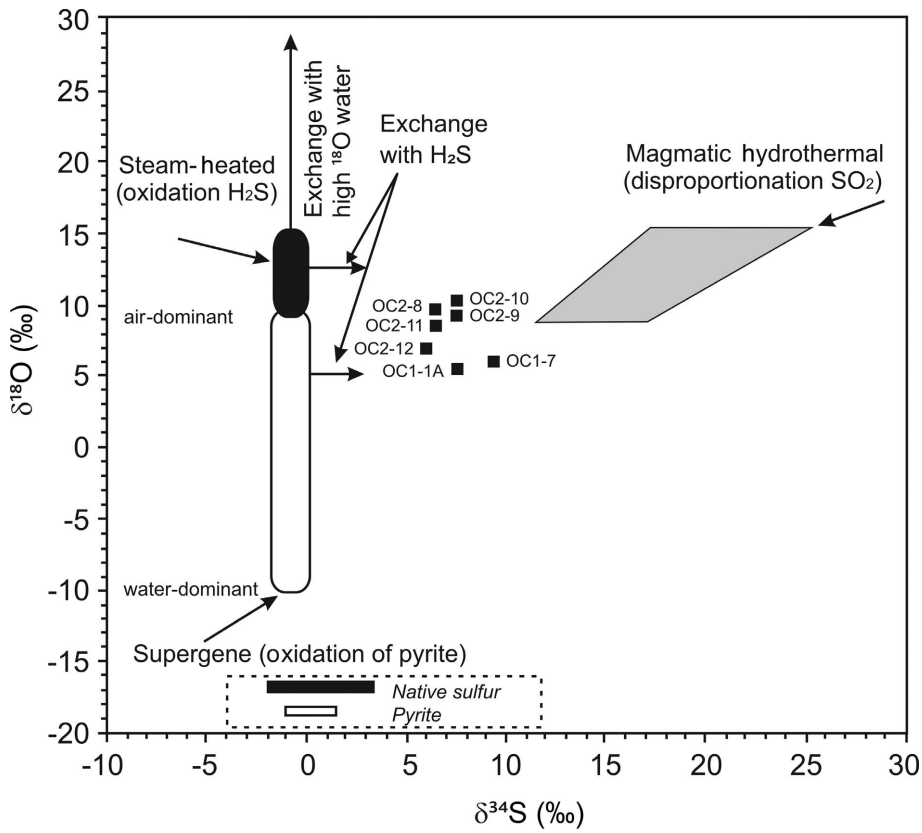

Figure 13. $\delta^{34}S$ *vs.* $\delta^{18}O$ plot showing isotopic compositions of alunite samples from the Güzelyurt kaolinite deposit (modified from Hedenquist and Lowenstern, 1994; Rye, 2005).

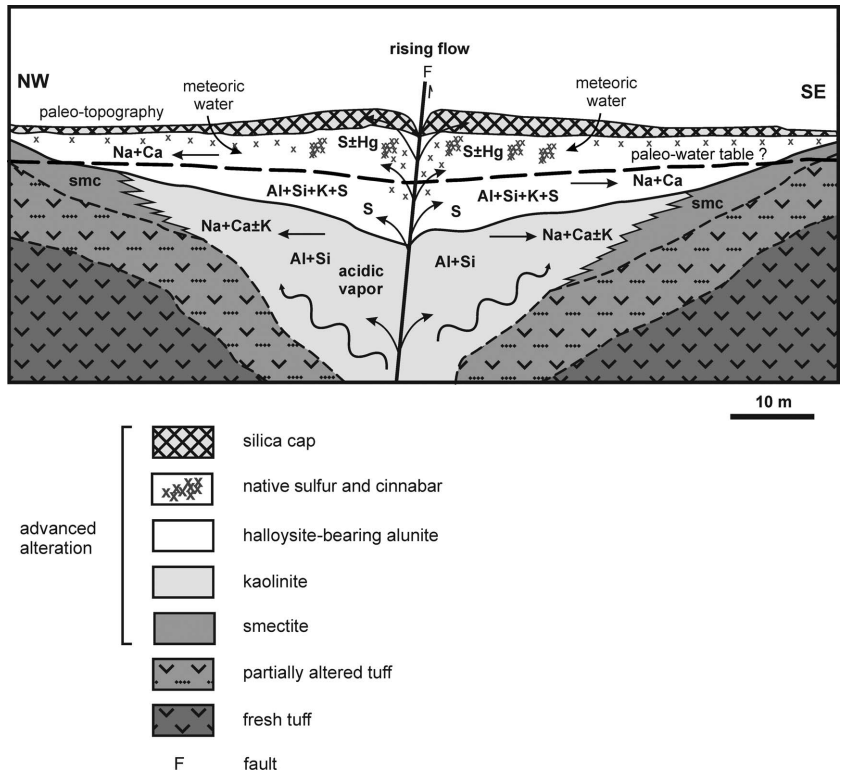

Figure 14. Genetic model for the Güzelyurt kaolinite deposit.

nites. The reddish-brown coloration was caused by Fe-(oxyhydr)oxide (Velde, 1985; Meunier, 2005).

The depletion of Si + Mg + K and Ba + Rb, the enhancement of Sr, the enrichment of *LREE*s relative to the *HREE*s, and the negative Eu anomalies reveal that the fractionation during alteration of plagioclase and hornblende and the devitrification of volcanic glass originated from dacitic and andesitic tuffs and basaltic lava during hydrothermal alteration processes and were the main sources of the kaolinite, 7 Å halloysite, and alunite formation (Rollinson, 1993).

The plot of δD and $\delta^{18}O$ values for the kaolinite + 7 Å halloysite fraction was between the equilibrium lines of kaolinite with meteoric water at 100ºC and with meteoric and primary magmatic water, but was near the equilibrium line of kaolinite with meteoric water at 100ºC; this may indicate a steam-heated environment at temperatures above 100ºC (Hayba *et al*., 1985; Ece *et al*., 2008, 2013). The isotopic data for kaolinite and 7 Å halloysite samples shifted to higher δD and $\delta^{18}O$ values, which were near the magmatic box compared with the smectitic samples; they may have been controlled by hydrothermal temperature changes and the degree of fractionation between the liquid and the vapor during the kaolinization and alunitization processes (Faure, 1986). A slight enrichment in the δD and $\delta^{18}O$ values of 7 Å halloysite from −115.55‰ to −101.81‰ and from 2.32‰ to 7.64‰, respectively, relative to kaolinite, which ranges from −132.92‰ to −106.05‰ and from 0.56‰ to 0.84‰, respectively, suggests the formation of kaolinite from steam-heated magmatic fluid and the formation of 7 Å halloysite ± kaolinite from the mixing of steam and meteoric water due to the exchange between the two fluids or evaporation (Gilg *et al*., 2003; Bethke *et al*., 2005; Deyell *et al*., 2005; Ece *et al*., 2013). Thus, the influence of meteoric water or the evaporation rate increase upward through the vertical sequences of the kaolinite deposit. This interpretation is also supported by the association of fine-grained alunite with 7 Å halloysite and the development of a porous silica cap at the uppermost layer of the kaolinite deposit (Deyell and Dipple, 2005; Rye, 2005). Lee *et al.* (2014) also noted that the high-sulfidation hydrothermal system of Seongsan (South Korea) exhibits similar enrichment, which is caused by the mixing of meteoric water with hydrothermal water.

Moreover, the positive $\delta^{34}S$ and $\delta^{18}O$ compositions of alunite, $\delta^{34}S$ values ranging between +6.0‰ and +9.4‰, and the fine grain sizes of alunite (<7 μm) reflect the involvement of steam-derived sulfur under temperatures of ~70−180ºC and pressures of 1−12 atm unlike that of magmatic steam which shows smaller $\delta^{34}S$ values (between +3.9 and +2.7), coarser grain sizes (>50 μm) and higher temperatures (200−300ºC) (Rye *et al*., 1992; Rye, 2005; Deyell and Dipple, 2005; Lerouge *et al*., 2006; Georgieva and Velinova, 2012). This

suggestion was also supported by the absence of pyrite, dickite, and pyrophyllite in association with alunite which might be expected at higher temperatures (200−340ºC) (Deyell and Dipple, 2005).

CONCLUSION

The Güzelyurt kaolinite deposit was formed by the hydrothermal alteration of dacitic and andesitic tuffs and basaltic lavas and was controlled by tectonic activity. These alteration processes resulted in a mineralogical zonation outward from the main kaolinite deposit. This outward zonation is: kaolinite + alunite ± 7 Å halloysite, smectite, the occurrence of a silica cap (opal-CT, quartz), and Fe-(oxyhydr)oxide phases associated with native sulfur and cinnabar above the deposit. This demonstrates that the kaolinization and alunitization were the result of multiple hydrothermal-alteration processes. The occurrence of kaolinite below, and alunite + 7 Å halloysite associated with native sulfur and cinnabar in the middle and above, the deposit suggests that alunite formed following the precipitation of kaolinite from a sulfur-rich hydrothermal fluid and under steam flushing and exhalative conditions. The increase in the (Al_2O_3 + Fe_2O_3 + K_2O)/SiO_2 ratio and the decrease in MgO + Na_2O + CaO along the fault zone also support the hydrothermal-zonation hypothesis. Micromorphologically, the development of platy and book-like kaolinite, the coexistence of rod-like 7 Å halloysite and cubic alunite with relicts of volcanogenic materials, the depletion of Si + Mg + K, Rb + Ba, the enrichment of S and Sr, the depletion of the *HREE* relative to the *LREE*, and a negative Eu anomaly suggest that these minerals formed from the alteration of feldspar, hornblende, and volcanic glass by a dissolution-precipitation mechanism under acidic environmental conditions in an open hydrologic system. A relative increase in the δD and $\delta^{18}O$ values of kaolinite and 7 Å halloysite above the deposit reflects the mixing of magmatic and meteoric waters and evaporation. The positive $\delta^{34}S$ and $\delta^{18}O$ isotope compositions of alunite with fine grain sizes suggest its formation under the influence of steam-derived sulfur from the oxidation of H_2S at or above the water table.

ACKNOWLEDGMENTS

This present study was supported financially by the Scientific Research Projects Fund of Eskişehir Osmangazi University in the framework of Project 201015030. The authors are indebted to Professor Warren D. Huff and an anonymous reviewer for their careful and constructive reviews that improved the quality of the paper significantly. The authors are also grateful to Associate Editor, Robert J. Pruett, Editors in Chief, Michael A. Velbel and Joseph W. Stucki, and Managing Editor, Kevin Murphy for their insightful editorial comments and suggestions. This paper was presented at the 50th Anniversary Annual Meeting of The Clay Minerals Society, University of Illinois at Urbana-Champaign, Illinois, USA.

REFERENCES

Arslan, M., Kadir, S., Abdioğlu, E., and Kolaylı, H. (2006) Origin and formation of kaolin minerals in saprolite of Tertiary alkaline volcanic rocks, Eastern Pontides, NE Turkey. *Clay Minerals*, **41**, 597−617.

Berner, E.K. and Berner, R.A. (1996) *Global Environment: Water, Air, and Geochemical Cycles*. Princeton University Press, New Jersey, USA, 376 pp.

Bethke, P.M., Rye, R.O., Stoffregen, R.E., and Vikre, P.G. (2005) Evolution of the magmatic-hydrothermal acid-sulfate system at Summitville, Colorado: integration of geological, stable-isotope, and fluid-inclusion evidence. *Chemical Geology*, **215**, 281−315.

Brindley, G.W. (1980) Quantitative X-ray analysis of clays. Pp. 411−438 in: *Crystal Structures of Clay Minerals and their X-ray Identification* (G.W. Brindley and G. Brown, editors). Monograph **5**, Mineralogical Society, London.

Boynton, W.V. (1984) Cosmochemistry of the rare earth elements: meteorite studies. Pp. 63−114 in: *Rare Earth Element Geochemistry* (P. Henderson, editor), Developments in Geochemistry. Elsevier, Amsterdam.

Chen, Y.C., Wang, M.K., and Yang, D.S. (2001) Mineralogy of dickite and nacrite from northern Taiwan. *Clays and Clay Minerals*, **49**, 586−595.

Clayton, R.N. and Mayeda, T.K. (1963) The use of bromine pentafluoride in the extraction of oxygen from oxides and silicates for isotopic analysis. *Geochimica et Cosmochimica Acta*, **27**, 43−52.

Craig, H. (1961) Isotopic variations in meteoric waters. *Science*, **133**, 1702−1703.

Deyell, C.L. and Dipple, G.M. (2005) Equilibrium mineral-fluid calculations and their application to the solid solution between alunite and natroalunite in the El Indio-Pascua belt of Chile and Argentina. *Chemical Geology*, **215**, 219−234.

Deyell, C.L., Rye, R.O., Landis, G.P., and Bissig, T. (2005) Alunite and the role of magmatic fluids in the Tambo high-sulfidation deposit, El Indio-Pascua belt, Chile. *Chemical Geology*, **215**, 185−218.

Dönmez, M., Akçay, A.E., Kara, H., Türkecan, A., and Yergök, F.A. (2005) *Geological map of Aksaray L32 Quadrangle, Scale 1:100.000.* General Directorate of Mineral Research and Exploration (MTA) Publications, Ankara.

Ece, Ö.İ. and Schroeder, P.A. (2007) Clay mineralogy and chemistry of halloysite and alunite deposits in the Turplu area, Balikesir, Turkey. *Clays and Clay Minerals*, **55**, 18−35.

Ece, Ö. İ., Schroeder, P.A., Smilley, M., and Wampler, M. (2008) Acid-sulfate alteration volcanic rocks and genesis of halloysite and alunite deposits in the Biga Peninsula, NW Turkey. *Clay Minerals*, **43**, 281−315.

Ece, Ö.İ., Ekinci, B., Schroeder, P.A., Crowe, D., and Esenli, F. (2013) Origin of the Düvertepe kaolin-alunite deposits in Simav Graben, Turkey: Timing and styles of hydrothermal mineralization. *Journal of Volcanology and Geothermal Research*, **255**, 57−18.

Ehrenberg, S.N. (1991) Kaolinized, potassium-leached zones at the contacts of the Garn Formation, Haltenbanken, mid-Norwegian continental shelf. *Marine and Petroleum Geology*, **8**, 250−269.

Erkoyun, H. and Kadir, S. (2011) Mineralogy, micromorphology, geochemistry and genesis of a hydrothermal kaolinite deposit and altered Miocene host volcanites in the Hallaçlar area, Uşak, western Turkey. *Clay Minerals*, **46**, 421−448.

Faure, G. (1986) *Principles of Isotope Geology*, 2nd edition, John Wiley and Sons, New York, 589 pp.

Fujii, N., Kayabalı, İ., and Saka, A.H. (1995) *Data Book of Ceramic Raw Materials of Selected Areas in Turkey*.

Monograph Series No.**1**, General Directorate of Mineral Research and Exploration, Ankara, 144 pp.

Georgieva, S. and Velinova, N. (2012) Alunite from the advanced argillic alterations in the Chelopech high-sulphidation epithermal Cu-Au deposit, Bulgaria: Chemistry, morphology and genetic significance. *Geochemistry, Mineralogy and Petrology*, **49**, 17–31.

Gilg, H.A., Weber, B., Kasbohm, J., and Frei, R. (2003) Isotope geochemistry and origin of illite-smectite and kaolinite from the Seiltz and Kemmlitz kaolin deposits, Saxony, Germany. *Clay Minerals*, **38**, 95–112.

Hayba, D.O., Bethke, P.M., Heald, P., and Faley, N.K. (1985) Geologic, mineralogic and geochemical characteristics of volcanic-hosted epithermal precious-metal deposits. *Reviews in Economic Geology*, **2**, 129–167.

Hedenquist, J.W. and Lowenstern, J.B. (1994) The role of magmas in the formation of hydrothermal ore deposits. *Nature*, **370**, 519–527.

Herdianita, N.R., Browne, P.R.L., Rodgers, K.A., and Campbell, K.A. (2000) Mineralogical and textural changes accompanying ageing of silica sinter. *Mineralium Deposita*, **35**, 48–62.

Hosono, T., Lorphensriand, O., Onodera, S-i, Okawa, H., Nakano, T., Yamanaka, T., Tsujimura, M., and Taniguchi, M. (2014) Different isotopic evolutionary trends of $\delta^{34}S$ and $\delta^{18}O$ compositions of dissolved sulfate in an anerobic deltaic aquifer system. *Applied Geochemistry*, **46**, 30–42.

Imai, N., Otsuka, R., and Kashide, H. (1969) Dehydration of palygorskite and sepiolite from the Kuzu District, Tochigi Pref., central Japan. Pp. 99–108 in: Proceedings, International Clay Conference, Tokyo.

Inoue, A. (1995) Formation of Clay Minerals in Hydrothermal Environments. Pp. 268–329 in: *Origin and Mineralogy of Clays* (B. Velde, editor), Springer-Verlag Berlin.

Jones, B.F. and Galán, E. (1988) Sepiolite and palygorskite. Pp. 631–674 in: *Hydrous Phyllosilicates (Exclusive of Micas)* (S.W. Bailey, editor). Reviews in Mineralogy, **19**, Mineralogical Society of America, Washington, D.C.

Jepson, W.B. and Rowse, J.B. (1975) The composition of kaolinite; an electron microscope microprobe study. *Clays and Clay Minerals*, **23**, 310–317.

Kadir, S. and Akbulut, A. (2009) Mineralogy, geochemistry and genesis of the Taşoluk kaolinite deposits in pre-Early Cambrian metamorphites and Neogene volcanites of Afyonkarahisar, Turkey. *Clay Minerals*, **44**, 89–112.

Kadir, S. and Erkoyun, E. (2013) Genesis of the hydrothermal Karaçayır kaolinite deposit in Miocene volcanics and Palaeozoic metamorphic rocks of the Uşak-Güre basin, Western Turkey. *Turkish Journal of Earth Sciences*, **22**, 444–468.

Kadir, S. and Karakaş, Z. (2002) Mineralogy, chemistry and origin of halloysite, kaolinite and smectite from Miocene ignimbrites, Konya, Turkey. *Neues Jahrbuch für Mineralogie, Abhandlungen*, **177**, 113–132.

Kadir, S., Önen-Hall, P., Aydin, S.N., Yakicier, C., Akarsu, N., and Tuncer, M. (2008) Environmental effect and genetic influence: a regional cancer predisposition survey in the Zonguldak region of northwest Turkey. *Environmental Geology*, **54**, 391–409.

Kadir, S., Erman, H., and Erkoyun, H. (2011) Mineralogical and geochemical characteristics and genesis of hydrothermal kaolinite deposits within Neogene volcanites, Kütahya (western Anatolia), Turkey. *Clays and Clay Minerals*, **59**, 250–276.

Küçüksille, N. (1979) Report on alunite-bearing kaolinite deposits at Güzelyurt, Niğde-Aksaray. MTA Report No. 6500, Ankara (in Turkish).

Lanson, B., Beaufort, D., Berger, G., Bauer, A., Cassagnabère, A., and Meunier, A. (2002) Authigenic kaolin and illitic minerals during burial diagenesis of sandstones: a review. *Clay Minerals*, **37**, 1–22.

Lee, G., Koh, S.M., and Pirajno, F.M. (2014) Evolution of hydrothermal fluids of HS and LS type epithermal Au-Ag deposits in the Seongsan hydrothermal system of the Cretaceous Haenam volcanic field, South Korea. *Ore Mineralogy Reviews*, **61**, 33–51.

Lerouge, C., Kunov, A., Fléhoc, C., Georgieva, S., Hikov, A., Lescuyer, J.K, Petrunov, R., and Velinova, N. (2006) Constraints of stable isotopes on the origin of alunite from advanced argillic alteration systems in Bulgaria. *Journal of Geochemical Exploration*, **90**, 166–182.

MacKenzie, R.C. (1957) *The Differential Thermal Investigation of Clays*. Monograph **2**, Mineralogical Society, London, 456 pp.

MacLean, W.H. and Kranidiotis, P. (1987) Immobile elements as monitors of mass transfer in hydrothermal alteration: Phelps Dodge massive sulfide deposits, Matagami, Quebec. *Economic Geology*, **2**, 951–962.

Meunier, A. (1995) Hydrothermal alteration by veins. Pp. 247–267 in: *Origin and Mineralogy of Clays, Clays and the Environment* (B. Velde, editor). Springer-Verlag, Berlin.

Meunier, A. (2005) *Clays*. Springer-Verlag, Berlin, Heidleberg, 472 pp.

Meunier, A. and Velde, B. (2004) *Illite: Origin, Evolution and Metamorphism*. Springer-Verlag, Berlin, Heidelberg, New York, 286 pp.

Moore, D.M. and Reynolds, R.C. (1989) *X-ray Diffraction and the Identification and Analysis of Clay Minerals*. Oxford University Press, New York, 332 pp.

Mutlu, H., Sarıiz, K., and Kadir, S. (2005) Geochemistry and origin of the Şaphane alunite deposit, Western Anatolia, Turkey. *Ore Geology Reviews*, **26**, 39–50.

Nagasawa, K. (1978) Kaolin minerals. Pp. 189–219 in: *Clays and Clay Minerals of Japan* (T. Sudo and S. Shimoda, editors). Developments in Sedimentology, **26**, Elsevier, Tokyo.

Nesbitt, H.W. and Markovics, G. (1997) Weathering of granidioritic crust, long-term storage of elements in weathering profiles and petrogenesis of siliciclastic sediments. *Geochimica et Cosmochimica Acta*, **61**, 1653–1670.

Njoya, A., Nkoumbou, C., Grosbois, C., Njopwouo, D., Njoya, D., Courtin-Nomade, A., Yvon, J., and Martin, F. (2006) Genesis of Mayouom kaolin deposit (western Cameroon). *Applied Clay Science*, **32**, 125–140.

Paterson, E. and Swaffield, R. (1987) Thermal analysis. Pp. 99–132 in: *A Handbook of Determinative Methods in Clay Mineralogy* (M.J. Wilson, editor). Blackie and Sons Limited, Glasgow, UK, 308 pp.

Rollinson, H.R. (1993) *Using Geochemical Data: Evaluation, Presentation, Interpretation*. John Wiley and Sons Inc., New York, 352 pp.

Rye, R.O. (2005) A review of the stable-isotope geochemistry of sulfate minerals in selected igneous environments and related hydrothermal systems. *Chemical Geology*, **215**, 5–36.

Rye, R.O., Bethke, P.M., and Wasserman, M.D. (1992) The stable isotope geochemistry of acid sulfate alteration. *Economic Geology*, **87**, 225–255.

Savin, S.M. and Epstein, S. (1970) The oxygen and hydrogen isotope geochemistry of clay minerals. *Geochimica et Cosmochimica Acta*, **34**, 25–42.

Sayın, Ş.A. (2007) Origin of kaolin deposits: evidence from the Hisarcık (Emet-Kütahya) deposits, western Turkey. *Turkish Journal of Earth Sciences*, **16**, 77–96.

Sheppard, S.M.F. (1986) Characterization and isotopic variations in natural waters. Pp. 141–162 in: *Stable Isotopes in High Temperature Geological Processes* (J.W. Valley, H.P. Taylor, and J.R. O'Neil, editors). Reviews in Mineralogy,

16, Mineralogical Society of America, Washington, D.C.

Sheppard, S.M.F. and Gilg, H.A. (1996) Stable isotope geochemisty of clay minerals. *Clay Minerals*, **31**, 1–24.

Sheppard, S.M.F., Nielsen, R.L., and Taylor, H.P. (1969) Oxygen and hydrogen isotope ratios of clay minerals from porphyry copper deposits. *Economic Geology*, **64**, 755–777.

Smykatz-Kloss, W. (1974) *Differential Thermal Analysis, Application and Results in Mineralogy*. Springer-Verlag, Berlin, 185 pp.

Sousa, D.J.L., Varajão, A.F.D.C., Yvon, J., and Da Costa, G.M. (2007) Mineralogical, micromorphological and geochemical evolution of the kaolin facies deposit from the Capim region (northern Brazil). *Clay Minerals*, **42**, 69–87.

Temel, A., Gençoğlu, H., Bayhan, H., Öner, F., and Ağrılı, H. (1995) Mekedere (Güzelyurt – Aksaray) kaolinit ocağının hidrotermal mineral oluşumları. *VII. Ulusal Kil Sempozyumu Bildiriler Kitabı*, s. 76–87.

Velde, B. (1985) *Clay Minerals. A Physico-Chemical Explanation of their Occurrence*. Development in Sedimentology, **40**, Elsevier, New York, 427 pp.

Wilson, M.J. (1987) X-ray powder diffraction methods. Pp. 26–98 in: *A Handbook of Determinative Methods in Clay Mineralogy* (M.J. Wilson, editor). Blackie & Sons, Glasgow and London.

Yuan, J. and Murray, H.H. (1993) Mineralogical and physical properties of the Maoming kaolin from Guangdong province, south China. Pp. 249–259 in: *Kaolin Genesis and Utilization* (H.H. Murray, W.M. Bundy, and C.C. Harvey, editors). The Clay Minerals Society, Boulder, Colorado, USA.

(*Received 19 February 2014; revised 26 December 2014; Ms. 851; AE: R.J. Pruett*)

Clays and Clay Minerals, Vol. 62, No. 6, 500–507, 2014.

ADSORPTION OF ORGANIC COMPOUNDS FOUND IN HUMAN SEBUM ON LATVIAN ILLITIC, KAOLINITIC, AND CHLORITIC PHYLLOSILICATES

AGNESE PURA, INGA DUSENKOVA*, AND JURIS MALERS

Institute of General Chemical Engineering, Riga Technical University, P. Valdena Street 3, Riga, LV-1048, Latvia

Abstract—Clays are used widely as facial masks to remove excess sebum, an oily substance released onto the skin. Smectite, illite, kaolinite, and in some cases, chlorite, are the dominant phyllosilicates in most commonly used clay facial masks. To date, the adsorption of human sebum has been proved only on smectite clays; in the present study the adsorption of two organic compounds found in human sebum by illitic, kaolinitic, and chloritic phyllosilicates was investigated. Illitic clays are often used in cosmetic clay masks, but usually contain some fine-grained non-clay minerals. The presence of carbonate, for example, can cause skin irritation because of its alkaline nature, and iron oxides and hydroxides reduce the adsorption properties of clays. The influence of the removal of these compounds on the adsorption properties of illitic clays was also investigated. The amounts of both compounds adsorbed were established by UV-VIS spectrophotometry. All samples were characterized by mineralogical composition, particle-size distribution, specific surface area, and cation exchange capacity (CEC). Oleic acid and squalene were adsorbed on all clay samples, but illitic and chloritic phyllosilicates showed the greatest adsorption capacity. After purification, the sizes of the particles decreased and the CEC values increased. Nevertheless, the dissolution of carbonates essentially had no influence on the adsorption properties, whereas the removal of iron oxides and hydroxides increased significantly the amounts adsorbed of both oleic acid and squalene.

Key Words—Adsorption, Carbonates, Clays, Iron oxides, Oleic Acid, Squalene.

INTRODUCTION

Clays and clay minerals are used widely in cosmetics, health-care, and therapeutic products as active ingredients and excipients (Lopez-Galindo and Viseras, 2004; Lopez-Galindo *et al*., 2007; Tateo and Summa, 2007; Veniale *et al*., 2007; Williams *et al.*, 2008; Carretero and Pozo, 2009, 2010). Clay minerals are understood to adsorb toxins and excess sebum from the skin surface due to the sorption properties of clay minerals and therefore are used as facial masks for treatment of skin inflammations and dermatological diseases such as acne, boils, ulcers and seborrhoea (Carretero, 2002; Williams *et al.*, 2008; Carretero *et al*., 2013). Sebum is an oily substance produced by sebaceous glands (located in the skin) and is a mixture of lipids composed mainly of triglycerides, wax esters, squalene, fatty acids, cholesterol, and cholesterol esters (Pappas *et al*., 2009; Schwartz *et al.*, 2012). Sebum is involved in the development of the epidermis, protection of the skin from ultraviolet radiation, and in the regulation of body odour (Schwartz *et al*., 2012). Increased sebum secretion on the face can lead to the development of several skin inflammations and diseases, one of them being acne (Thiboutot, 2004; Youn, 2010). Acne patients are known to have greater sebum secretion rates than those without acne (Harris *et al*., 1983; Zouboulis, 2004; Pappas *et al*., 2009) and their sebum contains higher levels of squalene (Pappas *et al*., 2009). Another sebum-induced skin disease is seborrheic dermatitis, caused mainly by increased levels of oleic acid (Schwartz *et al*., 2012).

Commercially available clays for therapeutic and beauty purposes contain one or usually more clay minerals. The most commonly used clays contain smectite, kaolinite, and/or illite, and sometimes also chlorite (Carretero, 2002; Zague *et al*., 2007; Vecstaudža *et al.*, 2012; Khiari *et al.*, 2014), but to the authors' knowledge, the adsorption of human sebum has been demonstrated only on smectite (montmorillonite) (Downing *et al.*, 1982). The adsorption of polar and non-polar organic compounds on clays depends on the type of clay mineral present (Greenland *et al*., 1965; Li and Gupta, 1994), *i.e*. on the crystal-chemical features of the clay (Johnston, 1996, 2010).

The application of certain clays can be improved by removal of some non-clay minerals. Cosmetic products used in health care should be slightly acidic, *i.e.* as close as possible to the skin's pH (4.5−5.5), but the presence of carbonates can irritate the skin (Matike *et al*., 2011). The presence of iron oxides and hydroxides reduces sorption properties because they adhere to the clay mineral particles and make coatings, thereby reducing the net negative surface charge density of the clay-mineral particles (Zhuang and Yu, 2002). Reduction and extraction of iron oxides from clays increases their CEC (Favre *et al*., 2006). Carbonates and iron oxides/

* E-mail address of corresponding author:
inga.dusenkova@rtu.lv
DOI: 10.1346/CCMN.2014.0620604

hydroxides are usually removed from clays using chemical treatments with dilute acid and sodium dithionite, respectively (Carrado *et al.*, 2006).

The aim of the present study was to investigate the adsorption of two organic compounds found in human sebum (squalene and oleic acid) on illitic, kaolinitic, and chloritic phyllosilicates. To evaluate the influence of the removal of carbonates and iron compounds on adsorption properties, illitic clays were chosen, because, in spite of the widespread occurrence of illite in nature, large deposits of high purity are quite rare (Weaver, 1989; Adamis *et al.*, 2005).

MATERIALS AND METHODS

Clay samples

Three commercial cosmetic clay samples (facial masks) from Russia (Cosm1 and Cosm3) and France (Cosm2) were used. To evaluate the influence of purification, clay samples were collected from three different sites in Latvia: Laza (L130), Prometejs (Prom), and Iecava (Ie). The <63 μm size fraction, obtained by wet sieving, was used in each case.

Clay-sample preparation

Citric (⩾99.7%, Sigma Aldrich, Germany) and hydrochloric acid (37%, Sigma Aldrich, Germany) solutions (1 M) were used to dissolve carbonates. During the dissolution process, clay/water suspensions were stirred and the pH was kept above 4.5 in order to avoid damaging the structure of the clay minerals (Carrado *et al*., 2006). After 3−4 days, when the pH was ~5 and constant, clay samples were washed with distilled water several times, until the electrical conductivity of the supernatant liquid was <100 μS/cm. These clay samples were referred to as −HCl and −C (treated with hydrochloric acid and citric acid, respectively). Before dissolution, the pH of the Ie, L130, and Prom clay suspensions (1:4 clay:water weight ratio) were ~7.4, 7.8, and 7.7, respectively. After dissolution, all samples were in the pH range 6.5−6.8.

Before the removal of iron oxides and hydroxides, all samples were treated with HCl in order to dissolve the carbonates. Dry clay samples (10 g) were mixed with 40 mL of 0.3 M sodium citrate (⩾99%, Sigma Aldrich, Germany) and 5 mL of 1 M sodium bicarbonate (⩾98%, Sigma Aldrich, Germany) solutions. Suspensions were heated to 75−80ºC; 1 g of sodium dithionite (⩾85%, Sigma Aldrich) was added to each and then mixed for 30 min (Mehra and Jackson, 1960). The color of the suspensions changed from brown (samples L130 and Prom) and gray (sample Ie) to blue-green. All suspensions were washed twice with 1 M NaCl (⩾99.5%, Fluka, Germany) and then with distilled water, until the electrical conductivity of the supernatant liquid was <100 μS/cm. The names of all treated samples were given the suffix '-D', *e.g.* Ie-D.

Adsorption experiments

Squalane is the saturated form of squalene (Figure 1) and is also found in small quantities in human sebum (Ledet *et al*., 2013). Adsorption experiments were performed in squalane (99%, Sigma Aldrich, Germany) media containing 2.5 and 25 mg/mL of oleic acid (⩾93%, Sigma Aldrich), 25 and 100 mg/mL of squalene (⩾98%, Sigma Aldrich, Germany). Dry clay samples (0.2 g) were mixed with 1.5 mL of the corresponding mixture and left to stand for 10 and 20 min, the range of average application times of a clay mask. Sample particles were separated from the mixtures by centrifugation for 3 min at 6440 $\times g$). The residue concentration was determined using an Evolution^{TM} 300 UV-VIS spectrophotometer (Thermo Scientific, USA) at 247 and 288 nm for oleic acid and squalene, respectively. For each sample the average result and standard deviation (SD) from at least five parallel experiments were used.

Analysis of untreated and purified clay samples

Powder X-ray diffraction (XRD) was used to identify clay minerals and other mineral phases. An X′Pert PRO diffractometer (PANalytical, USA) using CuKα_1 radiation (generated at 40 mA and 30 kV), with a step size of 0.05º2θ, an irradiated area of 15 mm, and a 1º divergence slit was used. Clay minerals were identified using XRD patterns of air-dried and ethylene glycol-solvated (4 h at 70ºC) oriented aggregates of clay fractions (<2 μm). All oriented clay fractions were heated at 550ºC for 1 h (Poppe *et al*., 2001). The quantitative mineralogical compositions were calculated using the *QUANTO* software (http://libra.msra.cn/Publication/24391217/quanto-a-rietveld-program-for-quantitative-phase-analysis-of-polycrystalline-mixtures, accessed March 2015) which is based on the Rietveld method. Calculations were carried out in triplicate for each sample and the range of all three values was used.

Determination of the chemical composition was by means of X-ray fluorescence spectroscopy (XRF) using a Pioneer S4 spectrometer (Bruker, Germany) with a Rh tube (4 kW) and P10 detector gas. The chemical composition was calculated using the *SPECTRAplus* software (Bruker AXS, Germany). The loss on ignition (LOI) was obtained after heating at 1000ºC for 4 h.

The CEC was determined by the methylene blue (MB) (Fluka, Germany) method. Aliquots of 0.01 M MB

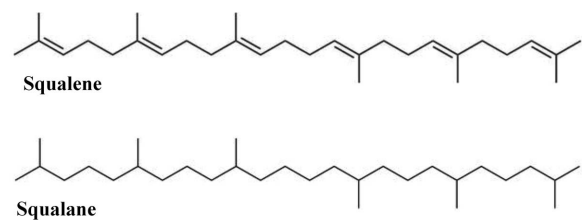

Figure 1. Molecular structure of squalene and squalene.

solution were added to 20 mL of 0.5% (w/w) clay dispersions. The final volume was brought to 60 mL and agitated for 24 h at 25±1ºC (Rytwo *et al.*, 1991). The dispersions were then centrifuged and the concentration of MB was determined by measuring the adsorption at 665 nm using the UV-VIS spectrophotometer mentioned above. The amount of MB adsorbed (meq/100 g of clay) was plotted *vs.* the MB added (meq/100 g of clay) and the point of optimum exchange of MB (CEC) occurs on the curve obtained where it begins to deviate from the initial 45º slope, *i.e.* where the adsorption is no longer 100% (Hang and Brindley, 1970). Experiments were carried out in triplicate and the range of all three values were used.

The specific surface area (SSA) was determined by nitrogen gas adsorption, performed using a QuadraSorb SI instrument (Quantachrome Instruments, USA). The SSA was calculated according to the Brunauer-Emmett-Teller (BET) method from three measurements for each sample. The range of all three values was used.

The particle-size distribution was determined using a laser particle sizer Analysette 22 NanoTec (Fritsch, Germany). For particle-size calculations, Mie theory was used (Mackinnon *et al.*, 1993). The measurements were carried out in triplicate for each sample and the average values were used.

RESULTS AND DISCUSSION

Characteristics of samples

The XRD patterns (Figure 2) showed that all the clay samples contained illite. Chlorite was identified by reflections at 14.1 Å (001), which did not change after glycolation but increased in intensity after heating to 550ºC. Kaolinite was identified by becoming amorphous to XRD after heating to 550ºC, resulting in the disappearance of reflections at 7.1 Å (001). In sample L130, the kaolinite (001) and chlorite (002) reflections overlap, and therefore the kaolinite was identified by its reflection at 2.38 Å (003). Illite (001) and chlorite (001)

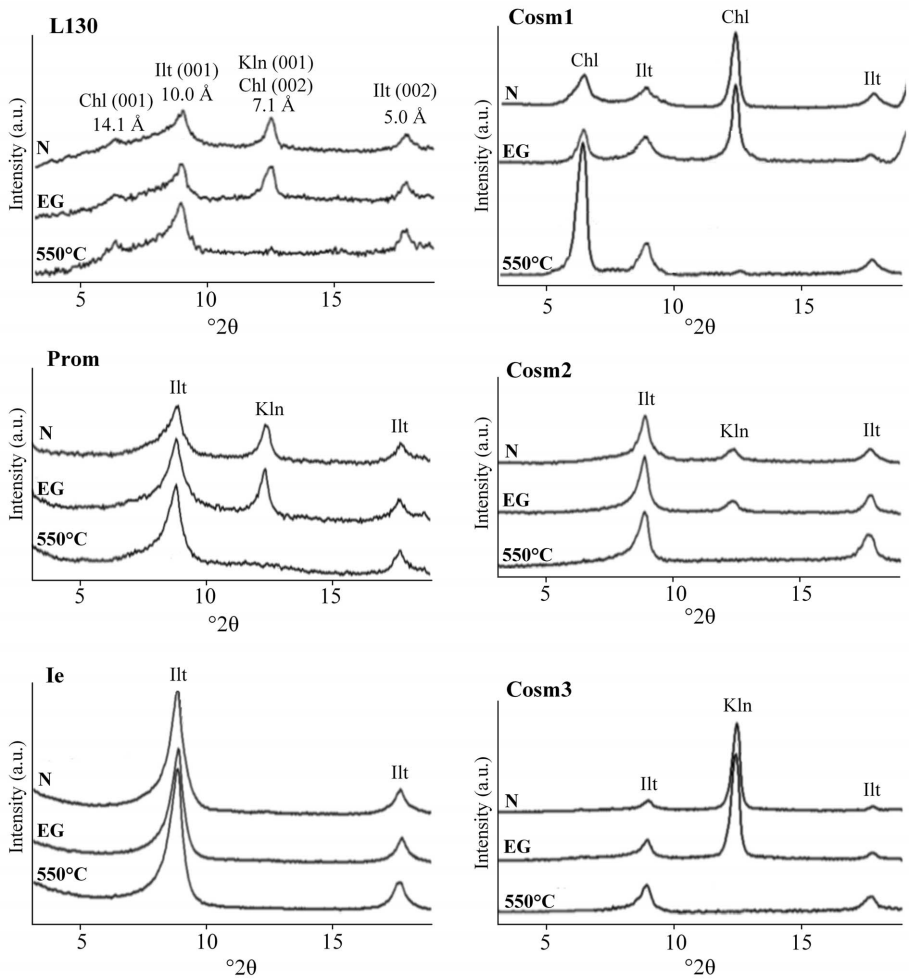

Figure 2. XRD patterns of all samples in air-dried (N), ethylene glycol-solvated (EG), and heated (550ºC) states (Ilt – illite; Kln – kaolinite; Chl – chlorite; abbreviations after Whitney and Evans (2010)).

Table 1. Mineralogical composition (mass%) of the untreated <63 μm fraction clay samples.

Sample	Illite	Kaolinite	Chlorite	Quartz	Feldspars	Dolomite	Calcite	Muscovite
L130	32–36	10–12	6–10	12–14	15–17	4–6	7–9	3–7
Prom	49–53	8–10	–	13–15	9–11	8–10	6–8	–
Ie	48–54	–	–	10–12	24–28	3–5	–	6–10
Cosm1	11–15	–	45–51	20–22	8–10	–	–	7–11
Cosm2	47–55	2–4	–	18–20	19–23	–	–	4–8
Cosm3	8–12	51–57	–	16–20	13–15	–	–	–

Table 2. Chemical composition (mass%) of illitic clays before and after (-D) treatment with sodium dithionite.

Sample	SiO_2	Al_2O_3	Fe_2O_3	CaO	MgO	K_2O	TiO_2	MnO	Na_2O	P_2O_5	LOI	Total
Ie	50.2	19.9	7.2	1.4	3.5	8.7	1.0	0.1	0.5	0.15	7.0	99.6
Ie-D	54.2	21.2	5.8	0.5	2.4	9.4	1.1	0	0.5	0.1	4.0	99.5
L130	43.8	16.8	8.6	7.3	3.2	4.7	0.9	0.1	0.7	0.1	13.8	99.9
L130-D	51.9	18.8	6.3	1.1	2.8	5.3	1.0	0.1	0.6	0.1	11.6	99.5
Prom	38.8	14.7	8.2	8.3	6.2	7.2	1.0	0.1	0.3	0.1	15.1	99.9
Prom-D	46.9	19.1	6.1	0.9	3.9	8.1	1.0	0	0.3	0	13.4	99.6

reflections were not displaced after glycolation, denoting the absence of expandable clay minerals (Moore and Reynolds, 1997).

The mineralogical composition showed that all clay samples contained >50% phyllosilicate minerals (Table 1). Each cosmetic clay sample contained a different type of phyllosilicate mineral: Cosm1 contained mostly chlorite, Cosm2 – illite, and Cosm3 – kaolinite. Of the clay-mineral samples, Prom contained mostly illite, sample Ie contained illite only, and sample L130 contained all three phyllosilicate minerals. In cosmetic clay samples no carbonates were detected; samples Prom and L130 contained both calcite and dolomite; sample Ie contained dolomite only.

The chemical composition (Table 2) showed lower Fe_2O_3 content after the treatment with sodium dithionite. The greatest decrease was observed for samples Prom and L130, by 28 and 26%, respectively. The brown color of these two samples (before the treatment with dithionite) indicated the presence of goethite and possibly hematite (Einsele, 2000), but the amount was below the detection limit of XRD. For sample Ie, the amount of Fe_2O_3 decreased by 19% only and the gray color, which turned red after firing, indicated the presence of FeO (Cuff, 1996). The CaO and MgO contents also reduced due to the dissolution of carbonates. The removal of carbonates and iron oxides and hydroxides was also indicated by the decrease in LOI.

The cumulative particle-size distribution (Figure 3) revealed that all cosmetic clay samples consisted of coarser particles than samples L130 and Prom, which could be the reason for the smaller SSA values than those of samples L130 and Prom (Table 3). Although sample Ie contained coarser particles than all other samples, it also contained finer particles than the other samples and so the SSA value for Ie was only slightly smaller than those for L130 and Prom.

The treatment with acids and sodium dithionite reduced the sizes of the sample particles (Figure 4) and increased the SSA (Table 3), probably because of the removal of Ca^{2+} and Mg^{2+} ions (released from carbonates), and of iron oxides and hydroxides which act as cementing agents (Carrado *et al*., 2006). The purification process also increased the CEC values. The treatment with sodium dithionite which presumably caused the removal of iron oxide and hydroxide coatings from the surfaces of clay mineral particles, thereby increasing the net negative charge (Favre *et al*., 2006),

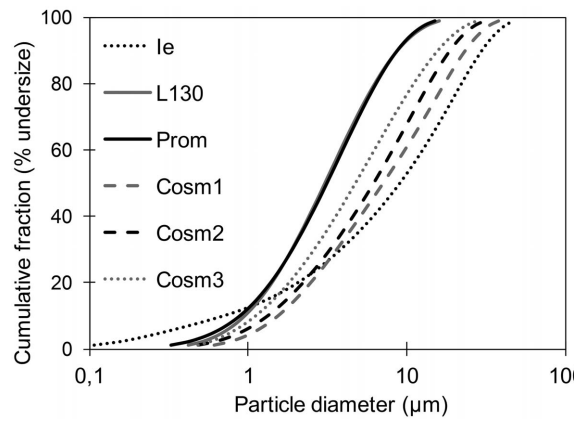

Figure 3. Cumulative particle-size distribution of untreated clays.

Table 3. Physicochemical properties of sample particles.

Sample	CEC (meq/100 g)	SSA (m^2/g)	Cumulative fraction (% undersize)* (μm)		
			d_{10}	d_{50}	d_{90}
Ie	15.2–20.0	45.0–47.3	0.72	9.07	29.75
Ie-HCl	15.4–16.7	46.4–50.0	0.66	8.60	28.05
Ie-C	14.8–16.7	46.4–49.6	0.45	6.88	24.14
Ie-D	18.2–19.8	47.2–50.1	0.55	7.68	26.25
L130	13.5–14.0	50.7–52.2	0.95	3.02	8.64
L130-HCl	12.4–14.7	50.0–52.2	0.90	2.75	8.07
L130-C	13.0–14.0	50.8–53.6	0.70	2.15	6.79
L130-D	17.5–19.0	53.5–55.1	0.72	2.41	6.52
Prom	12.7–14.7	51.4–53.0	0.89	3.14	8.69
Prom-HCl	13.1–14.0	49.4–54.0	0.88	2.71	7.92
Prom-C	13.2–14.7	50.0–52.3	0.85	2.67	7.82
Prom-D	18.0–18.9	54.4–57.0	0.70	2.43	6.49
Cosm1	11.2–12.8	35.7–36.9	1.55	7.06	23.18
Cosm2	12.0–13.0	37.1–40.5	1.33	6.15	18.55
Cosm3	8.4–9.1	37.1–39.3	1.12	4.73	15.59

* The d_{10}, d_{50}, and d_{90} values represent the amounts of all particles (10, 50, and 90%, respectively) that are finer than the particle size shown.

had the most significant effect on the CEC. Another reason could be the reduction of structural Fe(III) to Fe(II), causing an increased layer charge and thereby increasing the CEC (Stucki and Roth, 1977).

Adsorption of oleic acid

The results of the adsorption experiments (Figure 5) revealed that the differences between the amounts of oleic acid adsorbed from a concentration of 2.5 mg/mL by all untreated clay samples were insignificant – from 10 (Cosm3) to 12.7 mg/g (Ie) after 10 min (Figure 5a) and from 14 (Cosm3) to 17.5 mg/g (Ie) after 20 min of adsorption (Figure 5c). In contrast, the adsorption results from an oleic acid concentration of 25 mg/mL showed notable differences in the amount adsorbed by all untreated samples after both 10 and 20 min of adsorption time (Figure 5b,d). Samples Ie, L130, and Prom showed greater adsorption than samples Cosm1, Cosm2, and

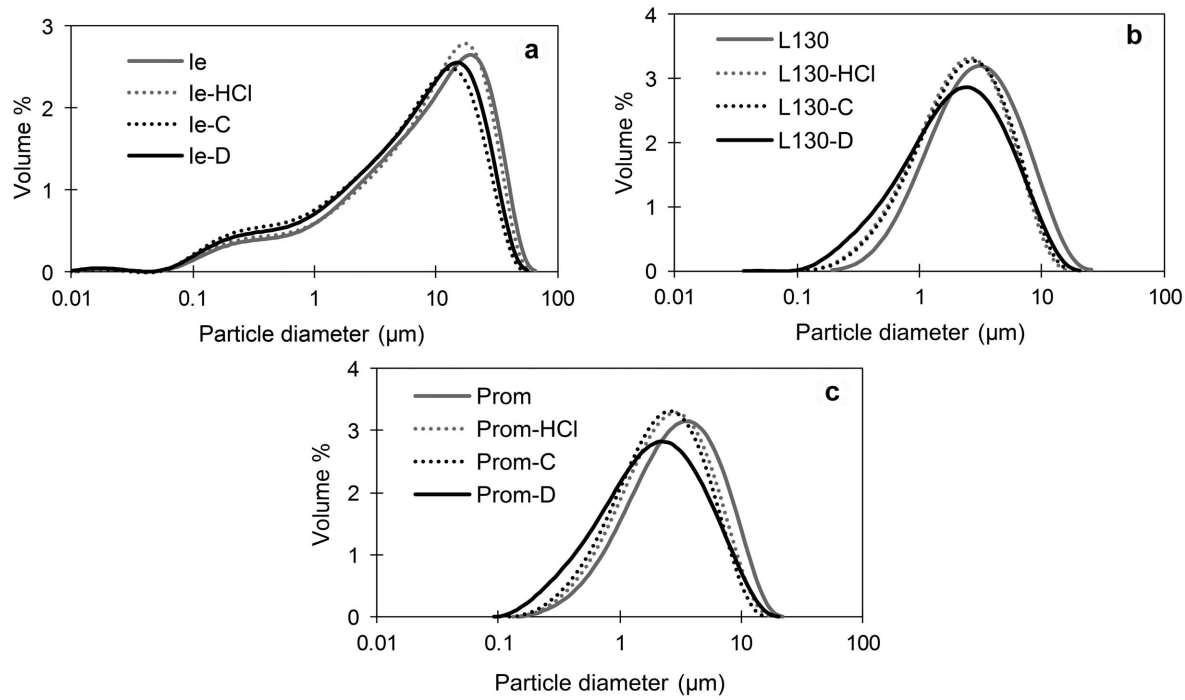

Figure 4. Particle-size distribution of untreated and purified Ie (a), L130 (b), and Prom (c) clay samples.

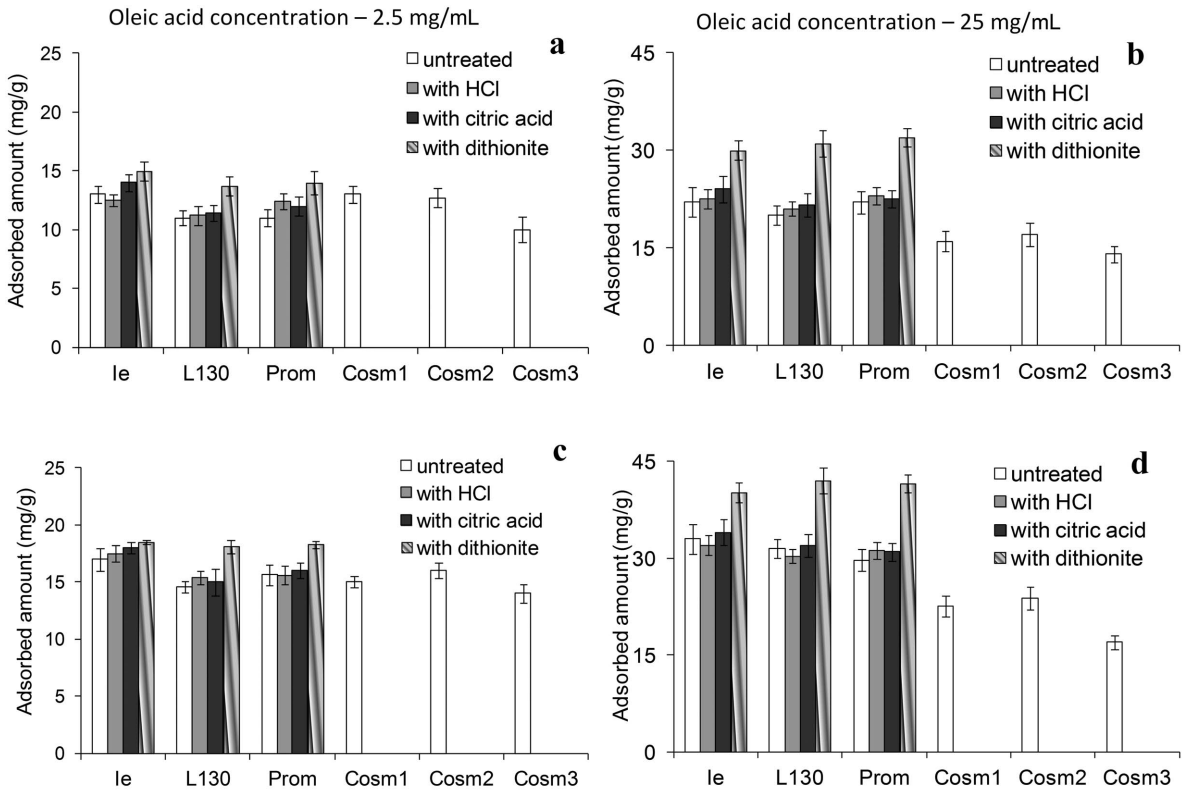

Figure 5. Amounts of oleic acid adsorbed by the clays with initial concentrations of 2.5 and 25 mg/mL after 10 min (a,b) and 20 min (c,d).

Cosm3, which corresponds to their larger CEC values. Although the amount of illite in Cosm2 was similar to that in samples Ie and Prom, the differences in the CEC values and the amount of oleic acid adsorbed can be attributed to coarser particles of Cosm2. The adsorption of oleic acid by sample Cosm1 was slightly less than but similar to that of sample Cosm2, again due to particle size, because chlorite and illite have similar CEC values (Carroll, 1959). Cosm3 adsorbed the smallest amount of oleic acid, probably because of its smaller CEC value.

The removal of iron oxides and hydroxides increased significantly the amount of oleic acid adsorbed because of the increase in CEC (Table 3). Samples Prom-D and L130-D showed greater increases than sample Ie-D in the amount of oleic acid adsorbed, which correlates with the decrease in the amount of Fe_2O_3 after the treatment with sodium dithionite (Table 2). After dissolution of carbonates, the changes in amounts adsorbed were insignificant.

For all samples, ~60–80% of the initial concentration of oleic acid (2.5 mg/ml) was adsorbed after 10 min, and ~80–98% after 20 min. When the initial concentration was 25 mg/mL, only 8–16% of the added oleic acid was adsorbed after 10 min, and ~10–18% after 20 min.

Adsorption of squalene

The results of squalene adsorption (Figure 6) were similar to those for oleic acid, but with some differences. Samples Ie, Ie-HCl, Ie-C, and Ie-D showed the greatest adsorption capacity for squalene, attributed to the largest CEC values for those samples. The adsorption of squalene by the three, untreated illitic clay samples (L130, Prom, and Cosm2) was very similar. As for oleic acid, sample Cosm1 adsorbed slightly less than did the illitic clays but sample Cosm3 adsorbed the smallest amount of squalene. The removal of iron oxides and hydroxides increased significantly the adsorption of squalene, but the dissolution of carbonates caused no significant changes.

The amount of squalene adsorbed from mixtures with initial concentrations of 25 mg/mL (Figure 6a,c) was 1.5–2 times greater than the amount of oleic acid adsorbed from mixtures of the same concentrations. After 10 min, ~10–20% of the squalene added was adsorbed from the mixture with a concentration of 25 mg/mL, and after 20 min that value had increased to 20–33%. By increasing the concentration four times (to 100 mg/mL) the amount adsorbed increased by only 2–5%.

CONCLUSIONS

The results obtained demonstrated that illitic, kaolinitic, and chloritic phyllosilicates adsorb oleic acid and squalene from nonpolar media in a manner similar to sebum. The adsorption capacity of a specific clay depends on the CEC value of the specific clay mineral and also on

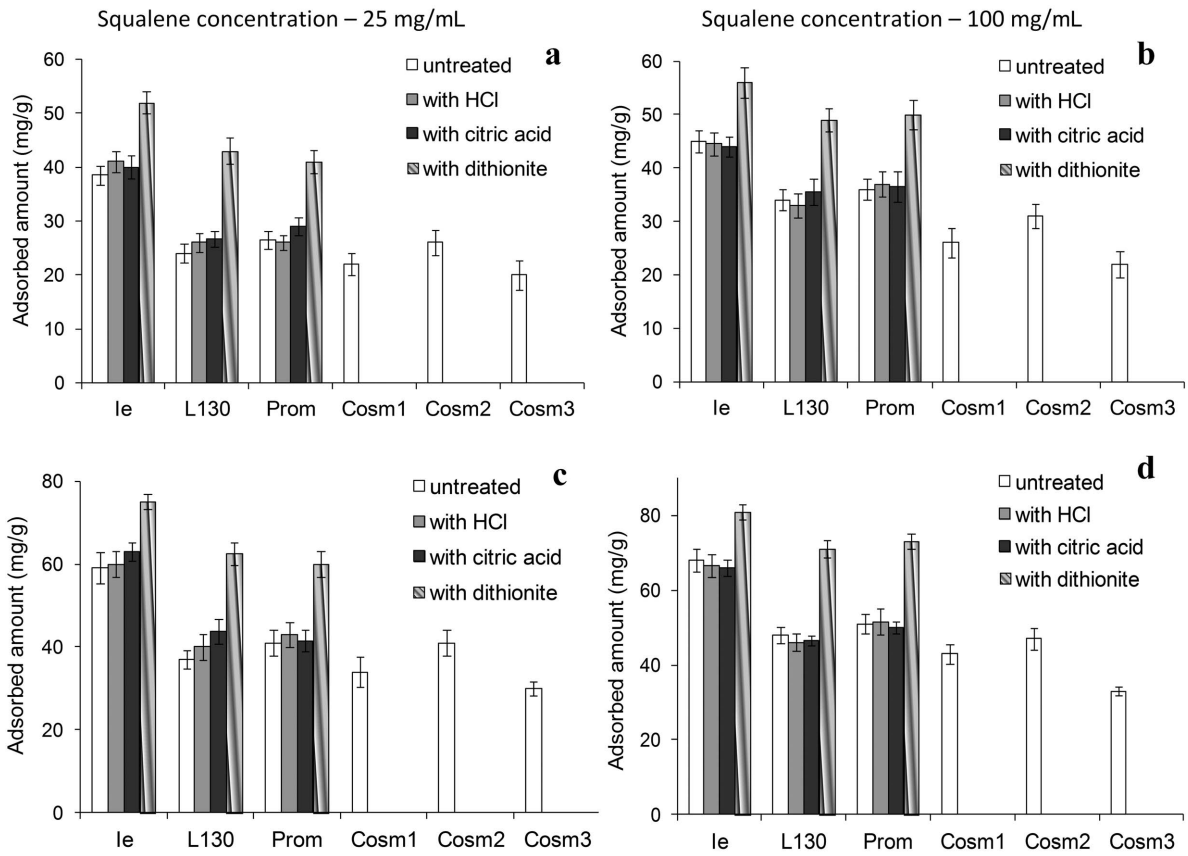

Figure 6. Amount of squalene adsorbed by the clays with initial concentrations of 25 and 100 mg/mL after 10 min (a,b) and 20 min (c,d).

the size of the particles. Illitic and chloritic phyllosilicates showed greater adsorption than kaolinitic clays, which correlates with the CEC values of these minerals in pure form. The purification of illitic clays decreased the particle size of the clay samples and increased the CEC values. The removal of iron oxides and hydroxides increased the CEC value significantly and therefore increased the extent of adsorption of oleic acid and squalene; the dissolution of carbonates had a negligible effect on the adsorption properties. These results revealed that the efficiency of sebum adsorption on clays can be improved by treatment with sodium dithionite and by applying clay masks for at least 20 min.

ACKNOWLEDGMENTS

Support for this work was provided by the Riga Technical University through the Scientific Research Project Competition for Young Researchers No. ZP-2013/21.

REFERENCES

Adamis, Z., Fodor, J., and Williams, R.B. (2005) Sources of human and environmental exposure. Pp. 23–39 in: *Environmental Health Criteria 231: Bentonite, Kaolin and selected Clay Minerals* (M. Sheffer, editor). World Health Organization, Germany.

Carrado, K.A., Decarreau, A., Petit, S., Bergaya, F., and Lagaly, G. (2006) Synthetic clay minerals and purification of natural clays. Pp. 115–139 in: *Handbook of Clay Science* (F. Bergaya, B.K.G. Theng, and G. Lagaly, editors). Elsevier, Amsterdam.

Carretero, M.I. (2002) Clay minerals and their beneficial effects upon human health. A review. *Applied Clay Science*, **21**, 155–163.

Carretero, M.I. and Pozo, M. (2009) Clays and non-clay minerals in the pharmaceutical industry, Part I: Excipients and medical applications. *Applied Clay Science*, **46**, 73–80.

Carretero, M.I. and Pozo, M. (2010) Clays and non-clay minerals in the pharmaceutical and cosmetic industries, Part II: Active ingredients. *Applied Clay Science*, **47**, 171–181.

Carretero, M.I., Gomes, C.S.F., and Tateo, F. (2013) Clays, drugs and human health. Pp. 711–764 in: *Handbook of Clay Science* (F. Bergaya and G. Lagaly, editors). Elsevier, Amsterdam.

Carroll, D. (1959) Ion exchange in clays and other minerals. *Geological Society of America Bulletin*, **70**, 749–780.

Cuff, Y.H. (1996) Preparing and testing natural clays for workshop use. Pp. 149–158 in: *Technology for Potters and Sculptors*. University of Pennsylvania Press, USA.

Downing, D.T., Stranieri, A.M., and Strauss, J.S. (1982) The effect of accumulated lipids on measurements of sebum secretion in human skin. *Journal of Investigative Dermatology*, **79**, 226–228.

Einsele, G. (2000) Special depositional environments and sediments. Pp. 249–283 in: *Sedimentary Basins: Evolution, Facies and Sediment Budget*. Springer, Germany.

Favre, F., Bogdal, C., Gavillet, S., and Stucki, J.W. (2006) Changes in the CEC of a soil smectite–kaolinite clay fraction as induced by structural iron reduction and iron coatings dissolution. *Applied Clay Science*, **34**, 95–104.

Greenland, D.J., Laby, R.H., and Quirk, J.P. (1965) Adsorption of amino-acids and peptides by montmorillonite and illite. Part 1. Cation exchange and proton transfer. *Transactions of the Faraday Society*, **61**, 2013–2023.

Hang, P.T. and Brindley, G.W. (1970) Methylene blue absorption by clay minerals. Determination of surface areas and cation exchange capacities (clay-organic studies XVIII). *Clays and Clay Minerals*, **18**, 203–212.

Harris, H.H., Downing, D.T., Steward, M.E., and Strauss, J.S. (1983) Sustainable rates of sebum secretion in acne patients and matched normal control subjects. *Journal of the American Academy of Dermatology*, **8**, 200–203.

Johnston, C.T. (1996) Sorption of organic compounds on clay minerals: A surface functional group approach. Pp. 1–44 in: *Organic Pollutants in the Environment* (B. Sawhney, editor). Workshop Lectures Series, **8**, The Clay Minerals Society, Boulder, Colorado, USA.

Johnston, C.T. (2010) Probing the nanoscale architecture of clay minerals. *Clay Minerals*, **45**, 245–279.

Khiari, I., Mefteh, S., Sánchez-Espejo, R., Cerezo, P., Aguzzi, C., López-Galindo, A., Jamoussi, F., and Iborra, V.C. (2014) Study of traditional Tunisian medina clays used in therapeutic and cosmetic mud-packs. *Applied Clay Science*, **101**, 141–148.

Ledet, G., Bostanian, L.A., and Mandal, T.K. (2013) Nanoemulsions as a vaccine adjuvant. Pp. 125–142 in: *Bioengineered Nanomaterials* (A. Tiwari and A. Tiwari, editors). CRC Press, Boca Raton, Florida, USA.

Li, Y. and Gupta, G. (1994) Adsorption/desorption of hydrocarbons on clay minerals. *Chemosphere*, **28**, 627–638.

Lopez-Galindo, A. and Viseras, C. (2004) Pharmaceutical and cosmetic applications of clays. Pp. 267–289 in: *Clay Surfaces, Fundamentals and Applications* (F. Wypych and K.G. Satyanarayana, editors). Elsevier, Amsterdam.

Lopez-Galindo, A., Viseras, C., and Cerezo, P. (2007) Compositional, technical and safety specifications of clays to be used as pharmaceutical and cosmetic products. *Applied Clay Science*, **36**, 51–63.

Mackinnon, I.D.R., Uwins, P.J.R., Yago, A., and Page, D. (1993) Kaolinite particle sizes in the <2 μm range using laser scattering. *Clays and Clay Minerals*, **41**, 613–623.

Matike, D.M.E., Ekosse, G.I.E., and Ngole, V.M. (2011) Physico-chemical properties of clayey soils used traditionally for cosmetics in Eastern Cape, South Africa. *International Journal of the Physical Sciences*, **33**, 7557–7566.

Mehra, O.P. and Jackson, M.L. (1960) Iron oxide removal by dithionite. *Clays and Clay Minerals*, **7**, 317–327.

Moore, D.M. and Reynolds, R.C. (1997) *X-ray Diffraction and the Identification and Analysis of Clay Minerals*. Oxford University Press, New York, pp. 227–260.

Pappas, A., Johnsen, S., Liu, J.C., and Eisinger, M. (2009) Sebum analysis of individuals with and without acne. *Dermatoendocrinology*, **3**, 157–161.

Poppe, L.J., Paskevich, V.F., Hathaway, J.C., and Blackwood, D.S. (2001) A laboratory manual for X-ray powder diffraction. *U.S. Geological Survey Open-File Report 01–041*, 33 pp.

Rytwo, G., Serban, S., Nir, S., and Margulies, L. (1991) Use of methylene blue and crystal violet for determination of exchangeable cations in montmorillonite. *Clays and Clay Minerals*, **39**, 551–555.

Schwartz, J.R., Yvonne, M., DeAngelis, Y.M., and Dawson, T.L. (2012) Dandruff and seborrheic dermatitis: A head scratcher. Pp. 389–414 in: *Practical Modern Hair Science* (T. Evans and R.R. Wickett, editors). Allured Publishing Corporation, USA.

Stucki, J.W. and Roth, C.B. (1977) Oxidation–reduction mechanism for structural iron in nontronite. *Soil Science Society of America Journal*, **41**, 808–814.

Tateo, F. and Summa, V. (2007) Element mobility in clays for healing use. *Applied Clay Science*, **36**, 67–76.

Thiboutot, D. (2004) Regulation of human sebaceous glands. *Journal of Investigative Dermatology*, **123**, 1–12.

Vecstaudža, J., Stunda-Zujeva, A., Irbe, Z., and Brziņa-Cimdiņa, L. (2012) Komercilo kosmtisko mlu sastvs un Latvijas mlu piemrotba lietojumam kosmtik. *Scientific Journal of RTU: Material Science and Applied Chemistry*, **26**, 42–49.

Veniale, F., Better, A., Jobstraibizer, P., and Setti, M. (2007) Thermal muds: perspective of innovations. *Applied Clay Science*, **36**, 141–147.

Weaver, C.E. (1989) Evolution of physils and continents. Pp. 561–704 in: *Clays, Muds and Shales.* Developments in Sedimentology, **44**. Elsevier, Amsterdam.

Whitney, D.L. and Evans, B.W. (2010) Abbreviations for names of rock-forming minerals. *American Mineralogist*, **95**, 185–187.

Williams, L.B., Haydel, S.E., Giese Jr., R.F., and Eberl, D.D. (2008) Chemical and mineralogical characteristics of French green clays used for healing. *Clays and Clay Minerals*, **56**, 437–452.

Youn, S.W. (2010) The role of facial sebum secretion in acne pathogenesis: facts and controversies. *Clinics in Dermatology*, **28**, 8–11.

Zague, V., Silva, D.A., Baby, A.R., Koneko, T.M., and Velasco, M.V.R. (2007) Clay facial masks: Physicochemical stability at different storage temperatures. *Journal of Cosmetic Science*, **58**, 45–51.

Zhuang, J. and Yu, G.R. (2002) Effects of surface coatings on electrochemical properties and contaminant sorption of clay minerals. *Chemosphere*, **49**, 619–628.

Zouboulis, C.C. (2004) Acne and sebaceous gland function. *Clinics in Dermatology*, **22**, 360–366.

(*Received 8 July 2014; revised 5 January 2015; Ms. 906; AE: H. Dong*)

Clays and Clay Minerals, Vol. 62, No. 6, 508–518, 2014.

SYNTHESIS AND CHARACTERIZATION OF ZEOLITE NaY USING KAOLIN WITH DIFFERENT SYNTHESIS METHODS

MARYAM TAVASOLI[1,*], HOSSEIN KAZEMIAN[2], SODEH SADJADI[3], AND MORTEZA TAMIZIFAR[4]

[1] Department of Materials Engineering, Islamic Azad University, Science and Research, PO Box 775/14515, Tehran, Iran
[2] Department of Chemical and Biochemical Engineering, Faculty of Engineering, Western University, London, Ontario, Canada N6A 5B9
[3] Nuclear Fuel Cycle School, Nuclear Science and Technology Research Institute, End of North Karegar Ave., PO Box 1439951113, Tehran, Iran
[4] Iran University of Science and Technology, Tehran, Iran

Abstract—The benefits of using kaolin as a source of aluminosilicate in zeolite synthesis to obtain lower-cost catalysts, adsorbents, or ion exchangers are widely known. Previous attempts to produce zeolite from natural Iranian kaolin resulted in the formation of zeolites A, X, and HS. Zeolite Y plays an important role in the petrochemical industry due to its application in the area of fluidized catalytic cracking; ~40% of gasoline production is obtained using this process.

In the present study, different methods were used to prepare pure zeolite NaY from the Iranian kaolin available. The effects of different parameters such as aging time, crystallization time, kaolin calcination and crystallization temperature, and starting-material composition were investigated in order to obtain improved properties and maximize phase purity. In all cases, the crystal structure and microstructure were studied using X-ray diffraction and scanning electron microscopy. Among different synthesis approaches, the 'guide-agent method' resulted in the formation of zeolite NaY. The synthesis was generally sensitive to changes in kaolin calcination temperature and in hydrothermal synthesis parameters. The optimum parameters to prepare pure zeolite NaY were: kaolin calcination temperature = 680ºC, aging time of guide agent = 48 h without an overall gel aging step, and crystallization at 90ºC for 36 h.

Key Words—Kaolin, Synthesis Methods, Zeolite NaY.

INTRODUCTION

Zeolites are crystalline aluminosilicates with pores of molecular dimensions that are widely used in applications such as separation, catalysis, ion exchange, and adsorption (Song *et al*., 2005). Zeolite Y, a highly versatile member of the faujasite family, plays a significant role in the petrochemical industry (Sang *et al*., 2006) due to its application in the area of fluidized catalytic cracking (FCC) through which ~40% of gasoline production is obtained.

More than 40 natural zeolites have been identified over the past 200 years but no significant commercial uses were found for them until synthetic zeolites were discovered and developed. Modern studies of synthetic zeolites have focused mainly on the use of inexpensive initial or waste materials (Georgiev *et al*., 2013). Zeolites are usually synthesized from low-cost silica-alumina sources in alkaline phases under hydrothermal conditions. The low-cost silica-alumina sources are fly ash and kaolin (Htay and Oo, 2008).

Kaolin is a convenient source of Si-Al for synthesizing low-silica zeolites such as zeolite Y (Chandrasekhar and Pramada, 2004). One of the main routes for preparing zeolite NaY is the so-called '*in situ*' process from kaolin. Two steps are involved in this process: (1) dehydroxylation of kaolin to form an activated material known as metakaolin; and (2) hydrothermal treatment of metakaolin with aqueous alkali to form zeolite (Chandrasekhar, 1996). The keys to this process are the activation of the kaolin and the subsequent hydrothermal synthesis (Liu *et al*., 2003).

Previous attempts to produce zeolite from natural Iranian kaolin resulted in the formation of zeolites A, X, and HS (Farzaneh, 1989). The aim of the present study was to synthesize microsized NaY zeolite because of its properties, *e.g.* its highly catalytic center, large surface/atom ratio, large surface area, large surface energy, and better retro-wear. The FCC catalysts prepared from microsized NaY zeolite with a large Si/Al ratio possess high catalytic activity and can be used in the refining of residual and heavy oils. Use of microsized NaY zeolite has been reported (Bo and Hongzhu, 1998) to improve catalytic cracking selectivity, reduce coke formation, increase the yield of diesel oil, and promote gasoline quality; use in the fine-chemical industry has also been reported.

In the present study, attempts were made, at various temperatures (680−950ºC), using locally available Iranian kaolin, to prepare zeolite NaY from metakaolin. Four different synthesis approaches were tried. In all cases, the crystal structure and microstructure were

* E-mail address of corresponding author:
mtavasoli366@gmail.com
DOI: 10.1346/CCMN.2014.0620605

studied by means of X-ray diffraction (XRD) and scanning electron microscopy (SEM).

EXPERIMENTAL

Materials

Kaolin was obtained from Kaolin Shargh Co. (Tehran, Iran). The chemical composition of the natural sample was determined by X-ray fluorescence (Table 1). The NaOH, sodium silicate ($SiO_2 \cdot Na_2O$), and sodium aluminate ($Al_2O_3 \cdot Na_2O$) were obtained from Merck Company (Whitehouse Station, New Jersey, USA) and used as received.

Apparatus

The crystal structure of the NaY powder synthesized was analyzed using CuKα radiation (Philips PW 1800, Amsterdam, The Netherlands).

The Fourier-transform infrared (FTIR) spectra of the samples were recorded using a Perkin-Elmer2000 FTIR spectrometer (Waltham, Massachusetts, USA). The particle size and morphology of the zeolites were examined using scanning electron microscopy-energy dispersive spectroscopy (SEM/EDS), using an XL30 instrument manufactured by Philips (Amsterdam, The Netherlands). The surface area of the zeolites was determined by the nitrogen adsorption method using a BELSORP-MINI II instrument (Toyonaka, Japan) in accordance with the Brunauer-Emmett-Teller (BET) method (Brunauer *et al*., 1938). The thermal stability of the zeolites was studied by thermogravimetric analysis using a TGA/DSC851e device (Mettler Toledo, Columbus, Ohio, USA) with heating rate of 10ºC/min from room temperature to 800ºC in the argon atmosphere.

Synthesis of zeolite NaY

For all four methods, the processes of synthesizing zeolite from kaolin share the same preparation procedure. This procedure began by converting kaolin to metakaolin. To accomplish this, the kaolin was activated at different temperatures; 680ºC for synthetic methods M_1-M_3, and 950ºC for method M_4. The sample was heated from 25 to 680 or 950ºC at a constant rate of 10ºC/min in air. When the calcination temperature was reached, the crucibles were left in the furnace for 3 h. Then, the crucibles were removed from the furnace and cooled in air. The conversion of the kaolin to metakaolin was confirmed by XRD analyses of the starting and thermally treated kaolin samples (Figure 1). The resulting metakaolins were then sieved through a 45 μm mesh and divided into four groups, ready for use in each of the four synthesis methods (M_1-M_4) to prepare zeolite NaY.

Table 1. Chemical analysis of the kaolinite mineral.

Component	Wt.%
SiO_2	57.66
Al_2O_3	30.71
Fe_2O_3	0.15
CaO	0.08
Na_2O	0.04
K_2O	0.01
MgO	0.001
TiO_2	0.079
MnO	0.001
P_2O_5	0.018
L.O.I*	10.88

* Loss on ignition.

Method 1 – alkali fusion method (M_1)

To synthesize zeolite by employing method 1 (Figure 2a), metakaolin synthesized by kaolin activation at 680ºC for 3 h was fused by the addition of NaOH at 550ºC for 3 h. Then, the solid products were ground with a fast mill (Pouyesh Sanat, Abyek, Iran), and sieved through a 45 μm mesh.

The resulting product was mixed with a calculated amount of sodium silicate and water (Table 2) to produce a system with molar composition SiO_2/Al_2O_3 = 5.3, Na_2O/SiO_2 = 0.25, and H_2O/Na_2O = 40. This material was kept for aging at room temperature for 24 h. After 24 h of aging, an aqueous pink gel appeared which was transferred to an autoclave, where the hydrothermal crystallization was carried out at 100ºC for 12 h. After this, the precipitate was filtered, washed several times with distilled water until pH = 9–10 (the pH of the water in equilibrium with the zeolite in the filter had already been measured), and then dried at 100ºC for 12 h.

Method 2 – synthesis without seed (M_2)

To synthesize zeolite using method 2 (Figure 2b), a calculated amount of sodium hydroxide, sodium silicate, and water were added to metakaolin (Table 3). These were mixed in order to achieve the same molar ratios as for method M_1 (SiO_2/Al_2O_3 = 5.3, Na_2O/SiO_2 = 0.25, and H_2O/Na_2O = 40). Then the mixture was aged at room temperature for 24 h to form a gel slurry. On heating at 100ºC, this gel slurry crystallized into zeolite over 36 h. After completion of hydrothermal crystallization, the resultant precipitate was separated and then

Table 2. Raw materials and their amounts used in the synthesis of the M_1 sample.

Raw materials	Amount (g)
Kaolin	32.21
NaOH	5.94
$Na_2O \cdot SiO_2$	71.4
H_2O	32.21

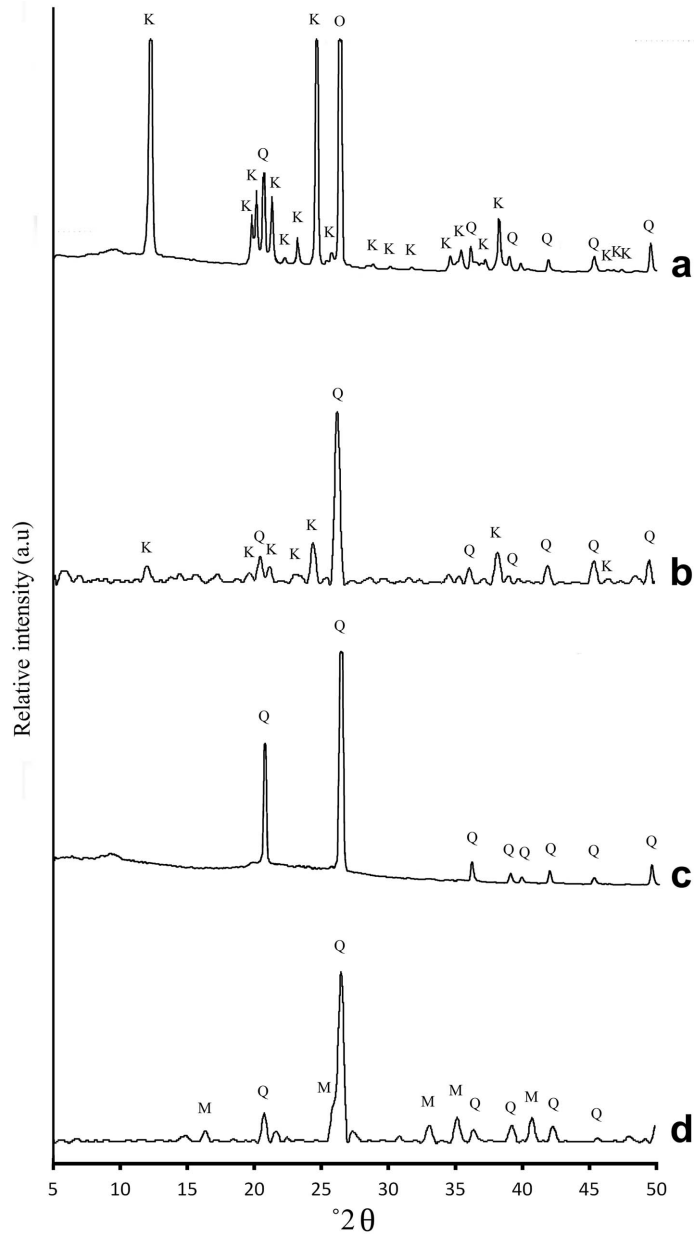

Figure 1. XRD patterns of (a) kaolin, and kaolin calcination obtained from kaolin activation at (b) 400ºC, (c) 680ºC, and (d) 1100ºC for 3 h. K: kaolinite, M: mullite, Q: quartz.

Table 3. Raw materials and their amounts used in the synthesis of the M_2 sample.

Raw materials	Amount (g)
Kaolin	29.513
NaOH	3.11
$Na_2O{\cdot}SiO_2$	66.942
H_2O	57.63

washed with deionized water until a pH range of 9−10, and dried at 100ºC for 12 h.

Method 3 − synthesis with zeolite NaY powder seed (M_3)

Preparation method 3 (Figure 2c) was similar to method 2, but differed in that zeolite NaY was used as seeding. The initial precursor was prepared by mixing the required amounts of metakaolin, zeolite NaY, sodium hydroxide, sodium silicate, and water (Table 4) to produce a system with molar composition SiO_2/Al_2O_3 = 5.3, Na_2O/SiO_2 = 0.25, and H_2O/Na_2O = 40, and then the zeolite NaY seed powder (3 g) was added to this mixture.

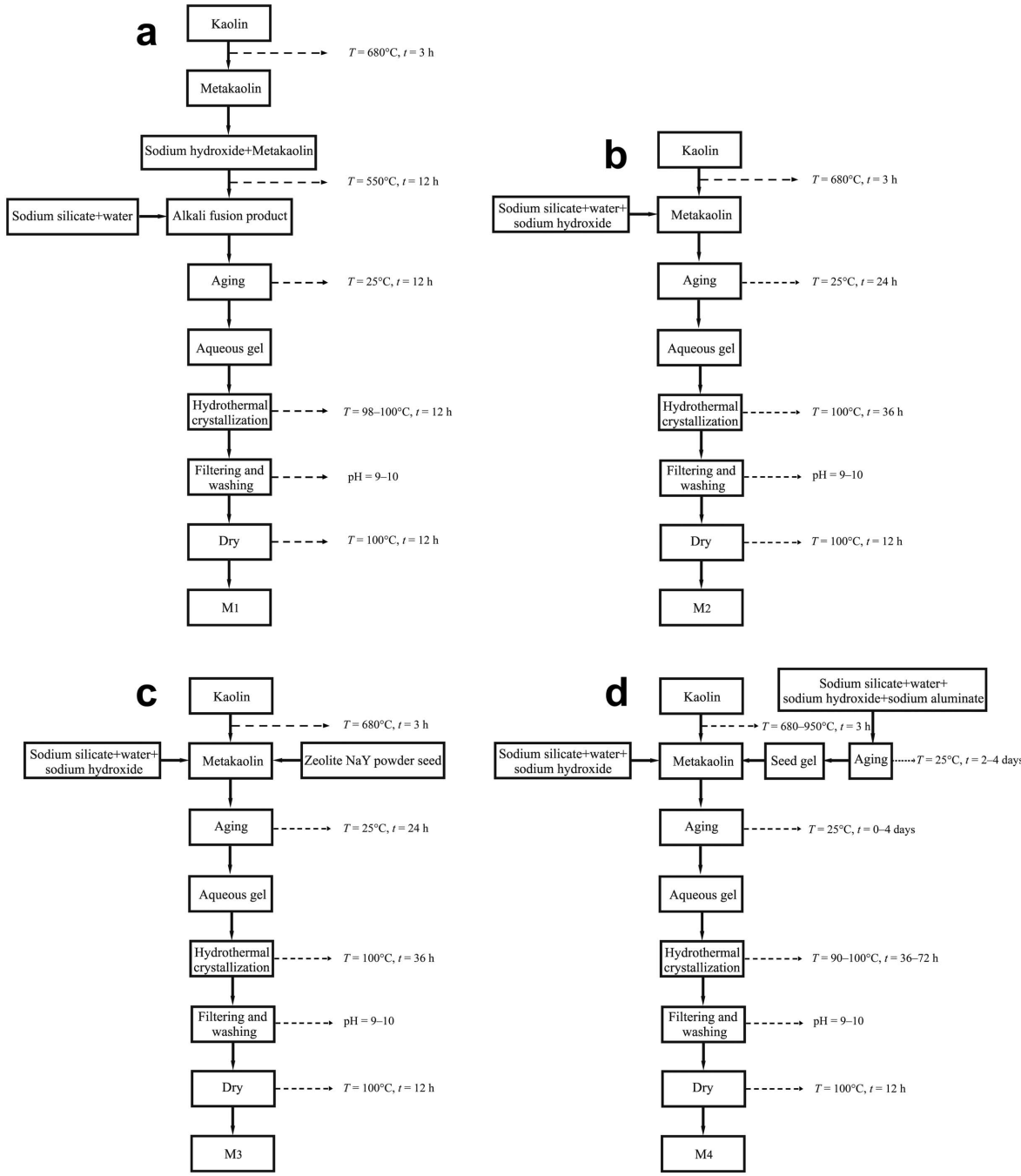

Figure 2. Different synthetic methods used to prepare zeolite NaY: (a) M_1, (b) M_2, (c) M_3, and (d) M_4.

Method 4 – guide-agent method (M_4)

In method 4 (Figure 2d), crystallization of zeolite NaY by the guide-agent method was also used and the effects of the different parameters such as kaolin calcination temperature, guide agent, and overall gel aging time, and crystallization time and temperature on the zeolite NaY preparation were studied in detail.

The metakaolins were prepared by heating the kaolin at 680 and 950ºC for 3 h in a muffle furnace. The guide agent was prepared from a mixture of sodium hydroxide, sodium silicate, and sodium aluminate (Table 5).

Firstly, the sodium aluminate solution was prepared by dissolving a calculated amount of the sodium aluminate in deionized water. This solution was then mixed with the sodium hydroxide and sodium silicate under constant stirring for 15 min. The resulting slurry was aged at room temperature for various times (2 and 4 h) to form a gel slurry.

Table 4. Raw materials and their amounts used in the synthesis of the M_3 sample.

Raw materials	Amount (g)
Kaolin	29.513
NaOH	3.11
$Na_2O{\cdot}SiO_2$	66.942
H_2O	57.63
Zeolite NaY powder seed	3

The overall gel was prepared by mixing the calculated amount of sodium hydroxide, sodium silicate, metakaolin, water, and guide agent to produce a system with molar composition $SiO_2/Al_2O_3 = 5.3$, $Na_2O/SiO_2 = 0.25$, and $H_2O/Na_2O = 40$ (Table 6). Then the mixture was aged at room temperature to form a gel slurry. The gel-like mixture was transferred to an autoclave, where hydrothermal crystallization was carried out at different times and temperatures. The hydrothermal crystallization was also carried out immediately after the overall gel preparation without an aging step. Various guide-agent method conditions ($M_{4\text{-}1}$–$M_{4\text{-}8}$) were applied. To study the effect of the calcination temperature of kaolin on the quality of the final product, three calcination temperatures, 680ºC, 800ºC and 950ºC were investigated for $M_{4\text{-}1}$, $M_{4\text{-}4}$, and $M_{4\text{-}5}$, respectively. The other parameters were kept constant including the aging time of the guide agent (Figure 2d), 0 h of overall gel aging time, crystallization temperature (100ºC), and crystallization time (36 h).

Two different aging times of the guide agent, 2 h and 4 h, were studied for samples $M_{4\text{-}1}$ and $M_{4\text{-}6}$, respectively, under constant conditions including kaolin calcination temperature (680ºC), 0 h of overall gel aging time, crystallization temperature (100ºC), and crystallization time (36 h).

Overall gel aging time is the next parameter that influences the hydrothermal crystallization and so it was evaluated under two sets of different conditions: 0 h in $M_{4\text{-}1}$ and 4 h in $M_{4\text{-}7}$. Other parameters were constant including kaolin calcination temperature (680ºC), aging time of the guide agent (2 days), crystallization temperature (100ºC), and crystallization time (36 h).

Another parameter is crystallization temperature. Crystallization temperatures of 100ºC in $M_{4\text{-}1}$ and 90ºC in $M_{4\text{-}8}$ were examined. The other parameters are kaolin calcination temperature (680ºC), aging time of guide agent (2 days), 0 h overall gel aging time, and crystallization time (36 h).

To investigate the effect of crystallization time, hydrothermal crystallization was carried out at different crystallization times: 36 h in $M_{4\text{-}1}$, 50 h in $M_{4\text{-}2}$, and 72 h in $M_{4\text{-}3}$. Other reaction parameters including kaolin calcination temperature (680ºC), aging time of the guide agent (2 days), 0 h of overall gel aging time, and crystallization temperature (100ºC) were kept constant during this experimental series.

Table 5. Raw materials and their amounts used in preparation of the guide agent for M_4 samples.

Raw materials	Amount (g)
$Na_2O{\cdot}SiO_2$	10.2
NaOH	2.94
$NaAlO_2$	0.652
H_2O	13.26

Table 6. Raw materials and their amounts used in the preparation of the overall gel for M_4 samples.

Raw materials	Amount (g)
Kaolin	30
Guide agent	18
NaOH	1.03
$Na_2O{\cdot}SiO_2$	59.43
H_2O	43.379

RESULTS AND DISCUSSION

Properties of metakaolin

The effect of temperature on the kaolin calcination was examined at temperatures ranging from 400 to 1100ºC. Various XRD patterns of the clay and metakaolins were observed (Figure 1). The clay showed all the characteristic peaks of kaolinite (K) with quartz impurities (Q). On calcination, these peaks disappeared giving a featureless band of X-ray amorphous metakaolin. Kaolin calcination was indicated as complete at 680ºC. Heating at 1100ºC for 3 h resulted in the formation of new phase, mullite (M), which could not transform to zeolite NaY. For these reasons, the influence of kaolin calcination temperature on the formation of zeolite NaY was studied at the temperatures of 680 and 950ºC.

Comparison of the different synthesis methods in the formation of zeolite NaY

Different synthesis methods (M_1–M_4) were used to prepare zeolite NaY. The XRD results (Figure 3) show that the structure of the zeolites prepared from metakaolin depends significantly on the synthesis method chosen. When methods M_1 and M_4 were used, the characteristic peaks of zeolite NaY could exist together with the competitive phase of zeolite P, while, in the product samples M_2 and M_3, only the characteristic peaks of zeolite P were seen.

To prepare zeolite NaY, the guide-agent method was chosen because of the simple synthesis conditions required. Compared with the guide-agent method, the alkali fusion method was more time consuming and

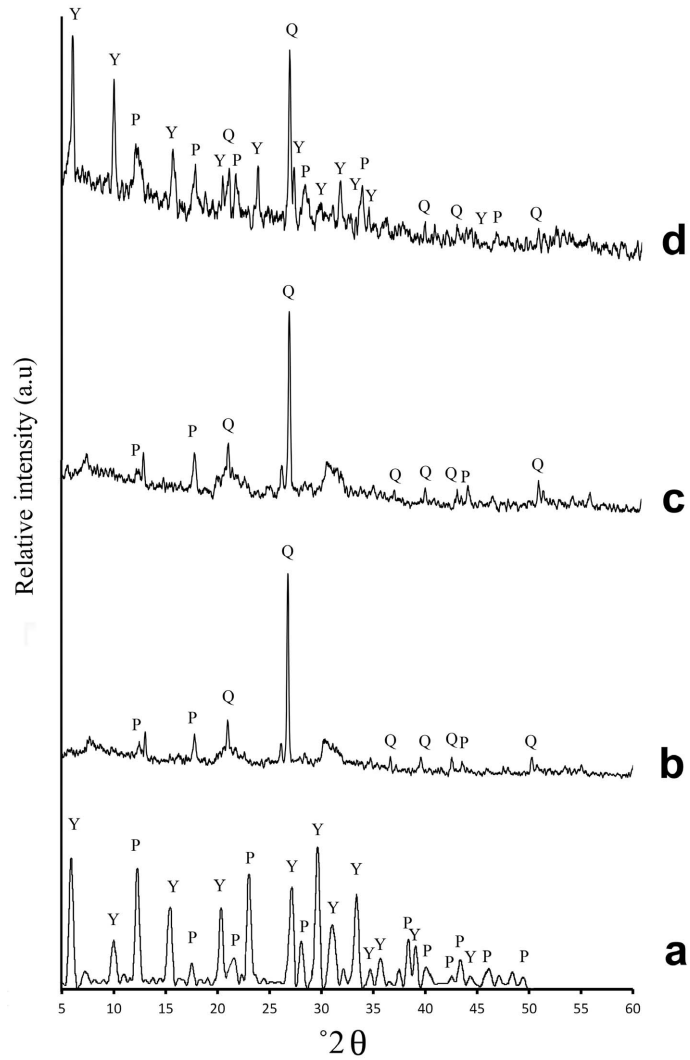

Figure 3. XRD patterns of products from the different synthesis methods : (a) M_1, (b) M_2, (c) M_3, and (d) $M_{4\text{-}1}$. P: zeolite P; Y: zeolite NaY, Q: quartz.

required a high calcination temperature; the residual fusion product was difficult to remove because it was tough and had to be ground.

Optimization of guide-agent method

To obtain a pure NaY phase, the effects of various parameters such as kaolin calcination temperature, guide agent, and overall gel aging time, crystallization time, and temperature ($M_{4\text{-}1}$−$M_{4\text{-}8}$) on the zeolite NaY formation were investigated.

The effect of kaolin calcination temperature

To investigate the effect of kaolin calcination temperature on the structure of the zeolites, comparative experiments at different kaolin calcination temperatures were carried out (Table 7, $M_{4\text{-}1}$, $M_{4\text{-}4}$, and $M_{4\text{-}5}$). The gel-preparation and hydrothermal-crystallization steps (Table 7) were similar but differed in terms of the kaolin-calcination temperature (680, 800, 950ºC for $M_{4\text{-}1}$, $M_{4\text{-}4}$, and $M_{4\text{-}5}$, respectively).

Clearly, the XRD results (Figure 4) show that when the starting kaolin was activated at 680ºC, the formation of zeolite P was competitive with zeolite NaY. When the kaolin calcination temperature was increased to 800ºC, the intensity of zeolite NaY was decreased and the formation of zeolite P dominated. The XRD patterns of solids obtained in the $M_{4\text{-}5}$ experiment, showed no zeolitic phases. These observations can be interpreted as follows: the kaolin structure transforms significantly to metakaolin ($2Al_2O_3{\cdot}4SiO_2$) at temperatures up to 500ºC. At 925ºC metakaolin layers condense to form a spinel-type phase of approximate composition $2Al_2O_3{\cdot}3SiO_2$ following removal of the silica (Brindley and Nakahira, 1959). On this basis, as the temperature increased to 800ºC, the transformation of metakaolin to the spinel resulted in the Si/Al ratio reduction, and so the

Table 7. Different conditions for the guide agent-method (M_{4-1}–M_{4-8}).

Sample	Kaolin calcination temperature (ºC)	Aging time of guide agent (days)	Overall gel aging time (days)	Crystallization temperature (ºC)	Crystallization time (h)
M_{4-1}	680	2	0	100	36
M_{4-2}	680	2	0	100	50
M_{4-3}	680	2	0	100	72
M_{4-4}	800	2	0	100	36
M_{4-5}	950	2	0	100	36
M_{4-6}	680	4	0	100	36
M_{4-7}	680	2	4	100	36
M_{4-8}	680	2	0	90	36

formation of the low-silica zeolite P was dominant. On further increase of the temperature to 950ºC, metakaolin transformed completely to the spinel phase which was stable and could not be transformed to zeolite.

The effect of aging time

The effect of the guide agent and overall gel aging time on zeolite formation was also investigated in terms of the reduction of zeolite P formation (Table 7, M_{4-1}, M_{4-6}, and M_{4-7}).

To investigate the effect of aging time of the guide agent, two experiments were carried out for different aging times (48 h and 96 h) without an overall gel aging step. Zeolite NaY was obtained for an aging time of 48 h. Increasing the aging time of the guide agent to 96 h had a negative effect on the preparation of zeolite NaY; zeolite P became the dominant phase.

To study the effect of the overall gel aging time on zeolite NaY formation, a similar reaction was carried out with 48 h of aging time of the guide agent and 96 h of overall gel aging time. The XRD patterns of the comparative experiments (Figure 5) revealed that when the overall gel was aged, only the characteristic peaks of zeolite P were seen. Therefore, in the formation of zeolite NaY, the optimal aging time for the guide agent was 48 h without overall gel aging.

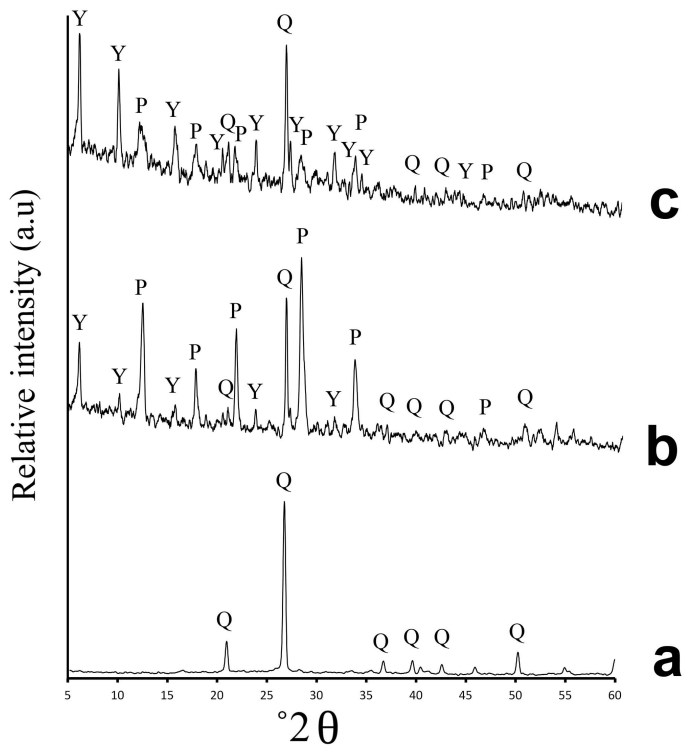

Figure 4. The effect of kaolin calcination temperature on XRD patterns of the products, crystallized at 100ºC for 36 h. Kaolin calcination temperature: (a) 950ºC M_{4-5}, (b) 800ºC M_{4-4}, and (c) 680ºC M_{4-1}. P: zeolite P; Y: zeolite NaY; Q: quartz.

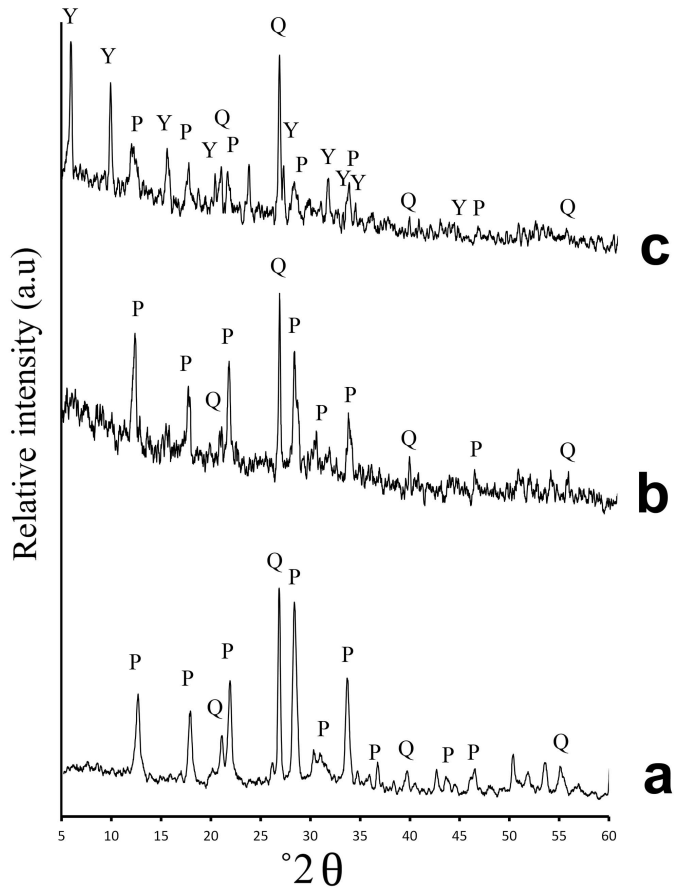

Figure 5. The effect of aging time on XRD patterns of the products, crystallized at 100ºC for 36 h: (a) aging time of the guide agent = 48 h, overall gel aging time = 96 h, $M_{4\text{-}7}$; (b) aging time of the guide agent = 96 h without overall gel aging step, $M_{4\text{-}6}$; (c) aging time of the guide agent = 48 h, without overall gel aging step, $M_{4\text{-}1}$. P: zeolite P; Y: zeolite NaY, Q: quartz.

The effect of crystallization time

Samples $M_{4\text{-}1}$, $M_{4\text{-}2}$, and $M_{4\text{-}3}$ were prepared at crystallization times of 36, 50, and 72 h, respectively, resulting in various XRD patterns (Figure 6). When the crystallization time was 36 h, zeolite P was formed as an impurity phase. Increasing crystallization time was found to favor the formation of zeolite P and pure phase P was formed after 72 h.

The effect of crystallization temperature

Attempts to prepare pure-phase zeolite NaY were continued by changing the crystallization temperature. The hydrothermal crystallization was carried out at 90 and 100ºC for 36 h. A significant increase in phase purity (Figure 7) was achieved by decreasing the crystallization temperature; consequently the zeolite NaY in pure phase was crystallized at 90ºC. As a result of these investigations, the optimum parameters used to prepare pure-phase zeolite NaY were: kaolin calcination temperature of 680ºC; aging time of the guide agent of 48 h (excluding an overall gel aging step), and crystallization at 90ºC for 36 h.

Characterization

Pure synthetic zeolite NaY was investigated here – the sample examined was obtained from method $M_{4\text{-}8}$ using a kaolin calcination temperature of 680ºC, an aging time of the guide agent = 2 days, 0 h of overall gel aging time, a crystallization time of 36 h, and crystallization temperatures of 90ºC.

The thermal degradation of the pure-phase zeolite NaY prepared was induced at a heating rate of 10ºC min^{-1} in an N_2 atmosphere (Figure 8). The DSC curve shows a ~26% weight loss between 100 and 400ºC that can be attributed to the loss of water.

The FTIR spectrum of zeolite NaY (Figure 9) shows the fundamental vibrations of the tetrahedral framework. The peak at 1009 cm^{-1} was assigned to the asymmetric stretching of the Al–O–Si chain of zeolite. The symmetric stretching and bending frequency bands of the Al–O–Si framework of zeolite appeared at 785 and 450 cm^{-1}, respectively (Zendehdel *et al*., 2010). The appearance of the peaks at 569, 1654, and 3454 cm^{-1} was attributed to the double-ring external linkage, vibration of the water molecule, and

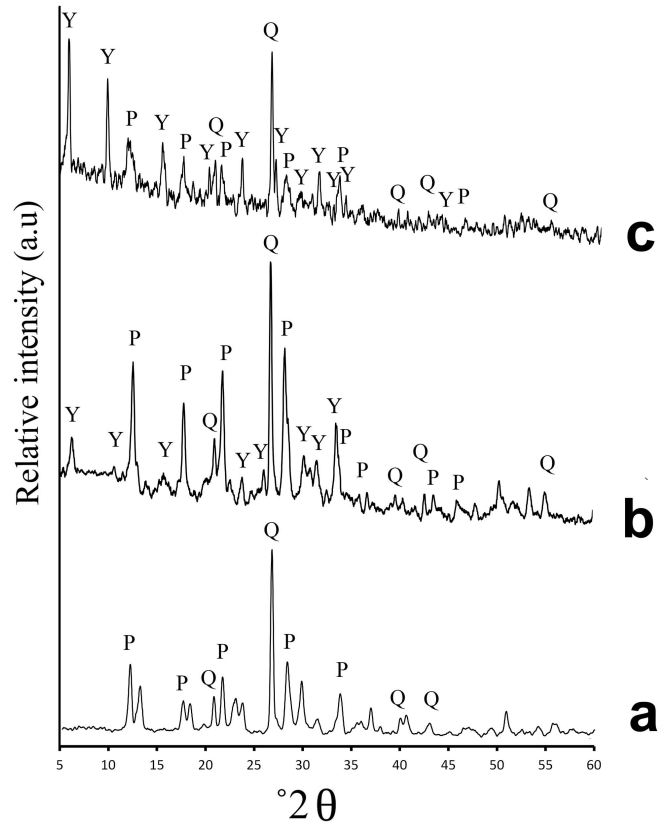

Figure 6. The effect of crystallization time on XRD patterns of the products, crystallized at 100ºC for: (a) 72 h, $M_{4\text{-}3}$; (b) 50 h, $M_{4\text{-}2}$; and (c) 36 h, $M_{4\text{-}1}$. P: zeolite P; Y: zeolite NaY, Q: quartz

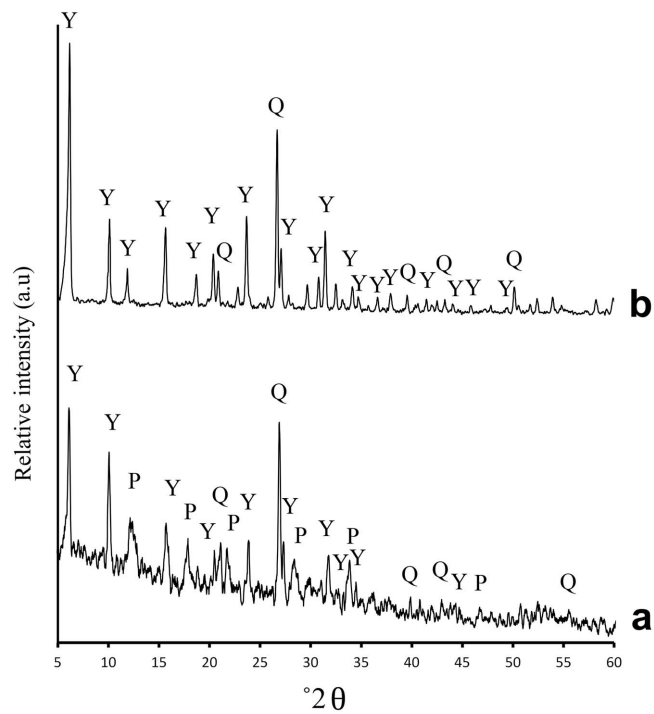

Figure 7. The effect of crystallization temperature on XRD patterns of the products, crystallized for 36 h at: (a) 100ºC, $M_{4\text{-}1}$; and (b) 90ºC, $M_{4\text{-}8}$. P: zeolite P; Y: zeolite NaY, Q: quartz.

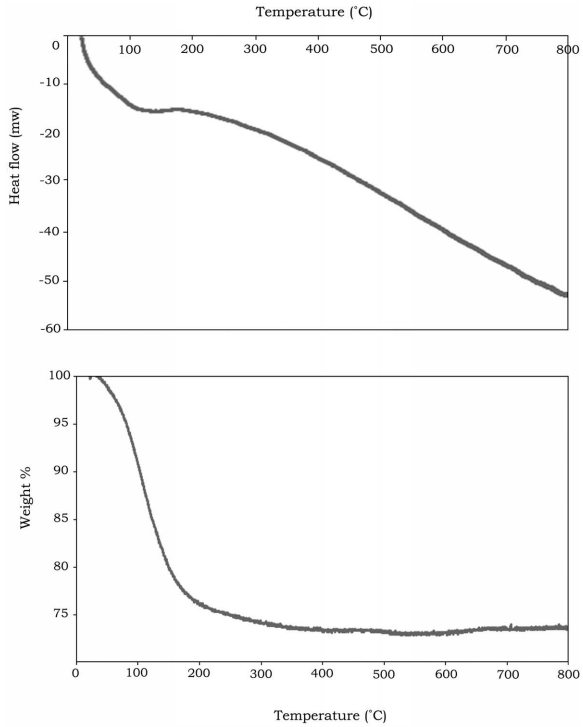

Figure 8. TGA thermogram of the zeolite NaY synthesized by the guide-agent method ($M_{4\text{-}8}$).

OH-stretching, respectively (Khabuanchalad *et al*., 2008).

The mean value of surface area of the synthetic zeolite NaY was 638 cm^2/g (from BET analysis).

Figure 10 is an image of the typical kaolin used, which has a flakey structure. Figure 11 is an image acquired from the kaolin calcined at 680ºC. Clearly, the surface of the flakey structure is partially melted and represents the transformation from kaolin to metakaolin. The microstructure of the metakaolin is amorphous and

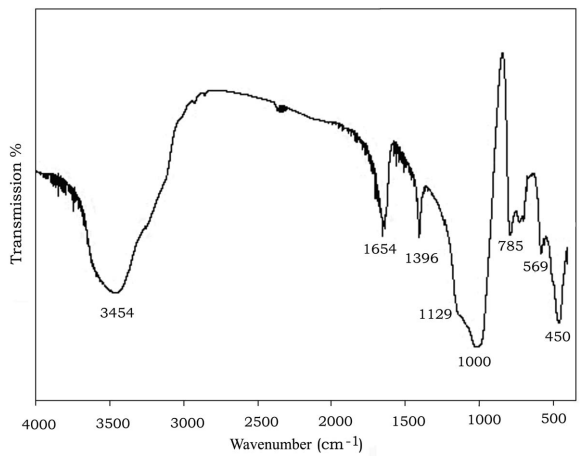

Figure 9. FTIR spectrum of the zeolite NaY synthesized by the guide-agent method ($M_{4\text{-}8}$).

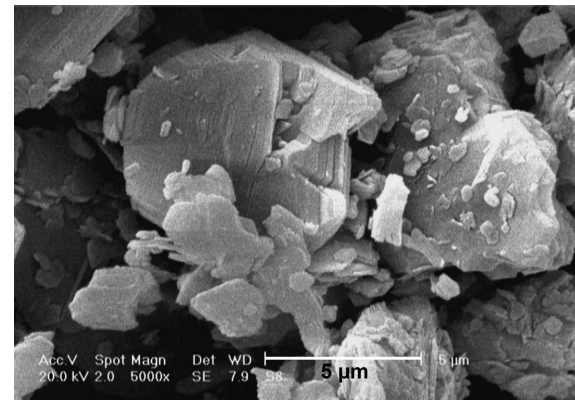

Figure 10. SEM image of kaolin.

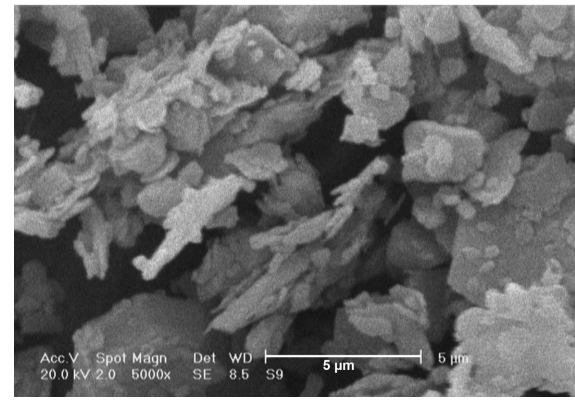

Figure 11. SEM image of calcined kaolin at 680ºC.

the XRD trace (Figure 1c) shows no peaks of any crystalline phase other than quartz (an impurity), which confirms the formation of the amorphous phase. During kaolin calcination, no other crystalline phases such as kaolinite and illite remain. Therefore, in the synthesis step, the zeolite crystals have must have been formed on

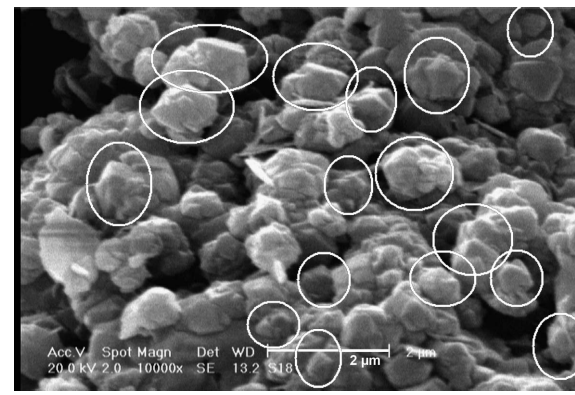

Figure 12. SEM image of the zeolite NaY synthesized by the guide-agent method ($M_{4\text{-}8}$). Circles identify subhedral grains with octahedral habit.

Table 8. EDS spectrum of the zeolite NaY synthesized by the guide-agent method ($M_{4\text{-}8}$).

Element	Weight fraction	Mole fraction
Na	0.022	2.71
Al	0.1425	14.65
Si	0.835	82.64

the amorphous background. The SEM image of the synthetic zeolite NaY (Figure 12) shows octahedral crystals of zeolite NaY (which are marked with circles) ~0.8 μm wide.

To check the composition of the zeolite NaY synthesized, analysis by EDS was undertaken (the EDS spectra were acquired from the circles indicated in Figure 12). The Si/Al ratio of 2.8 obtained is in the range for zeolite NaY (Table 8). In addition, the strong Na signal from the EDS pattern indicates the successful formation of zeolite surface NaY and the absence of other impurities.

CONCLUSION

Pure zeolite NaY, with uniform, octahedral crystals up to 0.8 μm wide, was synthesized successfully from Iranian kaolin. The method consists of three steps: firstly, the guide agent was prepared; secondly an overall gel was prepared; finally, hydrothermal crystallization. The synthesis was generally sensitive to changes in kaolin calcination temperature and hydrothermal synthesis parameters. The formation of zeolite P was competitive with zeolite NaY during preparation.

The optimum parameters to prepare pure zeolite NaY were a kaolin calcination temperature of 680ºC, an aging time of the guide agent = 48 h with no overall gel aging step, and crystallization at 90ºC for 36 h.

Three other synthesis methods were tested, including alkali fusion, synthesis with NaY seed powder, and synthesis without seed. The results revealed that the synthesis method exerts a significant influence on the structure of the zeolites prepared from metakaolin.

ACKNOWLEDGMENTS

The authors are grateful for partial financial support provided by the Nuclear Science and Technology Research Institute, Iran.

REFERENCES

Bo, W. and Hongzhu, M. (1998) Factors affecting the synthesis of microsized NaY zeolite. *Microporous and Mesoporous Materials*, **25**, 131–136.

Brindley, G. W. and Nakahira, M. (1959) The kaolinite-mullite reaction series: I. A survey of outstanding problems. *Journal of the American Ceramic Society*, **42**, 311–314.

Brunauer, S., Emmett, P.H., and Teller, E. (1938) Adsorption of gases in multimolecular layers. *Journal of the American Chemical Society*, **60**, 309–319.

Chandrasekhar, S. (1996) Influence of metakaolinization temperature on the formation of zeolite 4A from kaolin. *Clay Minerals*, **31**, 253–261.

Chandrasekhar, S. and Pramada, P.N. (2004) Kaolin-based zeolite Y, a precursor for cordierite ceramics. *Applied Clay Science*, **27**, 187–198.

Farzaneh, F., Nejad, M.M.A., and Oskooie, M.K. (1989) The synthesis of zeolites A, X and HS from natural Iranian kaolinite and the study of the transformation of zeolites X to HS and zeolites Y to P by X-ray diffraction and scanning electron microscopy. *Journal of Sciences, Islamic Republic of Iran*, **1(1)**, 23–29.

Georgiev, D., Bogdanov, B., Markovska, I., and Hristov, Y. (2013) A study on the synthesis and structure of zeolite NaX. *Journal of Chemical Technology and Metallurgy*, **48**, 168–173.

Htay, M. and Oo, M. (2008) Preparation of Zeolite Y catalyst for petroleum cracking. *World Academy of Science, Engineering and Technology*, **48**, 114–120.

Khabuanchalad, S., Khemthong, P., Prayoonpokarach, S., and Wittayakun, J. (2008) Transformation of zeolite NaY synthesized from rice husk silica to NaP during hydrothermal synthesis. *Suranaree Journal of Science and Technology*, **15**,225–231.

Liu, X., Yan, Z., Wang, H., and Luo, Y. (2003) In-situ synthesis of NaY zeolite with coal-based kaolin. *Journal of Natural Gas Chemistry*, **12**, 63–70.

Song, W., Li, G., Grassian, V.H. and Larsen, S.C. (2005) Development of improved materials for environmental applications: Nanocrystalline NaY zeolites. *Environmental Science & Technology*, **39**, 1214–1220.

Sang, S., Liu, Z., Tian, P., Liu, Z., Qu, L., and Zhang, Y. (2006) Synthesis of small crystals of zeolite NaY. *Materials Letters*, **60**, 1131–1133.

Zendehdel, M., Khanmohamadi, H., and Mokhtari, M. (2010) Host (nano cage NaY)/guest Mn(II), Co(II), Ni(II) and Cu(II) complexes of *N,N*-bis(3,5-di-tert-butylsalicyidene)-2,2-dimethyle-1,3-diaminopropane, synthesis and catalyst activity. *Journal of the Chinese Chemical Society*, **57**, 205–212.

(*Received 28 April 2014; revised 14 December 2014; Ms. 868; AE: S.M. Kuznicki*)

FORTHCOMING PAPERS

The following are some papers that have been accepted for publication in future issues of *Clays and Clay Minerals:*

Tadikonda Venkata Bharat and Asuri Sridharan. Prediction of highly plastic clay compressibility data using diffuse double layer theory

Artur Kuligiewicz, Arkadiusz Derkowski, Marek Szczerba, Vassilis Gionis and Georgios D. Chryssikos. Revisiting the infrared spectrum of the water–smectite interface

Tadikonda Venkata Bharat and Asuri Sridharan. A critical appraisal of Debye length in clay-electrolyte systems

Muazzez Çelik Karakaya, Necati Karakaya and Fuat Yavuz. Geology and formation conditions of the zeolite-bearing deposits southeast of Ankara (Central Turkey)

Paul Wersin, Andreas Jenni, and Urs K. Mäder. Interaction of corroding iron with bentonite in the ABM1 experiment at Äspö, Sweden: A microscopic approach

Javier Cuadros, Raquel Vega, and Alejandro Toscano. Mid-infrared features of kaolinite-dickite

Saadet Yapar, Günseli Özdemir, Alejandra M. Fernández Solarte, and Rosa M. Torres Sánchez. Surface and interface properties of lauroyl sarcosinate adsorbed CP^{+}-montmorillonite

Atika Chemmi, Jocelyne Brendlé, Claire Marichal and Bénédicte Lebeau. Key steps influencing the formation of aluminosilicate nanotubes by the fluoride route

Zeng-Yei Hseu, Franz Zehetner, Franz Ottner, and Yoshi Iizuka. Clay mineral transformations and heavy-metal release in paddy soils formed on serpentinites in eastern Taiwan

Clays and Clay Minerals, Vol. 62, No. 6, 520, 2014.

REFEREES VOLUME 62

The following are thanked for the time and effort they have given to providing reviews of manuscripts submitted for publication in the last 12 months:

Emel Abdioglu
Amoros Albaro
Ana C.S. Alcântara
Jacinto Alonso Azcárate
Marcelo Alves
Pilar Aranda
Ahmet Ay
Etienne Balan
Alain Baronnet
Blanca Bauluz
Christian Bender Koch
Faiza Bergaya
Ömer Bozkaya
Jocelyne Brendlé-Miehé
Florian Carstens
Walter Caseri
Muazzez Celik Karakaya
Javiera Cervini-Silva
Delphine Charpentier
Michael Cheshire
Deepankar Chouhury
George Christidis
Natalia Chubar
Javier Cuadros
Arkadiusz Derkowski
A. Umran Dogan
Stefan Dultz
Dominique Dupuis
Ömer Ece
W. Crawford Elliott
F. Elsass
Jessica Elzea Kogel
Katja Emmerich
Rasmus Eriksson
Antonin Fabbri
Wiemin Feng
Ana María Fernández
Ray Ferrell
Nicolas Finck
Najoua Frini-Srasra
Ray L. Frost
Sheila Furquim
Stéphane Gaboreau
Xiaodong Gao
Nelson Garcia
Emilia Garcia-Romero
Maria Isabel Garrido Prudêncio
Will Gates
Andreas Gehring
Jessique Ghezzi
Antonio Gil
H. Albert Gilg
Vassilis Gionis
Christopher Gorski
Georg Grathoff
Régis Guégan
Necip Guven
Hong Hanlie
Hongping He
Adriane Horbe
Kieren Howard
Laiming Huang
Warren Huff
Miroslav Huskic
Marian Janek
William Jaynes
Andrey G. Kalinichev
Shizhao Kang
Birgul Karan
Abhijeet Karkamkar
Stephan Kaufhold
Reinhard Kleeberg
Tomasz Kozlowski
Alena Kremleva
Thomas Kuehn
Steven Kuznicki
Bruno Lanson
Olivier Leupin
Yaping Li
Xiandong Liu
Xiancai Lu
Johannes Luetzenkirchen
Andrew Luhmann
Jana Madejová
Eva Mako
Prakash K. Malla
Mario Manassero
Jakub Matusik
Richard William McCabe
Dougal McCarty
Lorenz Meier
Lionel Mercury
Ahmet Mermut
Nicolas Michau
Marc Michel
Jean-Carlos Montero-Serrano
Lucas Moore
Enver Murad
Wagner Mussel
Sankar Nair
Pablo Naranjo
Phil Neuhoff
Makoto Ogawa
Markus Olin
Oladipo Omotoso
Muserref Onal
Marek Osacky
Helena Palkova
Dimitrios Papoulis
Pooria Pasbakhsh
Esperanza Pavon
F.J. Pearson
Pierre Pellard
Manuel Pelletier
Martin Pentrák
Sabine Petit
Manuel Pozo Rodriguez
Dimitri Prêt
Jason Price
Petr Ptacek
P.K. Pujari
Roland Pusch
Stuart Raeburn
Benaissa Rhouta
Franz Rinderknecht
Vicente Rives
Peter Ryan
James Sawada
Birgit Schampera
Paul Schroeder
Cristian Schulthess
Helge Stanjek
Zhong-Xi Sun
K. Suresh
Qi Tao
Fabio Tateo
Antoine Thill
Ali Tlili
Jonas Tokarsky
Snehasis Tripathy
Asuman Turkmenoglu
Kristian Ufer
Marta Valaskova
Jeroen van Duijneveldt
Eric van Oort
Miguel Vicente
Philippe Vieillard
Cesar Viseras
J. Marion Wampler
Laurence Warr
Peter G. Weidler
Charles Weiss
Martin Wells
Paul Wersin
Lynda Williams
Pingxiao Wu
Yunfei Xi
Yingqian Xiong
Chuanliang Yan
Shijian Yang
Li Yimin
Hua Yu
Peng Yuan
Runliang Zhu